SCALE CONTINUUM OF VERTICAL EXCHANGES BETWEEN LOWER STRATOSPHERE AND SURFACE LAYERS

A Dissertation

Submitted to the Graduate School

of the University of Notre Dame

in Partial Fulfillment of the Requirements

for the Degree of

Doctor of Philosophy

by

Patrick T. Conry

Harindra Joseph S. Fernando, Director

Graduate Program in Civil and Environmental Engineering and Earth Sciences

Notre Dame, Indiana

November 2017

SCALE CONTINUUM OF VERTICAL EXCHANGES BETWEEN LOWER STRATOSPHERE AND SURFACE LAYERS

Abstract

by

Patrick T. Conry

Exchanges of momentum, heat, and moisture between layers of atmosphere and upper ocean govern the variability of global climate down to local environments. Vertical exchange mechanisms include the largescale mean flow, planetary to small-scale waves, and ubiquitous turbulent eddies, the latter being particularly prominent in the atmospheric boundary layer (ABL). In this thesis, observational datasets covering a wide range of spatiotemporal scales are analyzed and interpreted to unravel multi-scale vertical exchange processes underpinning the atmospheric variability.

The major component of this work was a study of intraseasonal disturbances in the Indian Ocean (IO) during late boreal winter of 2015, dubbed ASIRI-RAWI. These disturbances drive tropical weather and travel as (theoretically predictable) planetary waves. Upper-air soundings from multiple IO sites as well as model reanalysis were utilized to educe wave activity. Equatorial baroclinic Kelvin waves (KWs) within the

stratified lower stratosphere and upper troposphere were identified as dominant patterns repeating biweekly. The eastward- and downward-propagating KWs initiated shear instabilities in the tropical tropopause layer (~17 km). Later when phase propagation brought westerly winds and high barometric pressure to ~12-14 km altitude, KWs coupled with lower-tropospheric disturbances and initiated strong vertical motions within 'chimney'-like columns of 'convection' ~300-500 km wide. High-resolution measurements from remote-sensing instruments and a flux tower at the Seychelles site captured the impacts of these events on the surface layer of ABL as westerly wind bursts (WWBs). The quasi-periodic WWBs were also studied using one-dimensional ocean mixed layer model to estimate response of upper ocean. These finding suggest new mechanisms for upper troposphere interacting with surface layers and should have implications in equatorial air-sea exchange parameterizations of coupled atmosphere-ocean global circulation models.

A case study on turbulence mixing parameters is also conducted based on fine-scale measurements from a specialized hot-film probe deployed in stably stratified shear flow of ABL. Direct measurements of mixing coefficient Γ – used widely in modeling atmospheric and oceanic flows – demonstrated its dependence on multiple parameters, thus underscoring the challenge of parameterizing turbulent mixing in environmental flows. However, during certain intervals the measurements behaved consistently with past laboratory/numerical experiments, which could be explained using physical arguments.

This thesis is dedicated to Mom and Dad, who have provided loving support during this work and throughout my lifetime, as well as to Noni, Grandma, and Grandpa, my wonderfully caring grandparents.

CONTENTS

FIGURES

TABLES

ACKNOWLEDGMENTS

First, I would like to acknowledge the funding sources for my graduate studies and the projects that made this work possible. I was supported for three years by the Department of Defense (DoD) through the National Defense Science & Engineering Graduate Fellowship (NDSEG) Program. I was also supported throughout my five years as a graduate student by an Arthur J. Schmitt Presidential Fellowship through the Arthur J. Schmitt Foundation. ASIRI-RAWI was funded through the Office of Naval Research (ONR) grants N00014-14-1-0279 and N00014-13-1-0199. MATERHORN was funded by an ONR Multidisciplinary University Research Initiative (N00014-11-1-0709).

I cannot express enough gratitude to the many individuals and groups who have made this work possible. I will name some here who have most directly contributed to my thesis and growth as a graduate student.

I would like to give foremost thanks to my advisor Joseph Fernando for his support, guidance, and teaching. He consistently and graciously has made himself available in his office or across-the-oceans via email to discuss problems and offer feedback on my work. In regard to this thesis, he provided helpful input on all chapters, and his energy and enthusiasm have been inspiring.

I express thanks to Eliezer Kit who has taught me a great deal about turbulence and hot-film measurements. Over detailed discussions and written correspondence he provided me with much of the knowledge and insights necessary to complete the work of Chapter 5. Also in regard to the 'combo' probe deployment during MATERHORN, Scott Coppersmith, Chris Hocut, and Dan Liberzon provided crucial support.

I am grateful to my committee members – Diogo Bolster, David Richter, and Joannes Westerink – not only for their consideration of my thesis but also for shaping the Environmental Fluid Dynamics (EFD) Group at Notre Dame along with other faculty members. It has been an amazing environment in which to research, and additional thanks go out to every student and researcher who has been a part of building the positive community.

While not contained in this thesis, an important part of my graduate studies was as a visiting scholar at the University of Salento (Italy). I thank Silvana Di Sabatino and my other collaborators there for hosting me during this meaningful experience.

I am also thankful to all the members of the Fernando Group as well as our many visitors; it has been a pleasure to work alongside them and take the occasional break together. In regard to ASIRI-RAWI, Lik-Khian Yeo and Hyejin Ok worked with me on this project during their visits. To Hyejin and her advisor Yign Noh I am indebted for teaching me much about ocean mixed layer modeling and conducting numerical studies under my direction. Figures 4.9 and 4.10 were produced by Hyejin during our collaboration.

The experimental phase of ASIRI-RAWI was a massive undertaking and many thanks are due to all the participating individuals for its success. I list here those who contributed most directly to the gathering and processing of the data: Upul Adhikari, Vincent Amelie, Byron Blomquist, Ed Creegan, Jean-Paul Dodin, Chris Hocut, Hencel Hollanda, Priyantha Jinadasa, Nelson Lalande, Laura Leo, Ben MacCall, Theron Moncherry, Selvan Pillay, Chien Wang, and Yansen Wang. I give a special thanks to Laura Leo, who led the experiments at Singapore and Sri Lanka while I led at Seychelles. I have enjoyed working with her on multiple projects during my graduate (and undergraduate) research. As a co-author on a manuscript, Laura also prepared the final versions of several figures in Chapters 3 and 4.

I thank one final, important group – my many teachers, coaches, and adult relatives who have taught me over the years. They have imparted much knowledge and many life lessons, without which I could not have completed (or even begun) my graduate studies. Thank you all.

ABBREVIATIONS

1D	One-dimensional
3D	Three-dimensional
ABL	Atmospheric boundary layer
AOGCM	Atmosphere-ocean global circulation model
ARL	Army Research Laboratory
ASIRI	Air-Sea Interaction in Northern Indian Ocean
ASIRI-RAWI	ASIRI-Remote Sensing of Atmospheric Waves and Instabilities
BoB	Bay of Bengal
CBL	Convective boundary layer
CINDY2011	Cooperative Indian Ocean Experiment on Intraseasonal Variability in the Year 2011
CPT	Cold-point tropopause temperature
DYNAMO	Dynamics of the Madden-Julian Oscillation
ECMWF	European Centre for Medium-Range Weather Forecasts
ENSO	El Niño-Southern Oscillation
ERA-I	ECMWF Interim
EUMETSAT	European Organisation for the Exploitation of Meteorological Satellites
GCM	Global circulation model

IO	Indian Ocean
ITCZ	Intertropical Convergence Zone
K-H	Kelvin-Helmholtz
LT	Local time
MJO	Madden-Julian Oscillation
MW	Microwave
NARA	National Aquatic Resources Research Agency (Sri Lanka)
NASA	National Aeronautics and Space Administration (USA)
NASCar	Northern Arabian Sea Circulation-Autonomous Research
NCAR	National Center for Atmospheric Research (USA)
NCEP	National Centers for Environmental Protection (USA)
ND	University of Notre Dame
NOAA	National Oceanic and Atmospheric Administration (USA)
OLR	Outgoing longwave radiation
QBO	Quasi-biennial oscillation
QBWO	Quasi-biweekly oscillation
RMM	Real-time Multivariate Madden-Julian Oscillation Index
rms	Root mean square
SBL	Stable boundary layer
SST	Sea surface temperature
TKE	Turbulent kinetic energy

TOGA COARE	Tropical Ocean-Global Atmosphere Coupled Ocean-Atmosphere Response Experiment
TTL	Tropical tropopause layer
UTC	Universal Time Coordinated
WMO	World Meteorological Organization
WWB	Westerly wind burst
XMET	Expeditionary Meteorological (sensor)

CHAPTER 1:

INTRODUCTION

Vertical exchanges (fluxes) of heat, momentum, and moisture through the various layers of the atmosphere profoundly affect the changing environmental conditions near the Earth's surface, more specifically the dynamics of the atmospheric boundary layer (ABL). Fluid motions underlying these exchanges are governed by a combination of radiative, tidal, and a host of internal Earth-system processes occurring across range of space-time scales. These processes are spanning physical space from atmospheric general circulations (~10^4 km) down to turbulent eddies (~1 m) in the ABL. Understanding and modeling the dynamics of this scale continuum remains a grand challenge in environmental (weather and climate) prediction.

The dynamical processes associated with a particular phenomenon depend on its space-time scales. In modeling applications, the grid cell size is a "representative volume" determining which processes are sufficiently large to be resolved by the computations and which are smaller, i.e., sub-grid scale. In either case, observations across the scale continuum are imperative for improving prediction of various phenomena because of dynamic coupling between scales which occurs in real atmosphere. Therefore models' predictions of resolved scales are dependent on unresolved (i.e., sub-grid) scales, the effects of the latter being parameterized in the models.

Observations across the scales have become particularly important with the recent advent of “seamless” modeling platforms. These platforms are capable of conducting simulations across a wide swath of scales using the same family of models but with different configurations. For example, the United Kingdom Met Office’s Unified Model is of this ilk, in which a global configuration (~17 km resolution) is used for medium-range weather forecasts (48 hours to 10-14 days) whereas regional configuration allows nesting down to ~1.5 km grid resolution within a particular area (domain) of interest to predict smaller-scale variability. Interestingly, the U.S. Weather Research and Forecasting Innovation Act of 2017 (H.R. 353) signed into law on 18 April, 2017 seeks major advancement of short- to long-range forecasting capabilities of U.S. agencies through better forecasting tools. In seamless modeling, the same parameterization schemes are used across the scales on a traceable framework, and the development of these parameterizations requires ambitious observations across the scales. These needs have been the impetus for the work presented in this thesis, a synthesis of multi-scale observations based primarily on a field campaign conducted by a collaborative group from U.S.A., Sri Lanka, Singapore, and Seychelles, for which I was a participant. I was stationed in Seychelles for a two-month period and oversaw the instrument deployment, data collection, and data processing. This dissertation makes use of the collected datasets to undertake focused, yet integrative across-the-scale, studies of exchange processes between atmospheric layers and the ocean mixed layer.

The various spatiotemporal scales and phenomena pertinent to the region-of-interest — equatorial Indian Ocean (IO) — are described in Section 1.1 with pictorial accompaniment (Figure 1.1). In Section 1.2, a short review of tools used to analyze the scale continuum of atmospheric exchange processes is given. The tools and general approach employed here are then introduced in Section 1.3, followed by the main hypotheses used for research in Section 1.4. Finally Section 1.5 outlines the subsequent chapters.

1.1 Overview of Equatorial Phenomena Spanning the Scales

Since a range of physical scales are covered within this thesis it is useful to demarcate them quantitatively and provide concrete examples. Therefore in the following descriptive paragraphs the physical scales of atmospheric motions are divided into four main categories (respective space and time scales given in parentheses): the largest scales are the *climate scales* (~10,000 km and months to centuries); the large scales include *intraseasonal to synoptic scales* (~100-1000 km and days to months); the transition scales are the *mesoscales* (~1-100 km and hours to days); the small scales include the *microscales to fine scales* (<1 km down to 1 mm and seconds to hours). Some examples of actual physical processes occurring within each range of scales are provided in the following paragraphs; certain examples important in the region-of-interest for this work are also shown schematically in Figure 1.1. The categories used here are in no way universal; there are many different classifications that exist, e.g., Oke (1978). It should be stressed that there is a continuum of scales, and these divisions between scales are not meant as inflexible barriers but as regions of overlap where numerous two-way interactions between scales are occurring. Through continuing investigations on delineation of phenomena at various scales, the creation of new knowledge will allow the scientific community to unravel mechanisms undergirding scale interactions like those that will be identified in subsequent chapters.

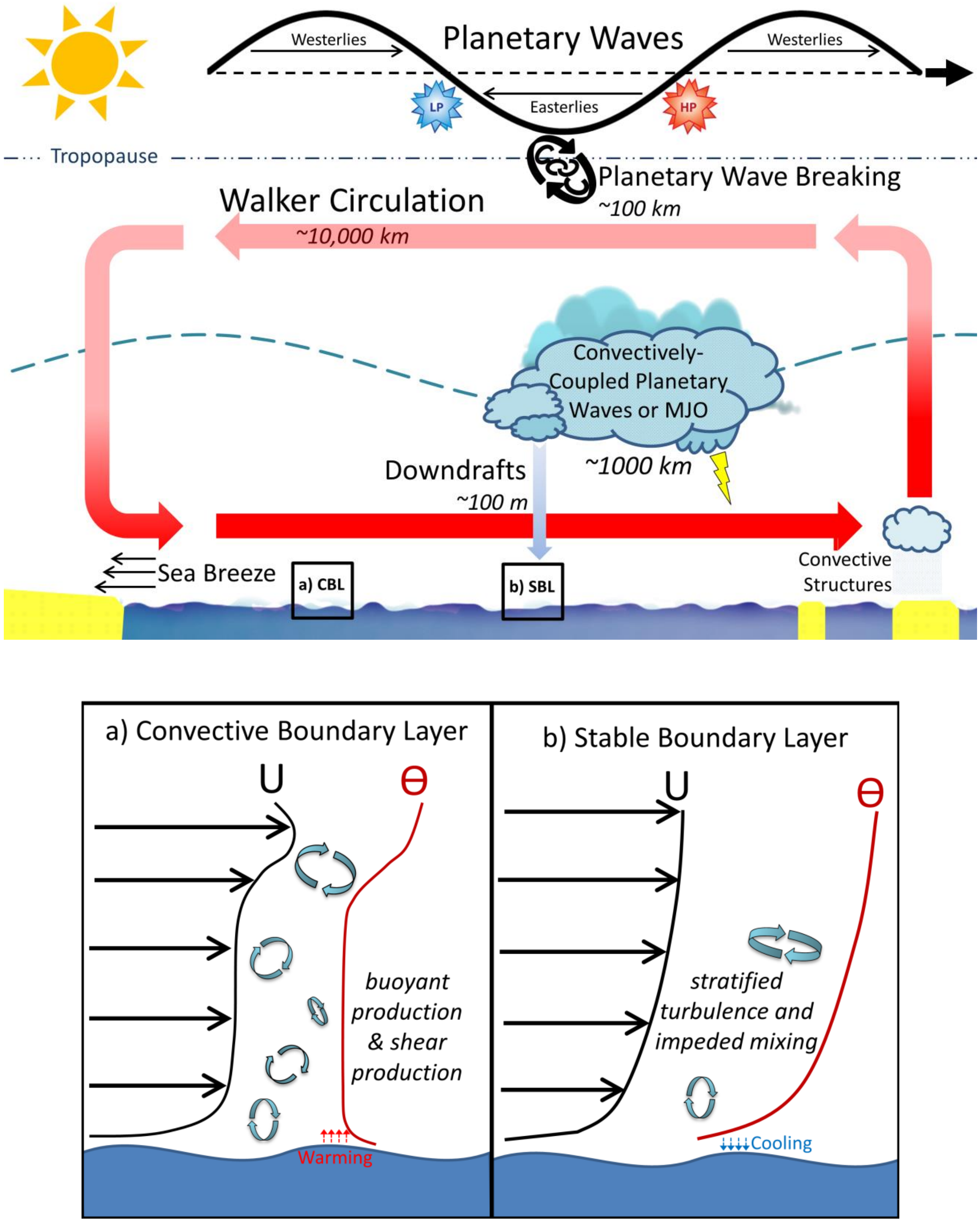

Figure 1.1: Schematic of atmospheric phenomena occurring in equatorial warm oceans (e.g. Indian Ocean) across multiple spatial scales. Lower panels show common atmospheric boundary layer conditions encountered: (a) convective boundary layer and (b) stable boundary layer.

1.1.1 Global circulations – Climate scales

Motions that circumnavigate the Earth's atmosphere on scales of the order of 10,000 kilometers (Earth's circumference: ~40,000 km) are the global circulations. These motions are typically driven by transoceanic/continental meridional (north-south) and zonal (east-west) temperature gradients, for example, the Hadley and Walker circulations, respectively. For modeling applications, atmospheric or oceanic global circulation models (GCMs) can predict seasonal variability over several months within their respective domains. More sophisticated coupled atmosphere-ocean GCMs (AOGCMs) are required for longer term predictions and are limited to coarser domains. AOGCMs are further coupled with biogeochemical models to construct climate models, which predict interannual variability spanning years to centuries. The climatic conditions that persist at a given location and their interannual variability are investigated with these climate models. For instance, the Pacific Walker circulation is associated with the global-maximum warm pool and rain pool that exist in the western Pacific and Maritime Continent. It is sometimes related with (east-west) Walker circulation in IO with its strength classification referred to as dipole. The negative IO Dipole is characterized by sea surface temperature (SST) warmer than normal in the eastern IO but cooler in the west. The reverse typifies the positive IO dipole. All these circulations and their reversals are linked to the El Niño-Southern Oscillation (ENSO) and its important role in interannual, global-scale weather-climate variability.

1.1.2 Planetary waves – Intraseasonal to synoptic scales

Zooming in below 10,000 kilometers, many important phenomena that dictate atmospheric variability exist on spatial scales on the order of 1000 to 100 kilometers and timescales on the order of days to weeks and up to 2-3 months. At the larger end of this range are the intraseasonal (also known as subseasonal) oscillations while the smaller disturbances are commonly classified under the umbrella of synoptic variability. In the tropical atmosphere, equatorial planetary waves play a dominant role in intraseasonal-to-synoptic variability in the (dry) middle atmosphere (Andrews et al. 1987) as well as in the lower atmosphere (Kiladis et al. 2009), where they are often moist waves coupled with convection, i.e., convectively coupled.

Equatorial waves were first theorized one half-century ago by T. Matsuno (1966) as a solution to the shallow water equations on an equatorial beta plane. In the tropical atmosphere, rising air masses caused by intermittent heating at the lower boundary (i.e. atmospheric convection) result in frequent perturbations to hydrostatically-balanced layers of air, exciting various wave modes in the lower and middle atmosphere. Some of these wave modes were identified mathematically by starting from the equations of motion in the zonal and meridional directions on a beta plane along with shallow water continuity equation. These equations are

$$\frac{\partial u}{\partial t} - (\beta y)v = -g\frac{\partial \eta}{\partial x} = -\frac{\partial \phi}{\partial x} \tag{1.1}$$

$$\frac{\partial v}{\partial t} + (\beta y)u = -g\frac{\partial \eta}{\partial y} = -\frac{\partial \phi}{\partial y} \tag{1.2}$$

$$\frac{\partial \phi}{\partial t} + gH_{\mathrm{o}}\left(\frac{\partial u}{\partial x} + \frac{\partial v}{\partial y}\right) = 0, \tag{1.3}$$

where ϕ is the geopotential height, β the coefficient from beta-plane approximation (or Rossby parameter), and H_o the height of the undisturbed fluid layer. Meridionally decaying wave solutions are assumed to be of the form

$$\begin{pmatrix} u \\ v \\ \phi \end{pmatrix} = \begin{pmatrix} \tilde{u}(y) \\ \tilde{v}(y) \\ \tilde{\phi}(y) \end{pmatrix} e^{i(kx-nt)}, \tag{1.4}$$

where k is the wave number and n is the wave frequency. Substituting Eq. 1.4 into Eqs. 1.1-1.3 and eliminating u and ϕ through a series of algebraic manipulations, one can write the following second-order differential equation with v as the only unknown:

$$\frac{d^2\tilde{v}}{dy^2} + \left[\frac{n^2}{gH_{\mathrm{o}}} - k^2 - \frac{k\beta}{n} - \frac{\beta^2 y^2}{gH_{\mathrm{o}}}\right]\tilde{v} = 0 \ . \tag{1.5}$$

If $\tilde{v} \to 0$ as $y \to \infty$ is imposed as boundary condition, the constant part inside brackets of Eq. 1.5 must satisfy the relationship

$$\frac{\sqrt{gH_{\mathrm{o}}}}{\beta}\left(\frac{-k}{n}\beta - k^2 + \frac{n^2}{gH_{\mathrm{o}}}\right) = 2m+1, m = 0,1,2,\dots , \tag{1.6}$$

where m is the meridional mode number. In order to have wavelike solutions, the part of Eq. 1.5 inside the brackets must be positive and therefore

$$\xi = \frac{y}{\sqrt{\frac{\sqrt{gH_o}}{\beta}}} < \sqrt{2m+1}, \tag{1.7}$$

so that all wave solutions are equatorially trapped. The solutions to Eq. 1.1 are of the form

$$\tilde{v}(\xi) = v_o H_m(\xi) e^{-\left(\xi^2/2\right)}, \tag{1.8}$$

where v_o is a constant from the initial conditions and H_m (m = 0,1,2,…) are m^{th} order Hermite polynomials. In general three roots in n exist for Eq. 1.6, representing eastward and westward inertio-gravity waves and (westward) planetary Rossby gravity waves. A final major class of linear equatorial waves is found by setting meridional component v equal to zero in Eqs. 1.1-1.3 and solving. This resulting special-case solution is the eastward Kelvin wave (see Chapter 3 for a more detailed treatment of equatorial Kelvin wave dynamics).

The wave modes of Matsuno's theory have subsequently been found to account for a significant portion of equatorial variability (Grise and Thompson 2012). The lower modes of Kelvin and Rossby waves generally have wave periods on the intraseasonal time scales (~10-80 days) whereas their higher modes and inertio-gravity waves tend to fall within the scope of synoptic variability (3-10 days). The larger-scale (intraseasonal) equatorial wave modes are thus outside the bounds of traditional medium-range weather forecasts even though they contain the greater portion of the energy content of equatorial wave activity (Žagar et al. 2009). A major driver of the tropical variability on the intraseasonal scales is the Madden-Julian Oscillation (MJO; Madden & Julian, 1972). Purely neither a Kelvin or Rossby wave, MJO contains signatures of both and is likely a non-linear combination of various equatorial wave modes. The MJO envelope encompasses smaller scale disturbances such as embedded convectively-coupled Kelvin waves causing localized one-day wind bursts (Moum et al. 2014), and both MJO and Kelvin waves can play a major role in changing conditions at larger scales, for instance, ENSO phase (Straub et al. 2006). Owing to similar scale interactions for other equatorial waves, the intraseasonal scales are readily detected in observational datasets from tropics just as the synoptic scales are prominent in extratropical datasets due to the baroclinic instability (Smagorinksky 1982).

1.1.3 Local circulations and instabilities – Mesoscales

At sub-synoptic scales (~ 1 to 100 km) are a host of phenomena that give rise to higher frequency atmospheric variability. These are the mesoscales that can be associated with the above planetary wave oscillations, for instance, through localized wave breaking due to instability (Fujiwara et al. 2003). Appropriate temporal scales are hours to days, and therefore may include effects of diurnal cycle of surface heating, such as sea and land breezes in coastal areas of IO (see Figure 1.1). The preceding example demonstrates that surface heterogeneities play an important role in mesoscale variability. Likewise surface heterogeneities of similar spatial scales (~5-100 km), such as urbanization, complex terrain, or agricultural land cover, can trigger mesoscale variability. Islands, for instance, have an impact on the frequency and distribution of precipitation in their immediate vicinity (Cronin et al. 2015). On the eastern boundary of IO, thousands of variously-sized islands of the Maritime Continent alter rainfall patterns of passing MJO events such that the MJOs' propagation around the globe can be affected

(Peatman et al. 2014), an example of mesoscale-global scale interactions. At times, new phenomena such a rectified flows or convective envelopes can arise due to these scale interactions.

1.1.4 Atmospheric boundary layer turbulence – Microscales and below

The microscales of fluid motions span from ~500 m down to 1 m and vary over hours to minutes. Convection is a microscale process for tropical atmosphere, which contributes to many of the larger-scale disturbances discussed above. Given its smaller scale, however, in global and regional modeling convection is a sub-grid process that must be parameterized. Therefore process studies at the microscales, e.g., large eddy simulations (Skyllingstad and de Szoeke 2015), have been used for better understanding of the convective motions (updrafts and downdrafts) as well as turbulent eddies that are the building blocks of convection and cloud formations.

Combined upward and downward turbulent motions, such as those in convection, cause a mean vertical exchange (flux) of moisture, momentum, heat, etc. G. I. Taylor introduced the notion of eddy fluxes of momentum and heat based on measurements over the marine boundary layer taken just over one century ago (Taylor 1915, 1970). While turbulent eddy motions are ubiquitous throughout atmosphere, they are most impactful in the ABL, where gradients of properties are prevalent so are the exchange processes. In the case of marine boundary layer, turbulence processes are of prime importance to air-sea fluxes. It has been well demonstrated that without proper atmosphere-ocean coupling, much of the travelling weather systems such as intraseasonal oscillations would remain stationary, causing severe errors in medium- to long-range forecasts (Ham et al. 2014).

Exchange processes in ABL depend largely on its state, whether the boundary layer is under convective, neutral, or stable conditions. For the convective boundary layer (CBL) turbulence, the vertical length scales can be large, and CBL can even reach several kilometers in height (known as deep convection). Deep convection prevails over equatorial oceans, particularly within the seasonally-varying intertropical convergence zone (ITCZ), with a mixed layer close to the ground where particularly strong turbulent motions sustain the moist sublayer with nearly constant temperature and wind speed (Fig. 1.1a). Exchange processes in ABL are much different under stable stratification (Fig. 1.1b), given inhibition of turbulence by buoyancy. The stable boundary layer (SBL) in equatorial oceans mostly forms not by surface cooling as in terrestrial nocturnal boundary layer but by convective downdrafts that cool due to evaporation during descent and can conglomerate to form larger-scale cold pools (Skyllingstad and de Szoeke 2015). In either case, the SBL is ~10-100 meters in height and lasts for hours to days (except in polar regions where it can last weeks to months) before giving way to neutral and then convective conditions due to heat fluxes at lower boundary from warmer ocean or morning onset of solar irradiation. In SBL, vertical turbulent transport is suppressed by buoyancy forces, but shear can produce turbulence and thus maintain some turbulent mixing, which must be appropriately parameterized.

1.2 Tools for Understanding Atmospheric Exchanges across the Scales

1.2.1 Seamless modeling

Traditionally, the weather and climate modeling communities have separately developed numerical models to address a select niche of spatiotemporal scales. For instance, medium-range weather forecasts are a product of gridded synoptic scale models with reasonable confidence in accuracy not exceeding one week or so. Often when there is a need to assess environmental impacts of atmospheric variability across a range of scales, output from models operating at separate scales is parsed together (nested modeling), which can be a cumbersome and computationally expensive process (e.g., Conry et al. 2015). In the past few decades there has been a purposeful convergence of weather and climate models to create unified modeling frameworks (Brown et al. 2012). These efforts towards "seamless prediction" incorporate atmospheric interactions with slowly-evolving components of the Earth system (oceans, glaciers, and land) which before were prioritized in just climate modeling (Hurrell et al. 2009). The seamless approach is skillful for capturing variability at the intraseasonal scales, which were previously outside the prioritized bounds of either weather or climate forecasting communities (Zhang 2013). While computational feasibility currently limits unified models to spanning only the climate to synoptic scales (mesoscales may also be covered in limited cases, and recently has been downscaled even to microscales for research purposes), these modeling frameworks are becoming important tools for understanding the interconnectedness of variability across space and time scales. A major source of model error is the mismatch of the grids at the boundaries between the fine resolution model and the global model as well as changing model physics therein, and, to address the latter, parameterizations valid across the scales are needed (Tang et al. 2013).

1.2.2 Observational platforms and campaigns

The real atmosphere offers a chance to observe scale interactions, but the efficacy of observations depends on meteorological instrumentation being available to deploy in targeted locations. The multitude of data available for researchers of atmospheric variability may be divided into two primary categories. First, are those collected with long-term multi-year or permanent observational platforms operated by forecasting agencies and research institutions; these often cover large space and long time scales. Second, are data collected during shorter term (on the order of months to days) field campaigns featuring dense arrays of instruments to study focused atmospheric processes. Like in modeling, different research communities make and use the largescale and small-scale observations so synthesis between them has been rare. Both are utilized in the current work and will be introduced below with more details following in Chapter 2.

Since the advent of meteorological satellites a half-century ago, remotely-sensed data now covers Earth's entire surface and supplies information needed to estimate various atmospheric (and oceanic) variables. The resolution of satellite measurements is limited to the larger spatial scales, but their coverage of Earth's entire surface is a major advantage. On the other hand, meteorological organizations operate an infrastructure of thousands of site-specific stations taking basic surface measurements (e.g., temperature, wind speed and direction, humidity, pressure), with several hundred also providing flux measurements and more conducting daily radiosonde measurements. These station observations are concentrated near populated areas, and there is an acute scarcity of data over oceans. However, limited and dispersed buoys and moorings provide coverage for meteorological variables. All these long-term observational platforms are maintained regularly and usually accessible to public for research purposes. Some of these observational datasets are important tools for developing model reanalysis as well. While reanalysis data are not truly observations, they bear striking similarities and are often utilized as such (Parker 2016). Like with satellite measurements, reanalysis data capture only the variability at larger scales (~100 km or above).

It addition to extant global measurement platforms, which are limited in spatial resolution or geographical distribution as mentioned, research groups occasionally conduct short-term, directed field campaigns, particularly those occurring at mesoscales and microscales not well-covered in the available databases, including over oceans. A foundational experiment on air-sea interactions was undertaken in the early 1990s to study the western Pacific warm pool and its role in ENSO. Called the Tropical Ocean-Global Atmosphere Coupled Ocean-Atmosphere Response Experiment (TOGA COARE), this international experiment included several months of intensive atmospheric and oceanographic observations from a dense array of ocean moorings, ship cruises, and aircraft flights (Webster and Lukas 1992). Detailed measurements down to fine-scale turbulence in the focus area were incorporated with a larger-scale dataset covering more than a decade, and this synthesis helped to understand how processes in warm pool influenced the intraseasonal and climate scales. Almost two decades later a major experiment comparable in spatial scale to TOGA COARE was carried out in Indian Ocean with several complementary research projects under the international umbrella CINDY2011 (Cooperative Indian Ocean Experiment on Intraseasonal Variability in the Year 2011), with the U.S. component dubbed DYNAMO (Dynamics of the MJO). The field campaign covered central equatorial IO and surrounding area for several months in the boreal fall and winter of 2011-12, and captured multiple full cycles of intraseasonal MJO (Yoneyama et al. 2013). The two projects (TOGA COARE and CINDY2011) were certainly among the most comprehensive across multiple scales conducted around the IO region. Major upcoming field experiments planned for the region in 2018 include Year of Maritime Continent (YMC) and Monsoon Intraseasonal Oscillations in Bay of Bengal (MISO BoB) are attempting to add to our understanding of regionally-important scale interactions.

1.3 Experimental Approach

This thesis aims to contribute to the understanding of multi-scale processes of vertical exchange through the atmosphere and at air-sea interface by making use of available datasets. The main project described in this dissertation was at the interface between the ASIRI (**A**ir-**S**ea **I**nteractions in the Northe**r**n **I**ndian Ocean) and NASCar (**N**orth **A**rabian **S**ea **C**irculation-**a**utonomous **r**esearch) initiatives of the Office of Naval Research (ONR), and it was dubbed ASIRI-RAWI (**R**emote Sensing of **A**tmospheric

Waves and **I**nstabilities). It dealt with detailed local observations of ABL through middle atmosphere up to ~20-30 km using an array of instruments. The instrument array and its relations to ASIRI and NASCar are described in Wijesekera et al. (2016) and Centurioni et al. (2017), respectively. In addition, closely related modeling studies (i.e., reanalysis) and satellite products were used to fill in gaps in the experimental dataset, particularly at the large scales. Together, these datasets cover from global to boundary layer turbulence scales in the IO atmosphere and are useful for detecting important phenomena and their interactions at different scales. The measurements from ASIRI-RAWI, however, could not resolve the finest (Kolmogorov) scales of turbulence due to instrumental constraints; these fine scales are important nonetheless for quantifying mixing in turbulent flows. For fine scales, I have used valuable measurements taken by a specialized sonic-hot-film anemometer system as a part of MATERHORN experiment on terrestrial atmosphere in complex terrain. The collected turbulence data reached down to the smallest spatiotemporal scales measurable in real atmosphere and provided information on the mixing in stably stratified shear flows, which exist in many environmental conditions such as convective cold pools (in surface layer of IO ABL), nocturnal boundary layer (terrestrial), and sheared equatorial thermocline (oceanic).

1.4 Research Hypotheses

The following are the hypotheses that guided the research described in the dissertation.

1. *The intraseasonal scales of variability are evident/dominant in equatorial Indian Ocean atmosphere and impact smaller-scale exchange processes in atmospheric boundary layer and the ocean beneath via air-sea interactions. (Addressed in Chapters 3, 4, & 5)*

The equatorial Indian Ocean atmosphere is replete with quasi-periodic, large-scale disturbances (i.e. planetary waves). The energy source for these equatorially-trapped waves is often convection, so their amplitudes may be more notable south of the equator, where the ITCZ is usually found in IO. Since these waves' motions help determine variables such as velocity, temperature, pressure, and their gradients at a given height, they can contribute to the vertical exchange mechanisms outlined in the following two hypotheses. Signatures of intraseasonal oscillations are prominent in the vertical structure of atmosphere during certain key phases of equatorial waves aloft, and they may even take precedence over variability on diurnal timescales near the surface (e.g., sea and land breeze). The resultant modifications to surface fluxes will impact the ocean via interfacial exchanges of heat and momentum. Major impacts of MJO on mixed layers of ABL and ocean have been demonstrated previously (e.g., Moum et al. 2014) so the present work intends to demonstrate impacts for other varieties of intraseasonal oscillations. While simultaneous oceanographic measurements were not part of datasets available for this work, modeling case studies are conducted to assess how changing atmospheric conditions impact the oceanic mixed layer.

2. *Shear instabilities are a key mechanism for vertical exchanges (mixing) in stratified atmospheric layers from ABL to middle atmosphere. (Addressed in Chapters 3, 4, & 5)*

Generally the middle atmosphere (≤ ~100 hPa) in nature is stably stratified so vertical transport is inhibited by density gradients. The velocity shear exerted by planetary waves can be effective in breaking up these layers and promoting vertical transport at scales ~ 1 km. On a different scale, (~10-100 m) in the lower atmospheric surface layer, SBL has profound influence on turbulence, and instabilities associated with local shear can be a key contributor to vertical transport. In both cases, turbulent mixing is effective when gradient Richardson numbers approaches between the critical values of 0.25 (linear theory) and 1.0 (nonlinear theory). Under such conditions instabilities, such as Kelvin-Helmholtz (K-H) billows, are generated that can cause significant vertical mixing (Strang and Fernando 2001a; De Silva et al. 1996). These instabilities lead to turbulent stirring and eventually to irreversible mixing between stratified layers no matter the scale. Observing these instabilities over the different scales available in datasets will highlight the wide-ranging roles these instabilities play in determining the atmospheric structure. As such, it is useful to evaluate the relationship between mixing parameters and governing quantities (e.g., Richardson number), a topic that has received much past attention (Lozovatsky and Fernando 2012; Pardyjak et al. 2002). However, the simultaneous, multi-scale measurements with shear introduced by different forcing mechanisms have received only scarce attention. The present study seeks to observe the breakdown mechanisms and, if possible, quantify mixing as a function of background parameters.

3. *Convective motions are a vertical exchange mechanism, quantification of which may require consideration of the roles of planetary waves in addition to contributions of surface thermal properties. (Addressed in Chapters 3 & 4)*

Deep and diurnal convection both play key roles in the tropics. Largescale deep convection in troposphere and smaller-scale convection in the CBL promote vertical transport via updrafts and downdrafts. In the CBL, moisture is transported rapidly upwards from the moist marine mixed layer under thermal forcing via convective motions leading to cloud formation. Deep convection can act as a fast, effective vertical exchange mechanism with vertical scales on the order of ~1-10 km, larger than in most shear instability-induced forcing or nominal thermal convection. Just as the vertical turbulence in the mixed layer results in near-constant wind velocity and temperature (Figure 1.1a), deep convection promotes vertical homogenization of properties, for instance, momentum, throughout lower to middle troposphere via turbulent mixing and entrainment in convective cells. While surface heating is certainly a principle source of convection with its persistent diurnal cycle in tropics, we hypothesize that pressure gradients induced by planetary waves may promote strong vertical motions, much the same as in thermally-driven deep convection. This possibility has been recently proposed as one mechanism for the initiation of active convection phase of MJO over Indian Ocean (Sakaeda and Roundy 2016; Powell and Houze 2015) and is advanced in this work.

1.5 Outline

The remainder of the thesis is organized as follows. In Chapter 2, the methodology used to acquire data is presented, including details of the field experiments (ASIRI-RAWI, MATERHORN-Technology) and public-access datasets consulted. Chapter 3 describes planetary waves observed during ASIRI-RAWI at larger scales, including their interactions with synoptic and mesoscale disturbances. The impacts of larger-scale disturbances on air-sea processes in the boundary layers are addressed in Chapter 4 using microscale resolution measurements (ABL) and model output (ocean). Even with the extensive ABL observations of ASIRI-RAWI, there were challenges to adequately measure small-scale mixing parameters beyond same limitations of past experiments so Chapter 5 presents a detailed study of mixing in stably stratified flows using a specialized instrument deployed during MATERHORN project, in which I also participated (Fernando et al. 2015). Finally, Chapter 6 concludes by summarizing the main outcomes of this work.

CHAPTER 2:

EXPERIMENTAL METHOD

2.1 Overview of ASIRI-RAWI

The ASIRI-RAWI project was designed to investigate Indian Ocean atmospheric phenomena at subseasonal and smaller scales, with the subtext of air-sea interactions and as part of the ONR research initiatives ASIRI and NASCar. An array of meteorological instruments, probing from the surface layer to lower stratosphere, captured a swath of space-time scales and provided measurements to study how the surface layer is impacted by waves and instabilities aloft. Targeted phenomena included oscillations on the order of 30-90 days (e.g. MJO) but the length of the campaign (~42 days) only allowed detailed studies of shorter intraseasonal scales such as quasi-biweekly oscillations as well as synoptic and mesoscale phenomena down to turbulence in the surface layer. To this end, instrumentation was deployed from 1 February through 15 March, 2015 in Seychelles (4°40'43.4'' S, 55°31'50.2 E), Sri Lanka (6°58'30.2"N, 79°52'12.8"E), and Singapore (1°17'57.1"N,103°46'16.5"E) to capture the propagation of subseasonal oscillations along and across the equator. Figure 2.1 illustrates the locations of the sites within the IO. At both Seychelles (Fig. 2.2) and Sri Lanka (Fig. 2.3) coastal sites, Radiometrics® microwave radiometers, Halo Doppler Lidars®, Vaisala® ceilometers, and 2-3 daily radiosondings provided vertical profiles of temperature, humidity, pressure, wind speed, wind direction, vertical velocity, and cloud intensity. The Singapore site featured a lidar, an Expeditionary Meteorological (XMET) sensor, and two daily soundings launched by Singapore's Meteorological Services. In addition, all sites had a flux tower (10-13 m) for momentum and heat flux measurements using three-dimensional (3D) sonic anemometers at multiple levels, and at two sites (Seychelles and Sri Lanka) infrared gas analyzers and net radiometers were also deployed for moisture flux and solar radiation measurements.

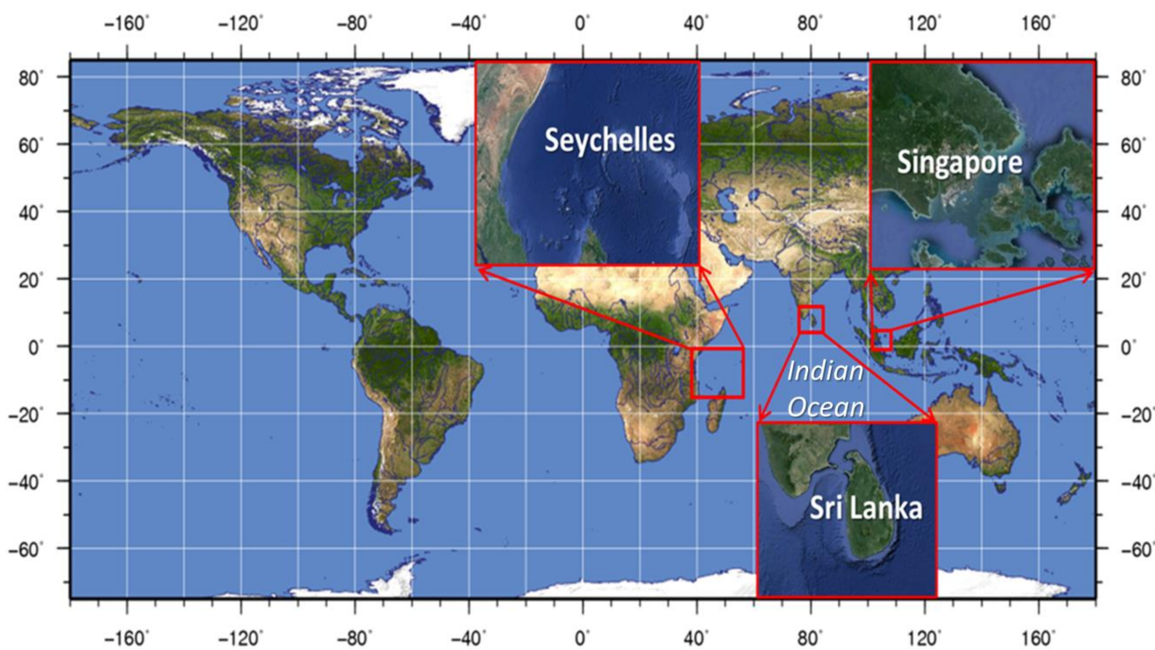

Figure 2.1: Global map on equirectangular projection with geographic coordinates depicting the three experimental locations in the Indian Ocean. Zoomed-in views show Seychelles, Sri Lanka, and Singapore along with surrounding seas.

The experiment was conducted during a period of year (February) when dry Kelvin wave climatology in the tropical tropopause layer often reaches a maximum (Suzuki and Shiotani 2008) so data coverage reaching middle atmosphere was needed to achieve full resolution of key intraseasonal phenomena. Most radiosondes reached altitudes between 20 and 30 km and thus could provide measurements of tropical tropopause layer. Additional valuable information was possible based on model reanalysis data. Technical details of the largescale data from radiosondes and reanalysis are provided in Section 2.2. Other instrument platforms mentioned here will be covered more in depth in Section 2.3. Section 2.4 introduces the novel hot-film sensor for fine-scale turbulence measurements that was used for analysis in Chapter 5.

Figure 2.2: Seychelles coastal experimental site adjoining Seychelles International Airport and southern Arabian Sea with key observational equipment labeled in red. In left panel are 10-m meteorological flux tower and Doppler lidar. In middle panel foreground are microwave (MW) radiometer and antenna for telemetric communication with radiosondes. In right panel is the Expeditionary Meteorological Ceilometer Enhanced (XMET-CX) sensor.

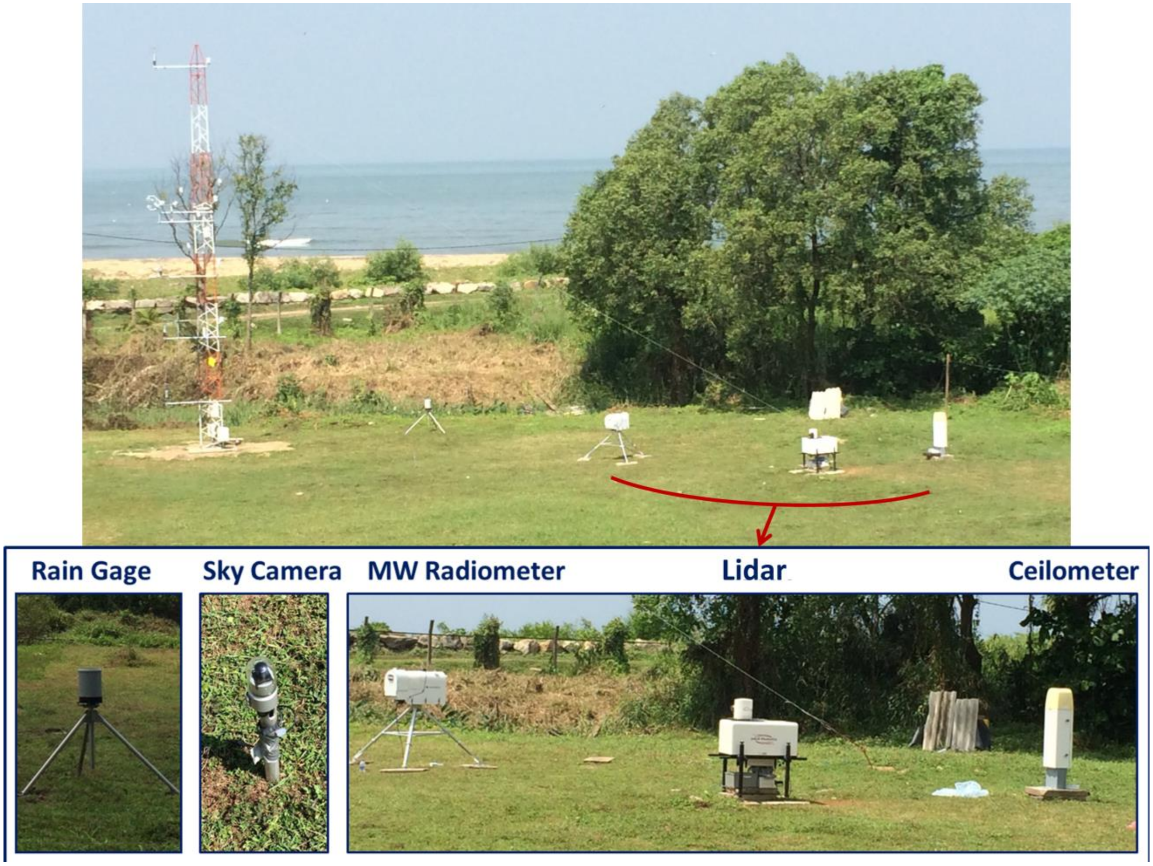

Figure 2.3: Sri Lanka coastal observational site adjoining National Aquatic Resources Research Agency (NARA) headquarters and Laccadive Sea. Upper panel has site overview with 13-m flux tower to the left. In lower panel are zoomed-in views of rain gage, sky camera, and remote sensors (MW radiometer, lidar, and ceilometer).

2.2 Largescale Datasets

2.2.1 Radiosondes

Radiosondes are operationally launched daily from thousands of locations around the world with the most common release times being at 0000 and 1200 UTC. They typically measure vertical profiles of temperature, relative humidity, pressure, and horizontal winds, and the collected data play an important role in global and regional weather forecasts by providing some initial conditions for model runs. Each site in

ASIRI-RAWI was serviced by local meteorological organizations that operated regular soundings at frequencies ranging from 4-5 times per week (Sri Lanka) to twice daily (Singapore). ASIRI-RAWI resources and personnel allowed an increase to the rate of radiosonde launches at Sri Lanka and Seychelles to 2-3 times daily. Figure 2.4 shows project participants launching radiosondes at Seychelles and Sri Lanka, which were the World Meteorological Organization (WMO) stations 63985 and 43466, respectively.

Figure 2.4: Radiosondes being launched in Seychelles (left and right) and Sri Lanka (middle) by ASIRI-RAWI participants (right photo credit: Joe Laurence, Seychelles News Agency).

The radiosonde data were collected with vertical resolutions of 5-10 m as opposed to coarse resolution (~100 m) available through public repositories from the WMO. In Seychelles, 0000 UTC soundings were conducted by National Meteorological Services using Vaisala® RS 92-SGP sondes and MW41 sounding system. This was augmented by 0600 and 1200 UTC soundings using a combination of Vaisala® RS 90-AG sondes with MW31 sounding system and RS 92-SGP sondes. Meteorological Services Singapore also used RS 92-SGP radiosondes with a MW41 sounding system for two daily radiosonde launches at 0000 and 1200 UTC (WMO station 48698). The Sri Lanka Department of Meteorology conducted 4-5 radiosonde launches per week with a their own Meisei Electric® sounding system and collaborated with University of Notre Dame (ND) to release one InterMet Systems® (iMet-1) radiosonde daily with the ND-owned iMet-3200A sounding system.

In Seychelles, fifteen simultaneous launches with both sonde types (RS 90-AG and RS 92-SGP) were conducted to test the ability of different systems to produce similar results. All vertical profiles (from both sonde types) were bin-averaged to 25-m to minimize the effects of sensor noise and because vertical positioning from GPS can have uncertainty of up to 20 meters so presenting observations over any smaller vertical scales may misrepresent accuracy. The mean absolute difference in measurements between the two systems for the 15 dual launches is shown in Table 2.1 below. The differences were less than 1 hPa, 1 °C, and 1 m/s for pressure, temperature, and wind speeds, respectively. For relative humidity, the difference of 5% is more substantial compared to the range of measurements (0-100%) but arises due to the limitations of the sondes' relative humidity probe which has a resolution of only 2% and uncertainty of 5%. The relatively small differences in all measured variables were acceptable for our applications and supported the use of radiosondes for analysis and comparisons presented in Chapter 3. The general agreement of the two sonde types was expected due to similar sensor hardware. A more detailed past study by Italian Air Force comparing these two sonde types had also demonstrated their inter-comparability (Leccese 2004). Unlike this Italian experiment which launched sondes attached to the same balloon with specialized equipment, we launched separate balloons (see Figure 2.5) so the comparison was essentially of two Lagrangian particles released at points close in time and space. The comparisons therefore did not represent the exact same air volume — in fact separations of up to several hundred meters could occur — and some disagreement in results was expected naturally for this reason.

TABLE 2.1

MEAN ABSOLUTE DIFFERENCES IN DUAL-LAUNCHED RADIOSONDES WITH TECHNICAL ACCURACY AND RESOLUTION SPECIFIED FOR RS 92-SGP SONDES

Variable	**Mean Absolute Difference**	**RS 92-SGP Measurement Uncertainty (<100 hPa)**	**RS 92-SGP Measurement Resolution (<100 hPa)**
Pressure (hPa)	0.7	1	0.1
Temperature (°C)	0.9	0.5	0.1
Relative humidity (%)	5	5	1
Zonal wind (m/s)*	0.7	0.15	0.01
Meridional wind (m/s)*	0.7	0.15	0.01

*Calculated based on measured wind speed and direction

Figure 2.5: ASIRI-RAWI participants preparing for dual launch of Vaisala® RS 92-SGP and RS 90-AG sondes (photo credit: Joe Laurence, Seychelles News Agency).

Determination of quantities such as vertical shear and Brunt-Väisälä frequency based on radiosonde data required calculation of vertical gradients of the measured variables. Prior to these calculations, profiles were smoothed using a Gaussian filter with a 250-m window, and then gradients were obtained using second-order accurate finite difference methods. Owing to inherent noisiness of second-order methods, 25-m resolution results were bin-averaged further for presentations in figures.

2.2.2 Reanalysis datasets

Reanalysis datasets were utilized to expand the spatial and temporal range of the field campaign, especially above the lower troposphere where 2-3 instantaneous profiles from radiosondes were available at only few locations every day. Long-term reanalysis datasets, which are widely used for climatological information (e.g. Kravtsov et al. 2014), can also be used for understanding atmospheric dynamics on shorter time scales (Powell and Houze 2015), as in our application. To create reanalysis datasets, observational data assimilation along with past forecasts (or hindcasts) are used to solve an ill-posed inverse problem that nudges gridded data to a best-guess approximation of the global (or regional) atmospheric state (Dee et al. 2011). While reanalysis can have near-observational accuracy, especially where plentiful accurate observations are available to assimilate, caution should be taken when utilizing them because of the general lack of information regarding the uncertainty of reanalysis data in absence of observational comparisons (Parker 2016). Notwithstanding, reanalysis can be a valuable tool when used to corroborate and enhance real observational datasets.

In the past two decades there have been several reanalysis datasets made available to the public by different meteorological agencies and research institutions. Some of these datasets span through near-present day so were applicable for the ASIRI-RAWI project. These include the pioneering National Centers for Environmental Protection/National Center for Atmospheric Research (NCEP/NCAR) Reanalysis 1 (Kalnay et al. 1996), the European Centre for Medium-Range Weather Forecasts (ECMWF) Re-Analysis Interim (ERA-I; Dee et al. 2011), and the Modern-Era Retrospective Analysis for Research and Applications (MERRA) from National Aeronautics and Space Administration (NASA; Rienecker et al. 2011). The more recently released reanalysis datasets, including ERA-I and MERRA, are significant improvements over classical NCEP/NCAR's datasets. While even the highest resolution reanalysis datasets still have challenges in accurately representing high-frequency equatorial wave activity (Kim and Alexander 2013), most datasets are quite adept at capturing the larger-scale Kelvin wave activity, which is the most energetic tropical wave component (Žagar et al. 2009). The ERA-I dataset from ECMWF was primarily utilized in subsequent analyses (ECMWF 2009). By having a horizontal resolution of 0.703°×~0.702° near the equator, it is one of the finest resolution present-day datasets available and is widely cited in tropical meteorology literature.

2.2.3 Satellite observations

Meteosat-7, a geostationary meteorological satellite, provided primary coverage for Indian Ocean during the field campaign. It was part of the first generation of Meteosat satellites operated by the European Organisation for the Exploitation of Meteorological Satellites (EUMETSAT), which were each equipped with Meteosat Visible and Infrared Imagers to measure the visible, infrared, and water vapor portions of the electromagnetic spectrum. For tropical meteorology, the brightness temperature derived from infrared measurements is an important variable and was the main satellite variable consulted in this work. Brightness temperature is directly related to the cloud coverage over an area due to convection and thus the outgoing longwave radiation (OLR), an important parameter in global climate studies. The satellite-observed OLR is used as a variable in the most popular MJO index, the Real-Time Multivariate MJO Index (RMM; Wheeler and Hendon 2004), and therefore the RMM constitutes an indirect satellite observation. RMM index (available at http://www.bom.gov.au/climate/mjo/) was checked for the campaign time frame, and it suggested that MJO was not a significant factor. No strong MJO meant that smaller-scale (<30 day) planetary waves for which the ASIRI-RAWI campaign was designed would be more pronounced. The main satellite data resources that were utilized for the analysis in this work were the Meteosat-7 based data products from the Cooperative Institute for Meteorological Satellite Studies at the University of Wisconsin-Madison (http://tropic.ssec.wisc.edu/tropic.php) and from EUMETSAT via the Earth Observation Portal (http://archive.eumetsat.int/usc/).

2.3 In-situ Observations

2.3.1 Microwave radiometer

Two MP-3000A Microwave (MW) Radiometers were deployed at part of the ASIRI-RAWI campaign in February and March 2015. One radiometer (ND-owned) was positioned at NARA headquarters in Colombo (see Fig. 2.3); the was other owned by the National Oceanic and Atmospheric Administration (NOAA) and positioned at Seychelles International Airport (see Fig. 2.2). The MW radiometers provided information on temporal variation of temperature, relative humidity, water vapor, and liquid water in atmosphere from surface layer to altitude of 10 km. This information is important because a radiosonde, on the other hand, could only provide an instantaneous measurement of the atmospheric conditions as balloon moved with wind. MW radiometers scan three profiles – vertical zenith, 20°N off-zenith, and 20°S off-zenith – every three minutes so the temporal evolution of atmospheric conditions within three separate fixed volumes can be observed at relatively high frequency. Radiosondes do have some advantages such as farther vertical range (into stratospheric layer), finer vertical spatial resolution, and higher accuracy. Radiosonde output should be considered the measurement "truth" rather than MW radiometers because radiometers convert microwave signal retrievals (in frequency bands 22-30 GHz and 51-59 GHz) to the relevant variables based on several assumptions and utilizing an artificial neural network, which was trained by past radiosonde data at the sites. Therefore, temperature and relative humidity profiles from radiosondes and microwave radiometer during soundings were compared to assess radiometer's ability to accurately replicate the atmospheric conditions measured by radiosondes.

At Seychelles site, the microwave radiometer and radiosonde system were located in close proximity as shown in Figure 2.2 so this site was selected for initial comparisons. In Sri Lanka, it was necessary to release radiosondes at the Department of Meteorology site ~5 km from NARA site so slight horizontal inhomogeneity of surface (which was indeed the case) was potentially responsible for some disagreement rather than the radiometer's inaccuracy, especially at lower levels. For Seychelles data, systematic comparisons of temperature and relative humidity profiles were completed by bin-averaging the radiosonde data to the vertical resolution of radiometer which was 50 m between the ground and altitude of 0.5 km, 100 m between altitudes of 0.5 and 2 km, and 250 m between altitudes of 2 and 10 km. Example comparison plots are shown in Figure 2.6 for one representative day. The zenith and 20° off-zenith scans were averaged for approximate 1-hour duration of soundings to produce profiles for the comparisons. Some features typical of the MW radiometer's performance were highlighted by Figure 2.6, including the close agreement for temperature and lesser agreement for relative humidity. The MW radiometer has particular difficulty estimating layers of very dry air above the moister layers because, while it has a mechanism for approximating cloud bottom height, it lacks robust capability to measure cloud top height and cloud thickness. Nonetheless, the MW radiometer was able to capture the general trends of the relative humidity profiles and is certainly fit for qualitative analyses and guided quantitative analyses.

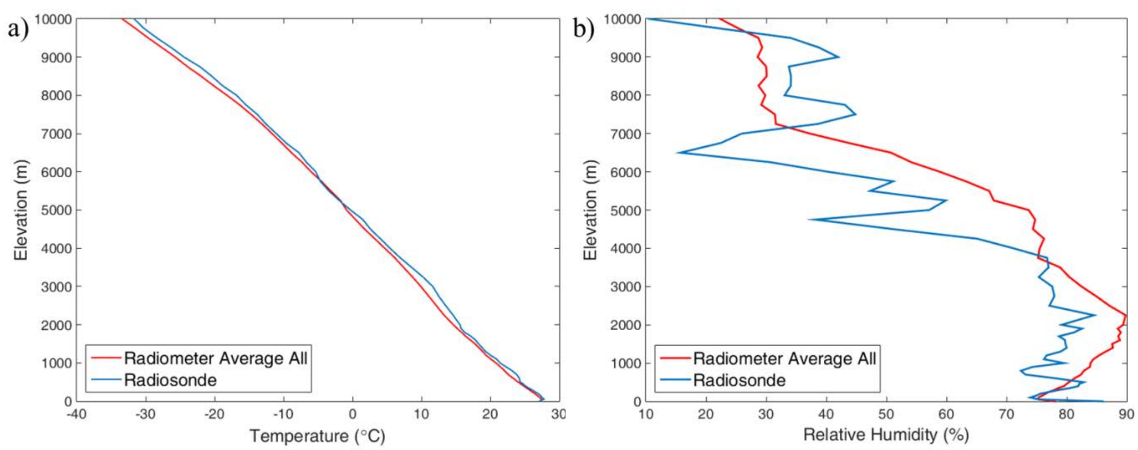

Figure 2.6: Radiosonde vs. MW radiometer observations at Seychelles for 1200 UTC on 16 February: (a) temperature and (b) relative humidity.

The statistical analysis was completed for comparisons between 97 soundings at the Seychelles site during experimental campaign while MW radiometer was in operation. The radiometer's errors were assessed as the difference from radiosonde output at each level and are shown in Table 2.2. The average errors for the full 10-km profile exceed average errors below 2 km, where MW radiometer has highest vertical spatial resolution of 50 to 100 m. Within these lower levels which include atmospheric boundary layer, errors remained below 1°C for temperature and 10% for relative humidity with a high level of confidence. MW radiometers were therefore an effective method for observing heat and moisture in ABL with a high temporal resolution, which was unobtainable from radiosondes without prohibitive financial costs. The performance of the MW radiometers could be improved using radiosonde data collected during the 2015 experiment to train a new neural network and reprocess data.

TABLE 2.2

MW RADIOMETER AVERAGE ROOT MEAN SQUARE ERROR AND MEAN ABSOLUTE ERROR IN REPLICATION OF RADIOSONDE PROFILES OF TEMPERATURE AND RELATIVE HUMIDITY

	Root Mean Square Error		**Mean Absolute Error**	
	All Levels	*<2 km*	*All Levels*	*<2 km*
Temperature (°C)	1.28	0.81	1.06	0.68
Relative Humidity (%)	14.9	8.4	11.3	6.4

2.3.2 Lidar

Lidar (light detection and ranging) is a widely used and relatively recent technique for ground-based remote sensing of the atmosphere, and the general details of lidar measurement are given below to provide background for its application in ASIRI-RAWI. The operation of lidar in atmospheric conditions takes advantage of the fact that the real atmosphere is filled with solid and liquid particles of various sizes (i.e. aerosols).

These particles ranging from molecules to submicronic aerosols to hygrometers like ice crystals and water droplets scatter or absorb any light travelling around them. Lidar systems emit pulses of light (beams) into the atmosphere and measure the amount of light that returns to lidar's receiver due to backscatter. As the light is sent out at discrete pulses of suitable frequency and wavelength, the returning backscattered light can be collected by a receiver in discrete periods. These periods can be related to an actual distance because the beam is travelling at the speed of light. Based on these distances the data can be broken down into range gates to give clear picture of aerosol characteristics at different radial distances along beam. Coherent Doppler lidar was the type applied during ASIRI-RAWI, which measures radial velocity. As the laser beam travels through the atmosphere and is scattered by particles travelling with velocity of air, a Doppler frequency shift is imparted to the scattered light. The receiver is able to measure this frequency shift in order to record the radial velocity of particles moving with air flow along the beam. For most Doppler lidar systems the beam is not limited to a stationary path; the emitter can rotate (scan) and pivot in order to give 2D and quasi-3D information about atmospheric flow velocity.

Three Doppler lidars were deployed, one at each site, during ASIRI-RAWI. Two Halo® Scanning Doppler Lidars were deployed: one owned by ND was at Sri Lanka site (see Fig. 2.3), the other owned by Army Research Laboratory (ARL) at Seychelles. The Singapore site featured an ARL-owned Leosphere® Doppler Lidar. The main Lidar-measured variable of interest was the vertical velocity because of its importance for tropical convection and its unavailability from other observations. Radiosondes did not directly measure vertical velocity, and the point measurements from 3D sonic anemometers on towers were not an ideal source of mean vertical velocity component (compared to horizontal components) because of possible interference of the anemometer and tower supports as well as closeness to the ground. The main data processing was completed for Seychelles Lidar, and, with the aid of Dr. Yansen Wang from ARL, the 1200-1600 upward-looking beam readings per hour (~25-30% of total measurements) were constructed into hourly-averaged vertical velocity profiles. Limited by the aerosol availability in marine/coastal boundary layer, the Lidar could only provide vertical velocity measurements up to ~900 m. Data from a rain gage deployed near the Lidar was utilized to identify rainy periods when Lidar measurements would be corrupted, and they were removed from the final dataset.

2.3.3 Ceilometer/XMET

In Seychelles, an Expeditionary Meteorological Ceilometer Enhanced (XMET-CX) sensor was set up during the field campaign and has been continuously operating there ever since (see Fig. 2.2). This specialized sensor was developed by the Coastal Observing Research and Development Center at the University of California, San Diego in collaboration with the United States Navy. The ceilometer component was a Vaisala® CL31, which operated using similar principles as lidar. Backscatter from an upward-looking, fixed electromagnetic (infrared laser) beam was used to detect cloud base heights and vertical visibility. The XMET component consisted of Vaisala® sensors to measure standard meteorological variables at ground level (2-3 m), including horizontal wind speed and direction, temperature, relative humidity, barometric pressure, and visibility. Many of these variables were also available from meteorological tower discussed below and the comparability between the two sets of data was good. A second XMET sensor (*sans* ceilometer) was deployed at the Singapore site during the campaign, and a second CL31 ceilometer at the Sri Lanka site.

2.3.4 Meteorological flux tower

Each site was equipped with a multi-level meteorological flux tower to measure near-surface vertical fluxes of momentum, heat, moisture, and short/longwave radiation as well as standard meteorological variables. For velocity, YOUNG® Model 81000 Ultrasonic Anemometers collected data at 20 Hz frequency. Wind speed and direction, respectively, were measured with resolutions of 0.01 m s^{-1} and 0.1° and accuracies of ±1% and ±2°. The sonic (virtual potential) temperature was derived from measured speed of sound with resolution of 0.01°C and accuracy of 2°C. The other high-frequency (20 Hz) observations for flux calculations were water vapor and carbon dioxide concentrations from LI-COR® LI-7500A Open Path CO_2/H_2O Gas Analyzers; their specifications are not listed here because instrument was mainly used and trusted for turbulent fluctuations of water vapor and not mean quantities. The variability of mean moisture and temperature was tracked at 1 Hz frequency using Campbell Scientific® Model HC2S3 Temperature and Relative Humidity (T/RH) probes. The probe used a capacitance hygrometer for relative humidity measurements with an accuracy of ~0.8% and a thermistor for temperature measurements with an accuracy of ~0.1°C. Secondary temperature measurements were also obtained from thermocouple(s) on each tower. Kipp & Zonen® CNR4 Net Radiometers measured (at 1 Hz) the upwelling and downwelling radiative fluxes, both shortwave and longwave. Uncertainty for the daily integrated shortwave and longwave radiation values was <5% and <10%, respectively.

Each tower was configured differently based on local site conditions and limited availability of resources. In Seychelles, substantial vegetation removal was required at the site to reduce surface roughness for measurements; Figure 2.2 was taken following these efforts. The tower had two levels, 2 and 10 m, with sonic anemometer, LI-7500A probe, and T/RH probe. At 10-m height, there were also a thermocouple and net radiometer.

The Sri Lanka site had a 13-m tower with more levels for instrumentation. At 2, 4, 6, 8, and 12 m were sonic anemometers and thermocouples. T/RH probes were also at each of these levels except at 2 m. The 8-m level was the most instrumented with the addition of an LI-7500A probe and net radiometer.

The 10-m meteorological tower in Singapore had two levels of instruments like Seychelles tower with bottom level moved up to 5 m due to higher urban surface roughness (see Fig. 2.7). There was a sonic anemometer and T/RH probe at each level (5 and 10 m). In addition there was a thermocouple (2 m), but otherwise the tower in Singapore was the least equipped.

All locations also had a rain gage near the tower to measure precipitation rate in mm hr^{-1} and a barometer for air pressure. Data were collected and stored by Campbell Scientific® data loggers at each site. Once collected, the data from sonic anemometers was processed using eddy covariance techniques to calculate the vertical momentum and kinematic temperature fluxes. At Seychelles and Singapore, the additional instrumentation allowed for the calculation of moisture and radiative fluxes as well obtaining a near-complete picture of the surface energy budget (see Chapter 4). Only the towers at Seychelles and Sri Lanka supplied the ABL surface measurements for Chapter 4 because of dense instrumentation deployed in these locations, and Singapore was anticipated to have a very strong urban influence as shown in Figure 2.7.

Figure 2.7: Singapore meteorological flux tower in dense urban setting.

2.4 MATERHORN 'Combo' Probe Deployment

As a part of the MATERHORN field campaign (Fernando et al. 2015), a series of five flux towers were deployed along the eastern slope of Granite Mountain located in the U.S. Army Dugway Proving Ground in Utah (Fig. 2.8a). Each tower was instrumented with multiple levels of sonic anemometers, temperature/relative humidity sensors, and thermocouples. Mounted on one of the towers, called ES2 (Fig. 2.8b) were sonic anemometers at 0.5 m, 4 m, 10 m, 16 m, 20 m, 25 m, and 28 m heights and thermocouple (temperature) probes at 0.5 m, 1 m, 3 m, 5 m, 7 m, 10 m, 13 m, 16 m, 20 m, 23 m, 25 m, and 28 m. At 6-m height, two specially designed unique probe systems, dubbed 'combo' probes, were deployed as a part of the MATERHORN-Technology initiative. Each consisted of a sonic anemometer and constant-temperature hot-film probes arranged in a three-dimensional (double-X) sensing probe configuration. The hot films were located within the probe volume of the sonic anemometer. The hot-film probe of the combo was pivoted on a precision-motorized gimbal that could rotate to align the probe tip with the direction of oncoming winds detected by the sonic anemometer. Approximate alignment of the probe with the mean winds is a requirement for accurate hot-film measurements. The sonic anemometer measured the three components of mean winds and turbulence (resolution ~ 10 cm), and these measurements were used to calibrate the hot film (resolution ~ 1 mm) that could measure down to Kolmogorov scales. The resolution of the composite hot-film probe was ~ 0.7 cm. The two combos were positioned on opposite sides of the tower so that only one of them could effectively record oncoming wind with hot film at any given moment (see below). More details of the combo probes are given in Kit et al. (2010, 2017). Application of combo measurements to the problem of vertical mixing efficiency in ABL is covered in Chapter 5. Because the deployment of combo probes was logistically prohibitive at ASIRI-RAWI sites, for the analysis of mixing efficiency the data from idealized cases during MATERHORN experiment were used.

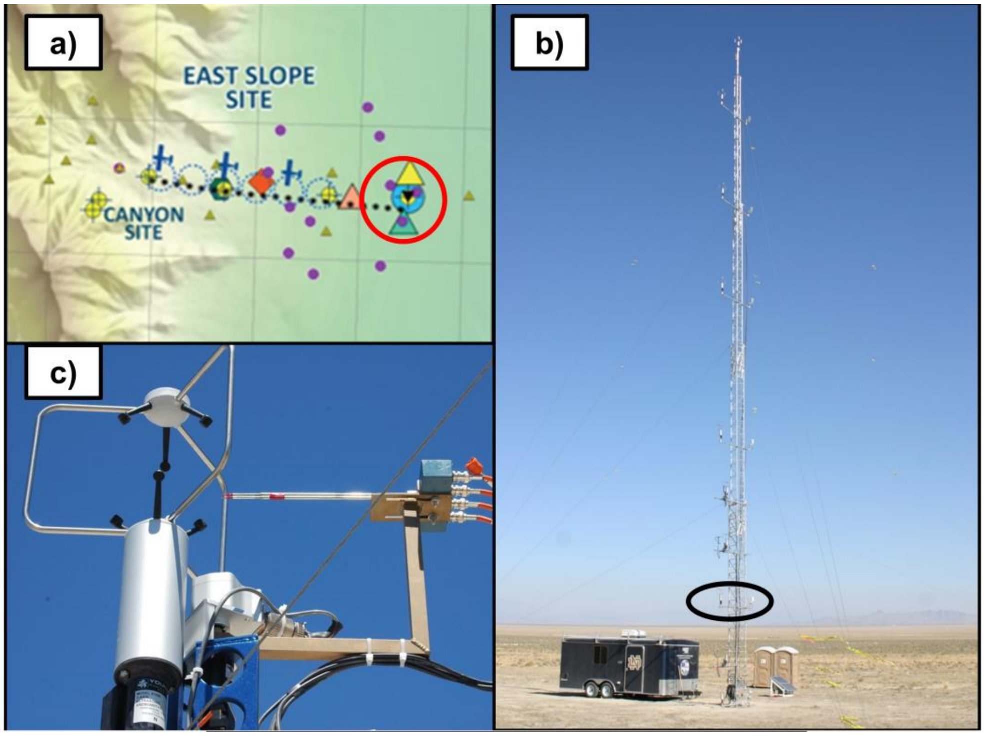

Figure 2.8: MATERHORN experimental overview for 'combo' probe deployment: (a) Topographical map provides a view of the experimental site on the east slope of Granite Mountain in Dugway, Utah. The tower with combo probe was located within the red circle, and all other symbols denote locations of various meteorological instrument systems – for details see Fernando et al. (2015). (b) 28-m meteorological tower at Dugway, Utah instrumented with multiple levels of sonic anemometers, thermocouples, and other sensors. Black ellipse indicates location of combo probes on 19 October, 2012, the day that data reported in Chapter 5 were collected. Note that the combo probes were pointed in opposite directions so that during the measurements one was windward of the tower and the other leeward; all results presented in this thesis are from windward probe (hot film or sonic) unless noted otherwise. Structures in the background were located to minimize their wake effects on the tower. (c) Combo probe with sonic anemometer to left and hot-film attached to rotating gimbal on the right.

CHAPTER 3:

EQUATORIAL KELVIN WAVES IN LOWER STRATOSPHERE AND UPPER TROPOSPHERE

3.1 Literature Review

The equatorial planetary waves discovered by Matsuno (1966) and introduced in Chapter 1 (Eqs. 1.1-1.8), to the first-order, provide a good description of weather-climate variability of the tropics. Eqs. 1.1-1.3 are valid for an idealized barotropic environment with a vertically homogeneous layer of fluid so some adjustments to the governing equation are needed to achieve realistic solutions for real (stratified) atmosphere. In this formulation, vertical velocity component w is introduced as an unknown variable via both the anelastic continuity equation and the conservation of energy equation for density stratified flows (Andrews et al. 1987), which are, respectively,

$$\frac{\partial u}{\partial x}+\frac{\partial v}{\partial y}+\frac{1}{\rho_o}\frac{\partial(\rho_o w)}{\partial z}=0 \tag{3.1}$$

and

$$\frac{\partial^2\phi}{\partial z\partial t}+wN^2=0, \tag{3.2}$$

where ρ_0 is the reference density (Boussinesq approximation) and N the Brunt-Väisälä frequency. If one assumes that N is constant with height, Eqs. 3.1 and 3.2 can be combined to eliminate w and write

$$\frac{\partial}{\partial t}\left[\frac{1}{\rho_0}\frac{\partial}{\partial z}\left(\rho_0\frac{\partial \phi}{\partial z}\right)\right] - N^2\left[\frac{\partial u}{\partial x} + \frac{\partial v}{\partial y}\right] = 0, \tag{3.3}$$

which replaces Eq. 1.3 of the governing set of equations and introduces vertical structure to the solutions; the horizontal structure of these waves is not altered by these theoretical adjustments. Some of the first observed equatorial waves in lower stratosphere had tilted vertical structures (Yanai and Maruyama 1966; Wallace and Kousky 1968), as evidenced by radiosonde measurements. Radiosondes with their high vertical resolution are particularly adept at detecting the 'dry' waves of the upper troposphere and stratosphere where strong stratification limits vertical wave length and exaggerates their tilted vertical structure, while horizontal structure is inferred by applying a Doppler shift to measurements from stationary observational points or by comparing observations from proximate sounding sites. These dry waves are studied for their role in stratospheric variability (Holton and Lindzen 1972) and stratosphere-troposphere exchange (Holton et al. 1995).

The horizontal structure of the equatorial waves is better detected by gridded observations such as satellites. Although some early satellite studies were able to detect propagating wavelike disturbances which had a convective component (e.g. Reed and Recker, 1971), the accumulation of bigger and better datasets facilitated the identification of Matsuno's waves within tropical convection signals (Takayabu 1994a; Wheeler and

Kiladis 1999; Cho et al. 2004). These studies produced space-time spectra (Hayashi 1977) based on improved satellite data which demonstrated the existence of convectively-coupled wave types analogous to several of those predicted by Matsuno's (1966) wave dispersion equations (curves in Figure 3 of Matsuno article). The horizontal dispersion curves of the various wave modes are shown in Figure 3.1 (reproduced from Kiladis et al. 2009). Note that the convectively-coupled waves in real troposphere exhibit slower wave speeds, or smaller equivalent depths, than dry stratospheric equatorial waves and theoretical predictions, which has been attributed to the neglect of moist, diabatic processes in derivations. Additionally, small departures from predicted curves may be due to Doppler shifting of waves in the strong, heterogeneous background winds of troposphere (Dias and Kiladis 2014).

All wave modes predicted by Matsuno's linear theory (Fig. 3.1) are progressive, equatorially trapped (or meridionally evanescent; see Eq. 1.7) waves. Their dispersion relations are plotted in wave number-frequency space and may be identified based on the direction of phase propagation, either eastward ($k^* > 0$) or westward ($k^* < 0$). Note that in this thesis the phase propagation velocities are denoted as eastward/westward, but the actual velocities of fluid parcels are defined as westerlies for west-to-east flow and easterlies for east-to-west flow. Besides direction of propagation, different restoring forces also distinguish the wave types. The (planetary) Rossby waves in lower left corner of the diagram exist due to conservation of potential vorticity on long time scales. Here the strong latitudinal planetary vorticity gradient near the equator, known more precisely as beta-effect, is balanced by the inertial forces. Planetary Kelvin waves have a kindred balance between beta-effect and inertial forces, but they propagate in opposite direction (eastward) and have special characteristic of no meridional motions. The stratification, which is the principal restoring mechanism for internal gravity waves, is increasingly important in equatorial mixed Rossby-gravity waves and inertio-gravity waves with (inertial) Coriolis effects also playing a role. Both Kelvin and inertio-gravity waves asymptotically approach a constant phase velocity, which is the shallow water wave velocity $c = \pm\sqrt{gH_o}$.

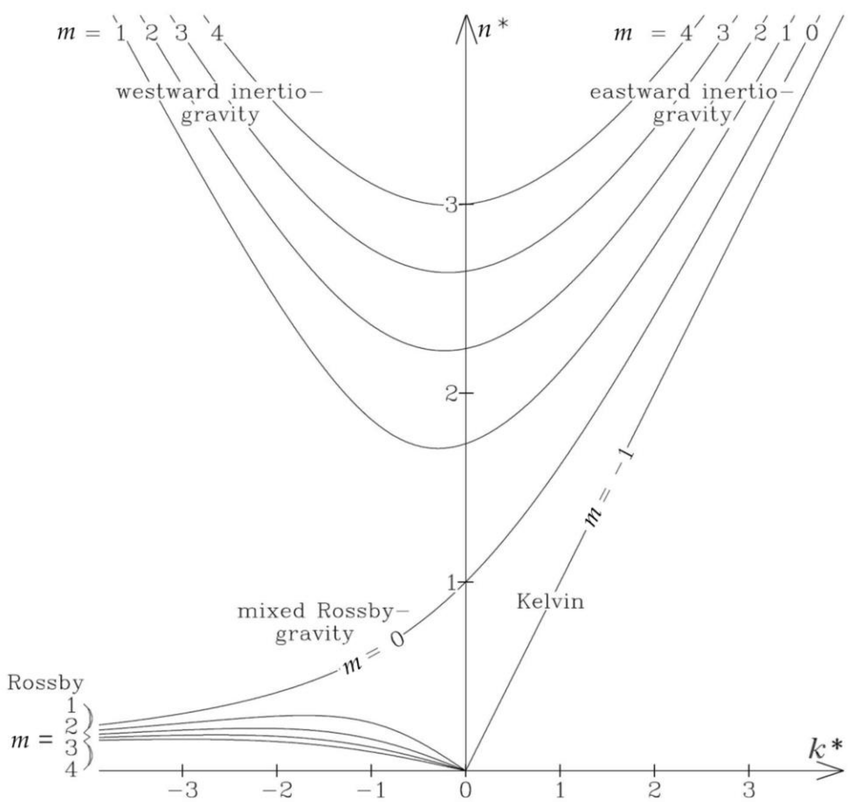

Figure 3.1: Dispersion curves for Matsuno's equatorial waves on a beta-plane taken from Kiladis et al. (2009) with some modifications. m is the meridional mode number, as in Eq. 1.6 and as discussed in the following subsections, extending from most commonly observed m=1 up to m=4. The axes are in nondimensional wave number $k^*=k(\sqrt{gH_o}/\beta)^{1/2}$ and wave frequency $n^*= n/(\beta\sqrt{gH_o})^{1/2}$.

The following subsections highlight key features from each of the observed atmospheric wave types in Figure 3.1. These include the westward and eastward inertio-gravity waves (m=1,2,…), equatorial Rossby waves (m=1,2,…), and the so-called mixed Rossby-gravity wave (m=0). The special solution known as equatorial Kelvin wave, assigned as meridional mode m=-1 for convenience, does not come from Eq. 1.6 and has received extended treatment in final subsection due to its importance for this work.

3.1.1 Westward and eastward inertio-gravity waves

The westward inertio-gravity waves (m=1) were first identified and analyzed by Takayabu (1994b) as connected to the westward-propagating convective disturbances that had been described earlier, particularly in tropical western Pacific (Nakazawa 1988). Subsequently, the TOGA COARE experiment provided a dataset rich with examples of westward inertio-gravity waves, allowing for detailed studies of their structure and behavior (Takayabu et al. 1996; Haertel and Johnson 1998). These waves have zonal wind in-phase with pressure anomalies and in quadrature with temperature and meridional wind, and, since wave periods are 1-3 days, they are referred to as (quasi) 2-day waves or disturbances. While these short-period, westward-propagating waves were known for their presence within the envelope of larger-scale MJO (Takayabu 1994b; Kiladis et al. 2009; Nakazawa 1988), the CINDY2011/DYNAMO experimental dataset provided stronger evidence and allowed more detailed studies (Zuluaga and Houze 2013), including on their role in MJO initiation (Kubota et al. 2015). In addition to in-situ measurements from these experiments, improved satellite and reanalysis have allowed more careful analysis of these waves' convective structures over extended periods, for instance, in 2000-2009 (Sumi and Masunaga 2016). Most of the literature reviewed here has focused on the *m*=1 inertio-gravity wave mode, but the *m*=2 mode has also been observed, as evident in space-time spectra (Kiladis et al. 2009).

Eastward inertio-gravity waves (*m*=1) are neither frequently referenced in the literature nor did they appear to have a peak in space-time spectra of Kiladis et al. (2009). Nonetheless, they exist (Yang et al. 2003, 2007; Pires et al. 1997), except not in western equatorial Pacific and some other regions. The reason for regional biases for certain equatorial inertio-gravity waves, e.g., the preponderance of westward inertio-gravity in western Pacific or during the MJO peak phase, is possibly related to the background state of zonal flow. Eastward inertio-gravity waves show preference for regions of strong easterly flow (Yang et al. 2007). The background winds may also determine how equatorial inertio-gravity waves interact with upper layers of the atmosphere. While so far this review has focused on convectively-coupled modes of inertio-gravity waves, their dry modes in upper troposphere and lower stratosphere have been known and studied for just as long. Early observations of westward inertio-gravity waves implicated them in upward transport of momentum affecting the quasi-biennial oscillation (QBO) in lower stratosphere (Maruyama 1994; Tsuda et al. 1994a). Eastward inertio-gravity modes may contribute more to QBO in regions where upper-tropospheric easterly winds may prevent westward waves from propagating into stratosphere (Sato and Dunkerton 1997) due to critical layer absorption when phase velocity equals the background wind velocity. Throughout both the troposphere and the stratosphere, the equatorial inertio-gravity waves have been found to play important roles in the weather and climate dynamics.

3.1.2 Equatorial Rossby waves

Equatorial Rossby waves (m=1) have a unique appearance among equatorially-trapped waves as a pair of cyclones straddling the equator (see Figure 3e of Kiladis et al. 2009). Rossby waves, among others, were first identified in space-time spectra of a decadal dataset by Takayabu (1994a), and again TOGA COARE immensely helped experimental studies on the behavior of these waves (Pires et al. 1997; Kiladis and Wheeler 1995). Regional variability is stronger for Rossby waves than other equatorial wave modes. In central Pacific, they are weakly convectively-coupled and nearly barotropic in their vertical structure over the central Pacific, but over western Pacific warm pool they are strongly coupled with convection with baroclinic (tilted) structure (Wheeler et al. 2000). Rossby waves have periods of 10-40 days and wave lengths up to ~10,000 km and thus can have major impacts on intraseasonal time scales of variability. The quasi-biweekly oscillation (QBWO) with its influence on Asian monsoon may originate as a convectively-coupled Rossby wave (Chatterjee and Goswami 2004; Chen and Sui 2010). Rossby waves may also have a role in MJO preconditioning (Gottschalck et al. 2013) and tropical cyclogenesis (Schreck and Molinari 2009).

3.1.3 Mixed Rossby-gravity waves

At m=0, one of the roots of Eq. 1.6 is neglected and a special-case solution forms a continuum though k^*=0 (Figure 3.1). One branch is a westward-propagating mixed

Rossby-gravity type wave, and the other is of the eastward inertio-gravity type. While the latter is sometimes classified with inertio-gravity waves (Section 3.1.1) recent research has shown close linkages between the two types across their shared part of space-time spectral space (Kiladis et al. 2016; Dias and Kiladis 2016). Generally though the eastward type has received limited attention (Yang et al. 2007) compared to the westward-propagating mixed Rossby-gravity type, which was the first equatorial wave ever observed in the stratosphere (Yanai and Maruyama 1966), contemporary with Matsuno's (1966) theoretical discovery and is dealt with in this review. These waves are prevalent in upper troposphere through stratosphere where they may influence QBO (Sato and Hirota 1994 and references therein) like inertio-gravity waves and Kelvin waves (see below).

While dry modes in the upper levels may or may not be coupled with convection, mixed Rossby-gravity waves in troposphere have been strongly linked to convection and cloudiness (Zangvil and Yanai 1981; Takayabu 1994a). Like the westward inertio-gravity waves and Rossby waves they show a regional preference for central and western Pacific, but they are observed in all equatorial convergence zones throughout the year with a seasonal peak in boreal summer (Wheeler and Kiladis 1999; Wheeler et al. 2000). Vertically, the mixed Rossby-gravity waves resemble the westward inertio-gravity waves in the troposphere but with important distinctions in the horizontal since westerly zonal winds are in-phase with high pressure in the mixed Rossby-gravity waves – the opposite is the case in westward inertio-gravity waves. Wave periods are usually 3-5 days, falling in between equatorial Rossby and inertio-gravity waves, and they can have important impacts on weather from synoptic to intraseasonal scales. During CINDY2011/DYNAMO, tropospheric mixed Rossby-gravity waves transported moisture during the MJO which may have contributed to multiple MJO cycles (Chen et al. 2015). These equatorial waves in particular have an important meridional dispersive component moving poleward and can spawn cyclones away from the equator (Zhou and Wang 2007).

3.1.4 Kelvin waves

The existence of v=0, m=-1 waves within equatorial waveguide of the tropical atmosphere has been known and studied since their first discovery by Matsuno (1966), who pointed out their similarity to coastal Kelvin waves (Thomson 1880) and thus introduced their common name. Barotropic Kelvin waves, introduced previously in Chapter 1, are a special solution to Eqs. 1.1-1.3 when the meridional component of velocity v is assumed to be zero (Matsuno 1966; p. 397 in Holton 1992); they only propagate eastward and are equatorially-trapped with the velocity fluctuations in the zonal direction. Matsuno's pioneering analysis of barotropic wave modes was subsequently extended to baroclinic (Holton and Lindzen 1968) and convectively-coupled modes (Kiladis et al. 2009). Baroclinic modes were the first Kelvin waves actually discovered in the real (stratified) atmosphere (Wallace and Kousky 1968), and they have subsequently been found to be prevalent in the tropical lower stratosphere (Holton et al. 2001).

The baroclinic Kelvin wave solutions of the stratified atmosphere are found by considering wave motions in a non-hydrostatic environment as in Eq. 3.3. Eqs. 1.1 and 1.2 are combined with Eq. 3.3, v is assumed zero, and other variables take the forms

$$\begin{pmatrix} u \\ w \\ \phi \end{pmatrix} = e^{z/2H} \begin{pmatrix} \hat{u}(y) \\ \hat{w}(y) \\ \hat{\phi}(y) \end{pmatrix} e^{i(k_1 x + k_3 z - nt)}, \tag{3.4}$$

where H is a standard height scale. If the vertical wavelength is assumed to be small (< 15 km; Andrews et al. 1987), then the problem is reduced to a simplified set of three equations:

$$n\hat{u} = k_1 \hat{\phi}, \tag{3.5}$$

$$\beta y \hat{u} = -\frac{\partial \hat{\phi}}{\partial y}, \tag{3.6}$$

$$k_1 \hat{u} = n k_3^2 N^{-2} \hat{\phi}. \tag{3.7}$$

From Eqs. 3.5 and 3.7, the dispersion relationship for baroclinic Kelvin waves is

$$n = \pm N k_1 k_3^{-1}. \tag{3.8}$$

In the vertical direction, the group and phase velocities of the wave are

$$c_g^{(z)} = \mp N k_1 k_3^{-2}, \tag{3.9}$$

and

$$c_p^{(z)} = \pm N k_1 k_3^{-2} \tag{3.10}$$

respectively. Eqs. 3.9 and 3.10 show that, in the vertical plane, the energy and phase propagation are in opposite directions. If the energy source is from below, as is generally true in the middle atmosphere, the positive root of Eq. 3.9 and negative root of Eq. 3.10 are the relevant ones. Thus, middle-atmospheric baroclinic Kelvin waves are a mechanism for transport of energy upwards from the troposphere. Equatorial Kelvin waves are confined to the tropics, and, just like other equatorial waves (see Eq. 1.7), they have amplitudes that decay meridionally from the equator. The following first-order differential equation in meridional direction can be derived from Eqs. 3.5 and 3.6:

$$\frac{\partial \hat{\phi}}{\partial y} + \frac{\beta y}{C_o}\hat{\phi} = 0\,, \tag{3.11}$$

where C_o is the horizontal gravity wave velocity, n/k_1 or $(gH_o)^{1/2}$. Eq. 3.11 has the nontrivial solution

$$\hat{\phi}(y) = Ae^{-\beta y^2 / 2C_o}\,, \tag{3.12}$$

where A is a constant. This solution shows that the wave's amplitude decays on the length scale $(2C_o/\beta)^{1/2}$ with increased distance from the equator, which is also known as the equatorial Rossby radius of deformation.

Even though atmospheric Kelvin waves only exist near the equator (approximately ±15°), they are a major player in subtropical dynamics. Kelvin waves are prevalent and impactful in the proximity of the tropical tropopause (Suzuki and Shiotani 2008; Tsuda et al. 1994b; Holton et al. 2001; Fueglistaler et al. 2009), where they play a key role in stratosphere-troposphere exchange (STE). Field campaigns have revealed their roles in ozone transport to the upper troposphere (Fujiwara et al. 1998), stratospheric dehydration (Fujiwara et al. 2001), and cirrus formation in the upper troposphere (Immler et al. 2008). Such processes have important influence on the atmospheric photochemistry and Earth's radiation budget. Enhanced turbulence caused by shear instabilities and Kelvin wave breaking has also been associated with these waves in the tropopause layer, as revealed by Doppler radar (Yamamoto et al. 2003), radiosonde (Alappattu and Kunhikrishnan 2010), and reanalysis (Flannaghan and Fueglistaler 2011) data. Therefore Kelvin waves can be source of clear air turbulence, and these instabilities are likely a common mechanism for the stratosphere-troposphere transport of atmospheric minor constituents like ozone and water vapor (Fujiwara et al. 1998) by intense, irreversible mixing. In regard to momentum transport, upper-level (dry) Kelvin waves are known to transport momentum upward in general, which is said to impact stratospheric phenomena such as QBO (Holton and Lindzen 1972; Hamilton 1999; Yang et al. 2012). Eastward-propagating disturbances similar to dry Kelvin waves have been implicated in the initiation of energetic convection events (Sakaeda and Roundy 2015), where momentum exchange is possible.

Convectively-coupled Kelvin waves are prevalent in the lower atmosphere, below the generally drier upper levels of troposphere, tropopause, and stratosphere. These waves are moist (versus dry waves discussed above), and diabatic heating processes should be included in theories to correctly treat these waves, which leads to complications and observed discrepancies in these waves' behavior in comparison to their dry counterparts (Kiladis et al. 2009). Convectively-coupled equatorial Kelvin waves have been shown to play a prominent role in intraseasonal variability of the tropical troposphere, with linkages to key phenomena like the MJO and ENSO (Grise and Thompson 2012; Straub et al. 2006; Kikuchi et al. 2017). They have been observed within envelope of MJO (Moum et al. 2014; Dias et al. 2017), and, in the absence of MJO, they still have a significant impact on the variability of convection in the troposphere (Kiladis et al. 2009 and references therein), albeit at higher frequency and smaller spatial scales than MJO. These waves, have their energy source in upper-mid-tropospheric deep convection (Shimizu and Tsuda 1997) and sometimes have a corresponding component behaving as a dry Kelvin wave in middle atmosphere.

The dry, middle-atmospheric Kelvin waves generally receive energy input from the tropospheric convection beneath, which includes convectively-coupled wave activity. Linkages of these middle-atmospheric waves to over-shooting convection have been established (Randel and Wu 2005). Owing to their dependence on convection, upper-level Kelvin waves exhibit seasonal behavior with late boreal winter (February) and late boreal summer (July-August) being particularly active periods (Suzuki and Shiotani 2008; Fujiwara and Takahashi 2001), but they always contain a substantial portion of disturbance spectral energy of the tropics. While the influence of convection on upper-level waves is well-known, the inverse interaction – how dry Kelvin-like waves in upper troposphere and tropopause might initiate convection – has only recently been proposed (Sakaeda and Roundy 2015, 2016), and examples of this dynamical vertical coupling were observed during ASIRI-RAWI at Seychelles and are described below. In this chapter, equatorial Kelvin waves around tropical tropopause layer will be identified along with lower atmospheric conditions favorable for wave-convection interaction. The next chapter (Chapter 4) will analyze the impacts of this type of interaction on the troposphere all the way down to the land/ocean surface.

3.2 Identification of Kelvin Waves

The major intraseasonal oscillations during ASIRI-RAWI were evidenced by zonal wind and potential temperature anomalies from radiosondes (individual sounding profile with 6-week mean profile removed), profiles of which are plotted in Figure 3.2 for both Seychelles and Singapore. A dominant pattern existed at 15-20 km in all plots, suggesting planetary waves were propagating at around the tropopause level throughout the experimental period, especially in February (cf. Suzuki and Shiotani 2008). The ground-based wave period was estimated as 15-18 days and (zonal wind) amplitude as 10-15 m s^{-1}. Wave crests first arrived at Seychelles and then Singapore, indicative of eastward phase propagation. Their periodicity was close to that reported for Kelvin waves previously (Andrews et al. 1987; Wallace and Kousky 1968; Fujiwara et al. 2001), supporting the waves' classification as equatorial Kelvin waves. However, additional data were needed to confirm that they were indeed Kelvin waves considering the rather large distance (~5400 km) between observational sites.

The ERA-I data (ECMWF 2009) approximate the state of equatorial atmosphere before, during, and after the experimental period. Figure 3.3a gives the temporal evolution of zonal wind at the equator and 100 hPa pressure level, with only the eastern hemisphere shown for clarity. NCEP/NCAR Reanalysis I data (Kalnay et al. 1996) is plotted similarly in Figure 3.3b for comparison, confirming that both reanalysis datasets capture the largescale wave-like signatures consistently. The westerly anomalies at both sites were part of the same largescale wave patterns, which confirmed the planetary nature of these waves even though beyond 90°E smaller disturbances contaminated their signals somewhat (Fig. 3.3). The wave pattern was altered over and did not propagate far beyond the Maritime Continent, a region where convection can penetrate the tropopause (Sherwood 2000; Liu and Zipser 2005) and intraseasonal oscillations like MJO can be strongly modified (Peatman et al. 2014). Again, eastward phase propagation was evident from the positive slope on the diagram (see the dashed arrows in Fig. 3.3a). The horizontal phase velocity $c_p^{(x)}$ was estimated from this Reanalysis data to be 20 m s^{-1} so that horizontal wavelength $\lambda^{(x)}$ was calculated as ~28000 km, assuming a wave period of 16 days (used hereafter); thus at 100 hPa the first horizontal mode of baroclinic Kelvin waves was recognized.

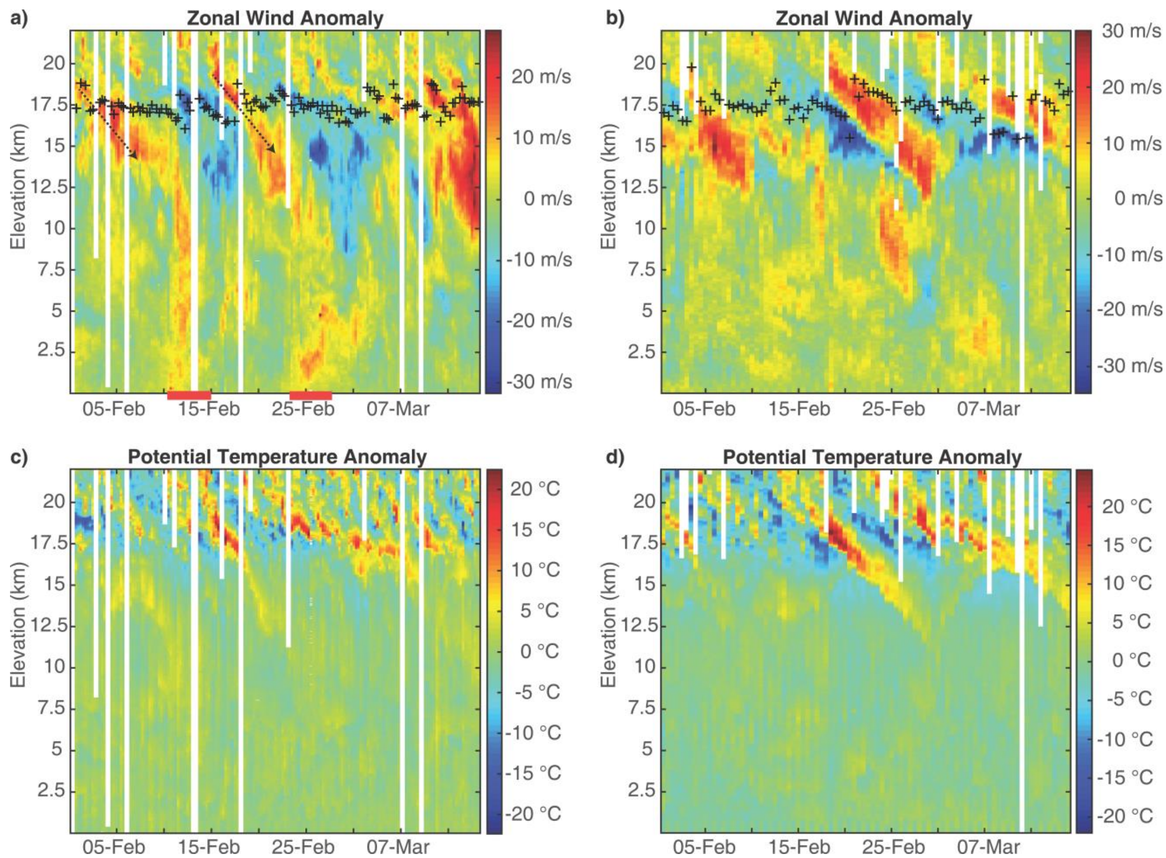

Figure 3.2: Time series of zonal wind and potential temperature anomalies taken from radiosonde profiles. Anomalies were calculated by subtracting 6-week mean profiles from individual sounding profiles. Gaps between soundings ≤12 hours have been filled via temporal interpolation; gaps in data >12 hours have been maintained and are marked in white. Panels include zonal wind anomalies at (a) Seychelles and (b) Singapore and potential temperature anomalies at (c) Seychelles and (d) Singapore. The dashed black arrows in (a) show approximate vertical phase propagation of Kelvin waves. The '+' marks in zonal wind plots indicate the altitude of cold-point tropopause, i.e., the minimum temperature from radiosonde profiles. Red bars on horizontal axis in (a) approximately denote periods of significant westerly zonal velocity in surface layer at Seychelles.

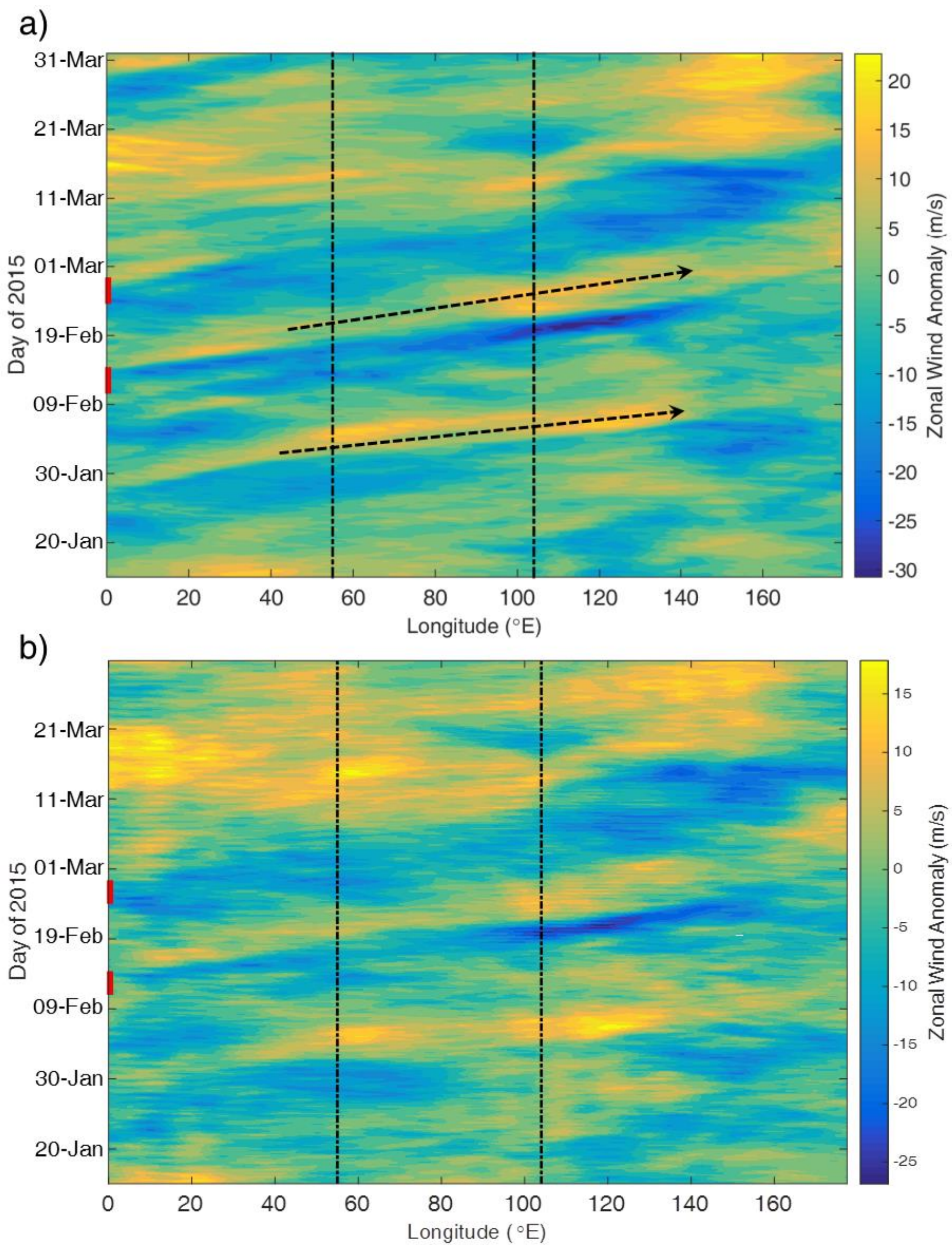

Figure 3.3**:** Hovmöller diagram of 100 hPa zonal wind anomalies along equator (averaged 5°N - 5°S) in eastern hemisphere from 15 January to 1 April, 2015 plotted from reanalysis datasets, including (a) ECMWF Re-Analysis-Interim (ERA-I) and (b) NCEP/NCAR Reanalysis 1 (Kalnay et al. 1996). Dashed arrows in (a) approximate the phase propagation. Red bars on the vertical (time) axes are the westerly wind burst (WWB) periods, the same periods as on horizontal axis of Figure 3.2a. Vertical dash-dot lines indicate longitudes of Seychelles and Singapore.

The waves must satisfy the dispersion relations for equatorial Kelvin waves to classify more firmly, and for full enumeration of dispersion relationship the intrinsic frequency rather than the Doppler-shifted (ground-based) frequency must be used. There was a background easterly wind speed of -6 to -8 m s^{-1} in upper levels (100-200 hPa), which, for simplicity, were assumed to be the steering altitude (Dias and Kiladis 2014). Therefore the phase velocity relative to the mean flow, $c_p^{(x)*}$, was estimated as 27 m s^{-1}; note that $c_p^{(x)*}$ is same as the gravity wave speed C_0 from Eqs. 3.11-3.12. In upper troposphere and stratosphere, equatorial Kelvin waves generally have upward group velocities but downward phase velocities (Andrews et al. 1987). The dispersion equation for vertical phase propagation (Eq. 3.10) can be rewritten using Eq. 3.8 and assuming downward propagation as

$$c_p^{(z)} = -\frac{k_1 \left(c_p^{(x)*}\right)^2}{N}, \tag{3.13}$$

where k_1 is the horizontal wave number and N the Brunt-Väisälä frequency (Fujiwara et al. 1998). Using Eq. 3.13, the vertical phase velocity $c_p^{(z)}$ could be calculated as -0.0074 m s^{-1}, or about -640 meters per day, where a Brunt-Väisälä frequency N^2 of 5×10^{-4} s^{-2} was used. This N^2 value was the average from Seychelles soundings in 16 to 19 km range, which is consistent with relevant past work (e.g., Ratnam et al. 2006). The calculated descent rate (640 m d^{-1}) approximately matched the negative slope registered by the descent of peak (westerly) phases in Figure 3.2a (see dashed arrows). The corresponding vertical wave length ($\lambda^{(z)}=2\pi/k_3$) was ~7.6 kilometers.

Other variables in reanalysis (and radiosonde) datasets confirmed the existence of the Kelvin waves in tropical tropopause layer. Time-longitude diagrams of meridional wind, potential temperature, and geopotential height anomalies at 100 hPa from ERA-I data are shown in Figure 3.4, similar to Figure 3.3a. Meridional wind (Fig. 3.4a) lacked notable disturbances on intraseasonal timescales consistent with the assumption v=0 for Kelvin waves, although smaller scale disturbances were evident. Conversely, geopotential height and potential temperature anomalies (Figs. 3.4b-c) displayed disturbances correlated with Kelvin waves. High geopotential anomalies traveled in phase with Kelvin wave zonal wind anomalies and temperature anomalies were roughly in quadrature (Kiladis et al. 2009), with peak temperature phase leading westerlies by ~2-3 days (see also Figs. 3.2c-d).

In summary, the following attributes supported the identification of the observed disturbances as baroclinic Kelvin waves: (i) eastward propagation, (ii) adherence to vertical phase dispersion equation (Eq. 3.10) for equatorial baroclinic Kelvin waves, (iii) no intraseasonal-scale meridional disturbance component (Fig. 3.4a), (iv) arrival of temperature peak phase (Figs. 3.2c-d; Fig. 3.4c) preceded the peak westerly phase by approximately a quarter cycle, (v) coincidence of peak westerly velocity with positive geopotential anomalies (Figs. 3.4b), and (vi) less pronounced anomalies over Sri Lanka station, indicating the equatorially-trapped amplitude of the waves.

Figure 3.4: Hovmöller (time-longitude) diagram of ERA-I variables at tropopause (100 hPa) averaged 5°S - 5°N in eastern hemisphere: (a) meridional wind anomaly, (b) geopotential height anomaly, (c) temperature anomaly. Red bars on vertical axes are WWB periods. Note geopotential height has been low-pass filtered to daily averages to filter effects related to atmospheric tides.

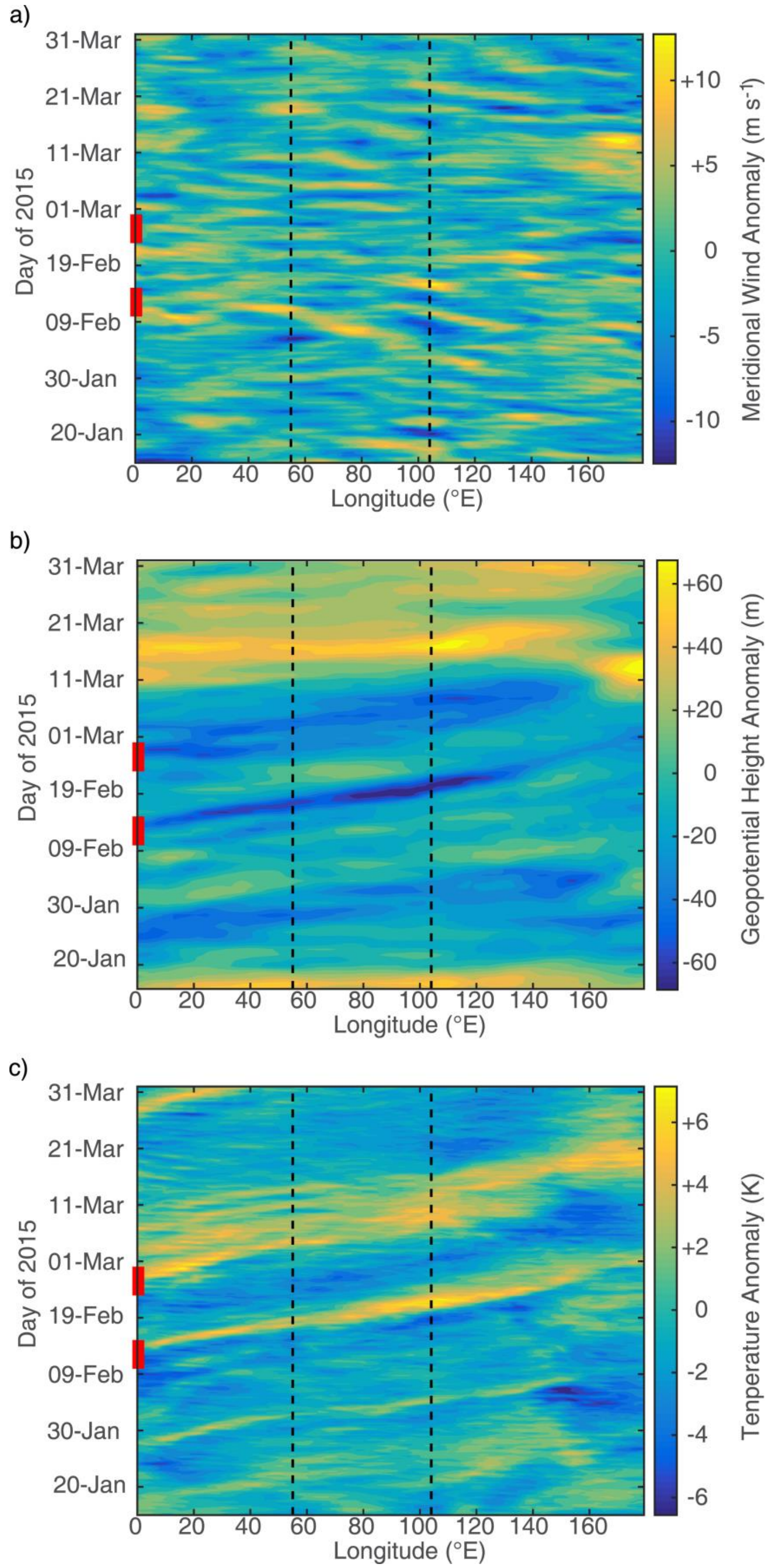

a)
31-Mar
21-Mar
11-Mar
01-Mar
19-Feb
09-Feb
30-Jan
20-Jan
Day of 2015
0 20 40 60 80 100 120 140 160
Longitude (°E)
+10
+5
0
-5
-10
Meridional Wind Anomaly (m s-1)
b)
Geopotential Height Anomaly (m)
+60
+40
+20
0
-20
-40
-60
c)
Tenperature Anomaly (K)
+6
+4
+2
0
-2
-4
-6

3.3 Tropopause Variation and Kelvin-Helmholtz Instabilities

The tropical tropopause layer (TTL), where Kelvin waves described in the previous section were documented, is an important transitional region between the convective, well-mixed tropical troposphere and the highly stratified stratosphere with their different respective chemical compositions. The TTL is typically centered around 17 km and spans from upper troposphere ~15 km to lower stratosphere ~18 km (Randel and Jensen 2013). Temporal variations in the TTL are most often tracked using the metric of cold-point tropopause temperature (CPT, i.e., the minimum temperature in the vertical profile of troposphere and stratosphere) and its altitude.

CPT variations during ASIRI-RAWI experiment are documented in Figure 3.2 by cross-marks. Some notable features were the sudden increases in altitude of CPT, which occurred simultaneously with the passage of peak westerly phase of Kelvin wave through TTL. In general equatorial wave activity is known to modulate CPT (Kim and Alexander 2013), and the observed modulations of temperature were related to the propagation of Kelvin waves through the TTL. Similar changes in CPT height on the order of ~2 km, which are termed here as 'tropopause jumps,' have been attributed to Kelvin waves and identified concurrently with internal shear instabilities (Fujiwara et al. 2003; Mega et al. 2010) and stratosphere-troposphere mixing events (Fujiwara et al. 2001; Fujiwara et al. 1998). The atmospheric conditions during the 'tropopause jump' at 1200 UTC on 18 February are shown in Figure 3.5 along with the profiles from the sounding at 0600 UTC on 16 February, which together characterized the evolution of the TTL during periods of the 'jumps.'

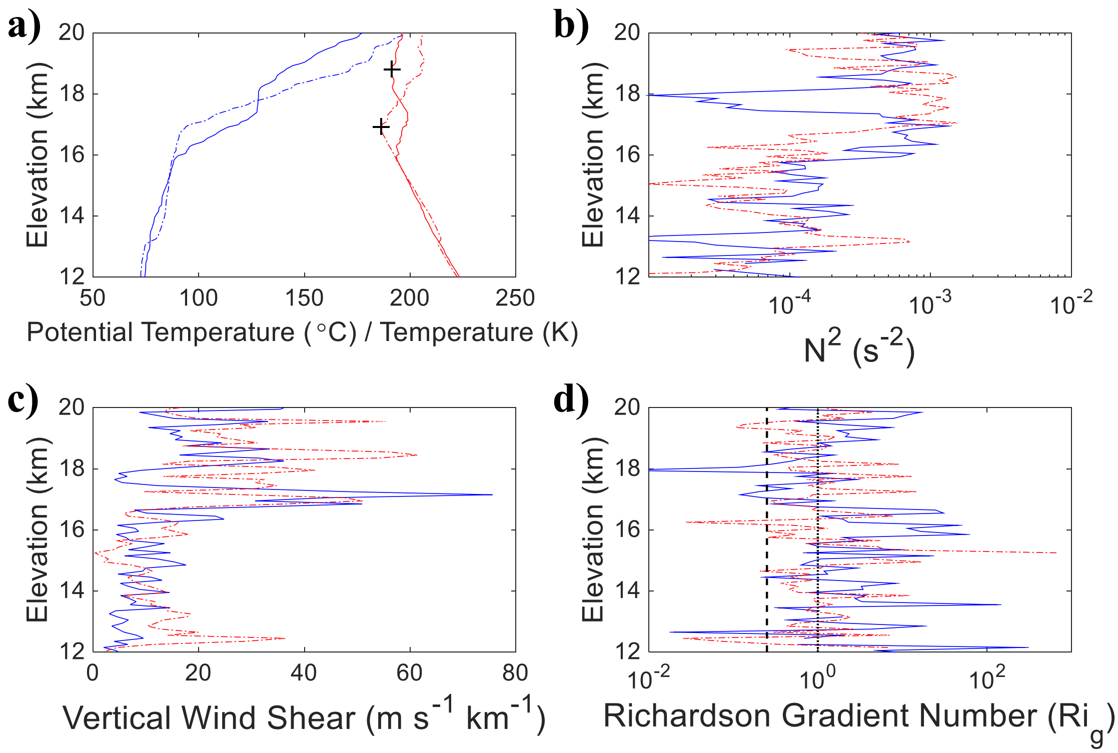

Figure 3.5: Segments of Seychelles radiosonde profiles from 12-20 km, including tropical tropopause layer. Results are bin-averaged to 100-m from 25-m resolution. (a) Potential temperature profiles displayed in blue for 16 February at 0600 UTC (dashed) and 18 February at 1200 UTC (solid). Temperature displayed similarly in red, for same radiosonde profiles. Black '+' marks show the elevation and temperature of cold-point tropopause. Note that potential temperature and temperature are plotted using different scales, °C and K, respectively. (b) Brunt-Väisälä frequency squared (N^2) from 16 February at 0600 UTC (red dashed) and 18 February at 1200 UTC (blue solid). The line designations here apply to subsequent panels. (c) Same as in (b) but for vertical wind shear, calculated using $S = \sqrt{(du/\ dz)^2 + (dv/\ dz)^2}$, where u and v are zonal and meridional components of velocity, respectively. (d) Same as in (b) but for gradient Richardson number ($Ri_g = N^2 / S^2$). Black vertical dashed/dotted lines are critical Ri_g values of 1.0 and 0.25.

On 16 February, a typical stratosphere-troposphere transition was observed in Figure 3.5a with a minimum temperature at ~17 km as well as steadily increasing temperatures above due to radiative heating and below due to adiabatic heating. The peak temperature phase of Kelvin wave preceded the peak westerly phase by approximately one quarter cycle so that it descended below ~17 km in the days following 16 February. The result was the rise of temperatures down to 16 km, partially due to adiabatic heating of air parcels via the wave motions. Minimum temperatures around altitude of former CPT between 16 and 18 km were eliminated, and the potential temperature gradient was significantly weakened, as observed by 18 February sounding (Fig. 3.5a). Potential temperature profiles had previously (16 February) displayed a clear transition between troposphere and stratosphere with a sharply increasing gradient above CPT, but by 18 February the potential temperature profile was nearly vertical in a 600-800 m region centered on 17.8 km and generally weakened elsewhere in the TTL. The weaker gradients are expected due to Kelvin wave's temperature perturbations, but the extended region of near-constant potential temperature suggests that irreversible changes (i.e. mixing not stirring) may have occurred during the event. The reader is referred to Figure 12 from Mega et al. (2010) for a helpful schematic of how a Kelvin wave alters the typical tropopause profiles of temperature and potential temperature as described above.

The perturbations to potential temperature lowered the Brunt-Väisälä frequency (N^2) in a region where stability was typically increasing with altitude (Fig. 3.5b), which would generally promote conditions favorable for instability. When combined with increased shear in TTL due to Kelvin wave passage (Fig. 3.5c), the Kelvin wave's perturbations to potential temperature gradient and a background of lower N^2, which naturally drops by nearly an order of magnitude below CPT (see 16 February in Figure 3.5b), caused the drop of Ri_g below critical values (Fig. 3.5d) and provided trigger for shear (Kelvin-Helmholtz, K-H) instabilities and turbulent mixing (Ivey et al. 2008). A further discussion on this aspect follows.

As the peak westerly phase of the wave descended, it encountered a tropical easterly jet at ~17 km (see background wind in Figure 3.6) resulting in large peaks in vertical shear (Fig. 3.5c) on 18 February. Ri_g (Fig. 3.5d) decreased below both non-linear and linear stability limits of 1.0 and 0.25, respectively, much more often than in the 16 February case because of the combination of low N^2 and high shear. Ri_g ~1 is favorable for efficient mixing and Ri_g ~0.25 for K-H billowing (Strang and Fernando 2001b). The latter may have been observed by our sounding on 18 February judging by the resemblance to profiles of K-H billows in the laboratory, ocean, and field observations described by De Silva et al. (1996) and TTL observations of Mega et al. (2010). The form of K-H billowing during sounding at 1200 UTC on 18 February was indicated by the structure of N^2 and vertical shear profiles (Figs. 3.5b-c) – peaks at the edges around 17.2 and 18.4 km with a region of relatively low N^2 and shear in between these peaks. This structure bears particular similarity to that seen in radiosonde profiles from 16 December 2008 presented in Mega et al. (2010). The Ri_g values above and below the K-H region remained relatively large, confining mixing to the K-H layer. Note that the limited vertical resolution (25 m) of radiosonde observations precluded accounting for lower Ri_g values that could have existed at smaller scales (De Silva et al. 1999; Werne and Fritts 1999).

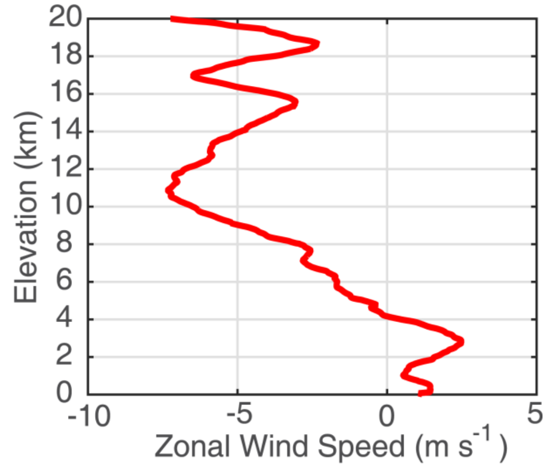

Figure 3.6: Mean zonal wind velocity profile from 6-week radiosonde campaign. Besides in lower troposphere, background flow was generally easterly. The second-highest velocity peak (<20 km) was centered around ~17 km in the tropical tropopause layer, which was possibly some weak manifestation of the tropical easterly jet or related to Walker circulation.

Other radiosonde profiles from 16-18 February at Seychelles and the earliest soundings of the experimental period (see another 'tropopause jump' at 0000 UTC on 2 February in Figure 3.2a) displayed similar features as have been noted for Figure 3.5. Our radiosonde observations bear strong similarity to those from past campaigns (Fujiwara et al. 2003; Yamamoto et al. 2003; Mega et al. 2010) with radars to measure turbulence enhancement during K-H instabilities associated with Kelvin waves. Their compiled evidence suggests that K-H instabilities, with similar characteristics as what we observed in some soundings, are transient and localized events of increased turbulence that persist intermittently during the passage of a certain phase of Kelvin waves through the TTL. Lack of direct observations of turbulence in our case prevented firm conclusions on K-H billowing and stratosphere-troposphere exchange. Whether or not the modulations caused instabilities converting some wave energy to turbulence, the radiosondes importantly showed the passage of Kelvin waves through the tropopause layer, accompanying modulations, and possible irreversible mixing.

3.4 Kelvin Waves in Upper Troposphere and Other Tropospheric Disturbances

Radiosonde data (Fig. 3.2) indicated that the Kelvin waves persisted above and below the tropopause as tilted (baroclinic) waves with downward phase velocities as discussed in Section 3.2 and illustrated by dashed arrows in Fig. 3.2a. After the peak westerly phases of Kelvin waves passed through the TTL, they followed the theoretically predicted descent rate (~640 meters per day) moving from ~17-18 km to ~12-13 kilometer within 7-9 days. The descent is evident in Figures 3.2a-d (marked in Figure 3.2a), though perhaps blurred by diffusion of momentum by local instabilities as described in previous section. Figure 3.7 provides an example of the Kelvin wave's westward-tilted vertical structure in the lower stratosphere, TTL, and upper troposphere on February 23 with in-phase velocity and geopotential perturbations. The in-phase relation of westerly wind and high geopotential (pressure) anomalies has already been noted based on Figures 3.3 and 3.4b. After the peak westerly and pressure phases arrived in the upper troposphere (~12-14 km), i.e., approximately 7-9 days after causing ‘tropopause jumps,’ a striking observation was made at Seychelles – anomalous westerly wind disturbances existed at surface simultaneously with upper-tropospheric anomalies from Kelvin waves. These periods of anomalous westerly momentum at surface are marked by red bars in Figure 3.2a and will be referred to as ‘westerly wind bursts’ (WWBs) hereafter.

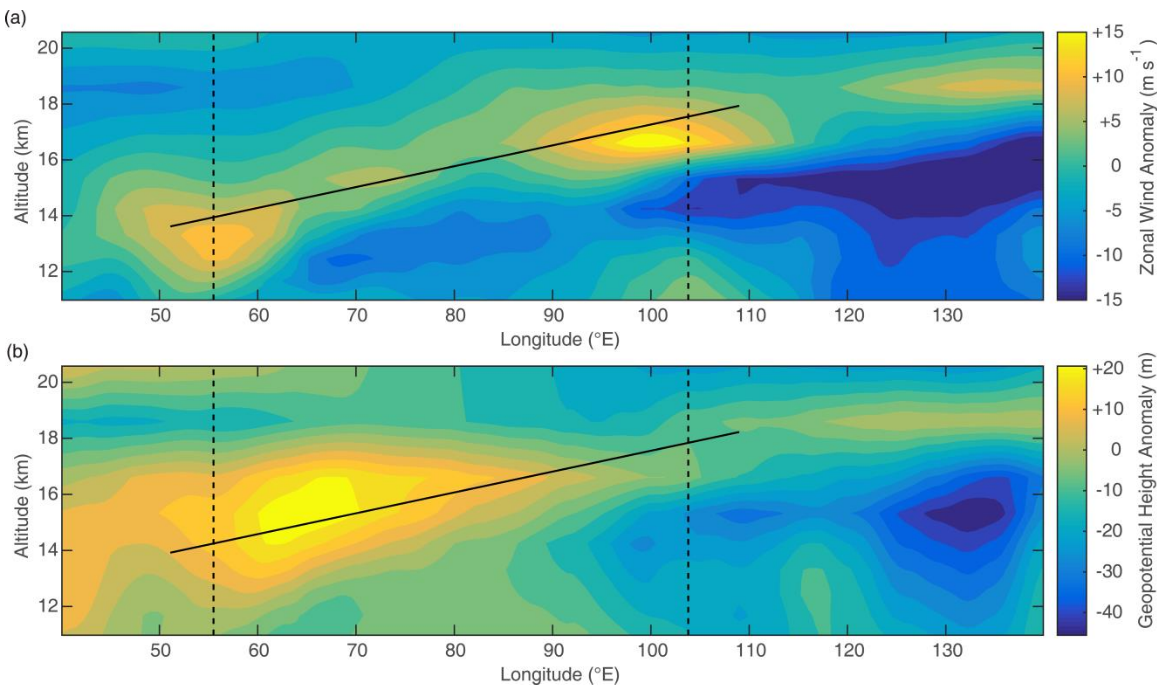

Figure 3.7: Vertical cross-sections of (a) zonal wind anomalies and (b) geopotential height anomalies in tropopause and upper troposphere on 23 February 2015 (daily average) before second WWB. Dataset used for this and all subsequent figures in Chapter 3 is ERA-I. Averaging is done over latitudes 0° - 5°S. The eastward-tilted vertical structure expected above the mid-troposphere for Kelvin waves was evident as well as coupled westerly wind and high pressure anomalies. Dotted lines are longitudes of Seychelles and Singapore. The solid line indicates the constant phase lines based on Figure 3.2.

Shortly after the appearance of surface westerlies, westerly wind anomalies were evident throughout the entire troposphere in a column (chimney). These westerly anomalies below 12 km cannot be explained as a phase descent of middle-atmospheric dry Kelvin waves, and further analysis was needed to understand the possible source of the westerly momentum in surface layer. Although measurements of momentum in troposphere were limited to three daily soundings and Lidar scans of the lower 1 km from a fixed point at Seychelles, reanalysis datasets were consulted for more evidence on the origins of the anomalous westerly momentum. Figure 3.8 displays Hovmöller diagrams of key variables at 250 hPa, just below the lowermost level in Figure 3.7 and still in upper troposphere. Note that Table A.1 is provided in Appendix for general use in pressure level (hPa) to altitude (m) conversions because both systems are used in the literature and to enable easy conversion to a reader's system of preference. Westerly anomalies appeared in the western IO during the WWBs (red bars on vertical axes), but the eastward propagation (i.e. positive slope on diagrams) associated with Kelvin wave anomalies (Fig. 3.3 and 3.4) was not evident. The shallow slope which was detectable on diagrams during WWB periods was instead indicative of westward propagation and suggested a shorter period at this level relative to Kelvin wave period. Note that not all variables consistently displayed correlated patterns across all longitudes of Western IO, and, in general, interpretations based on a single level should be treated with caution.

The mid-tropospheric anomalies shown in Figures 3.9 and 3.10 give a clearer picture of the westward-propagating anomalies that were faintly detectable from Figure 3.8. Wave-like disturbances were evident during February, particularly in region 60°-

90°E. For these disturbances, northerly meridional and westerly zonal anomalies appeared approximately in-phase, though the short period made exact phase relations (quadrature versus in-phase) difficult to distinguish. Additionally, low geopotential anomalies in Figure 3.10c were approximately aligned with the northerly/westerly phases, and therefore patterns were consistent with cyclonic (clockwise) circulation around low pressure centers expected in the southern hemisphere. Attempts at precise identification of individual smaller-scale, higher-frequency, and convectively-coupled waves using reanalysis datasets should be viewed with circumspection because of known challenges, such as inconsistencies between datasets for such short waves (Kim and Alexander 2013). Nonetheless, the estimated wavelength from diagrams was ~4000-5000 km and the westward phase speed was 5-7 m s^{-1}, from which a wave period of 7-10 days was calculated. In normalized wave number-frequency space (Fig. 3.1) these wave characteristics would place these disturbances near where dispersion curve for m=0 mode passes through k*=-1 suggesting that these were westward mixed Rossby-gravity waves. However, the (pressure-wind) phase relationships and vertical structure observed near Seychelles in the reanalysis data were not consistent with mixed Rossby-gravity wave but instead with westward inertio-gravity waves. This mismatch could suggest that the disturbance is a combination of different equatorial wave modes and not a specific standalone wave, which is known to be possible from other examples such as MJO envelope.

Figure 3.8: Hovmöller (time-longitude) diagram of ERA-I variables in upper troposphere (250 hPa) averaged ~2.5-7.5°S: (a) zonal wind anomaly, (b) meridional wind anomaly, and (c) geopotential height anomaly. Note that two features of this and subsequent diagrams have changed in comparison to those in Figures 3.3 and 3.4 so as to focus on a region of Indian Ocean centered meridionally near Seychelles' latitude and south of the equator, where there may be relatively more convectively-coupled wave activity due to proximity to seasonal Intra-Tropical Convergence Zone. Averaging is done over ~2.5-7.5°S, and the longitudinal range is 40-140°E. Dotted black lines are longitudes of Seychelles and Singapore. Red bars are periods of strong westerlies at surface (WWBs). Note that diurnal averaging was done on geopotential height in (c) like in Figure 3.4b and in all subsequent geopotential height plots.

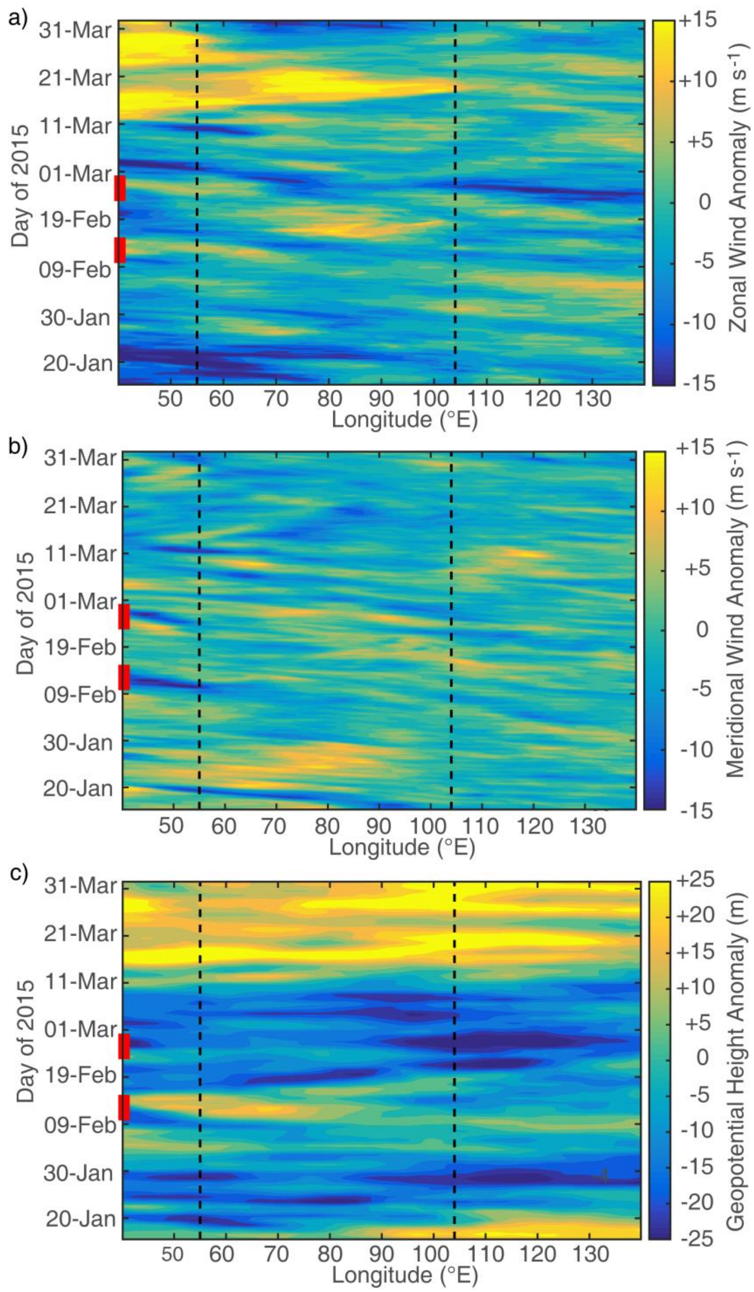
a)
31-Mar
21-Mar
11-Mar
01-Mar
19-Feb
09-Feb
30-Jan
20-Jan
Day of 2015
50
60
70
80
90
100
110
120
130
Longitude (°E)
+15
+10
+5
0
-5
-10
-15
Zonal Wind Anomaly (m s-1)
b)
Meridional Wind Anomaly (m s-1)
c)
+25
+20
+15
+10
+5
0
-5
-10
-15
-20
-25
Geopotential Height Anomaly (m)

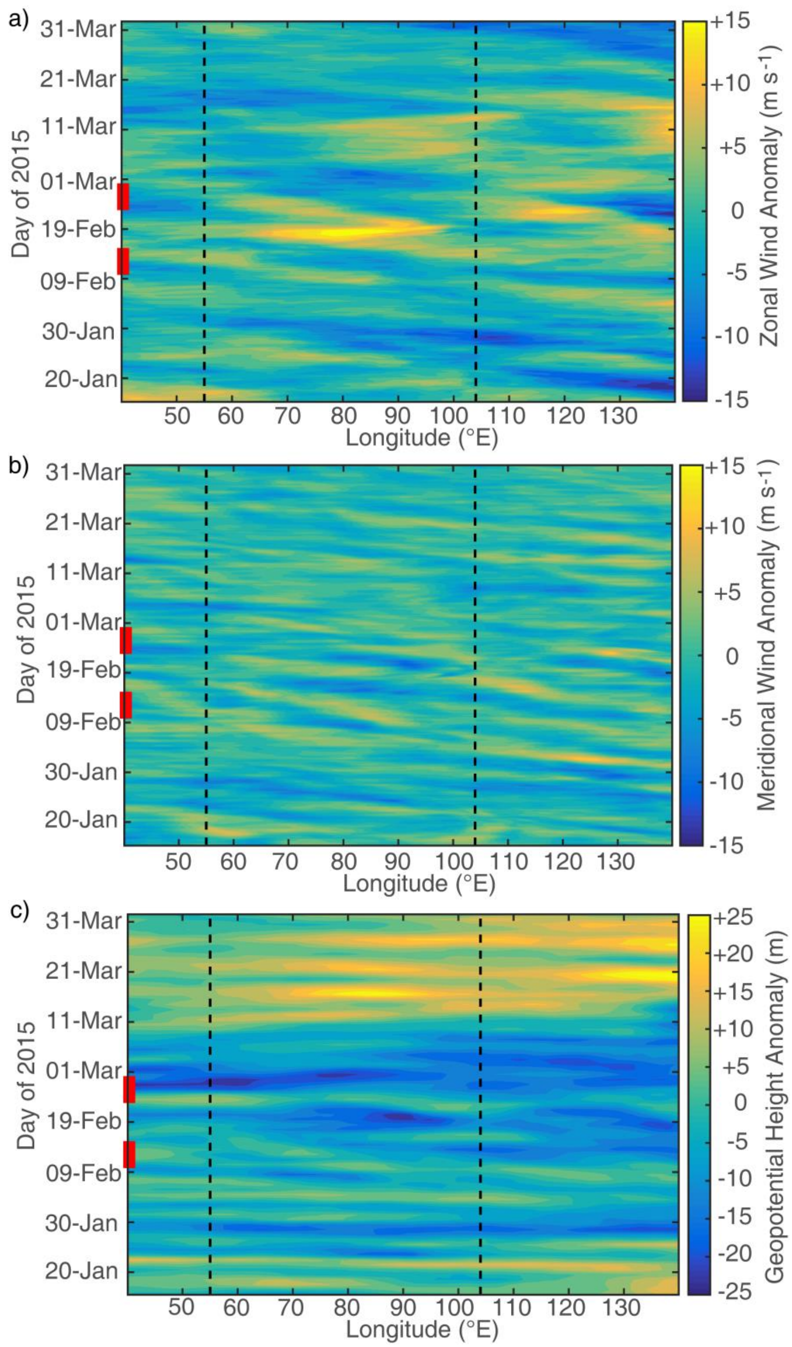

Figure 3.9: Hovmöller (time-longitude) diagram of ERA-I variables in mid-troposphere (450 hPa) averaged ~2.5-7.5°S: (a) zonal wind anomaly, (b) meridional wind anomaly, and (c) geopotential height anomaly. Dotted black lines are longitudes of Seychelles and Singapore. Red bars are periods of strong westerlies at surface (WWBs).

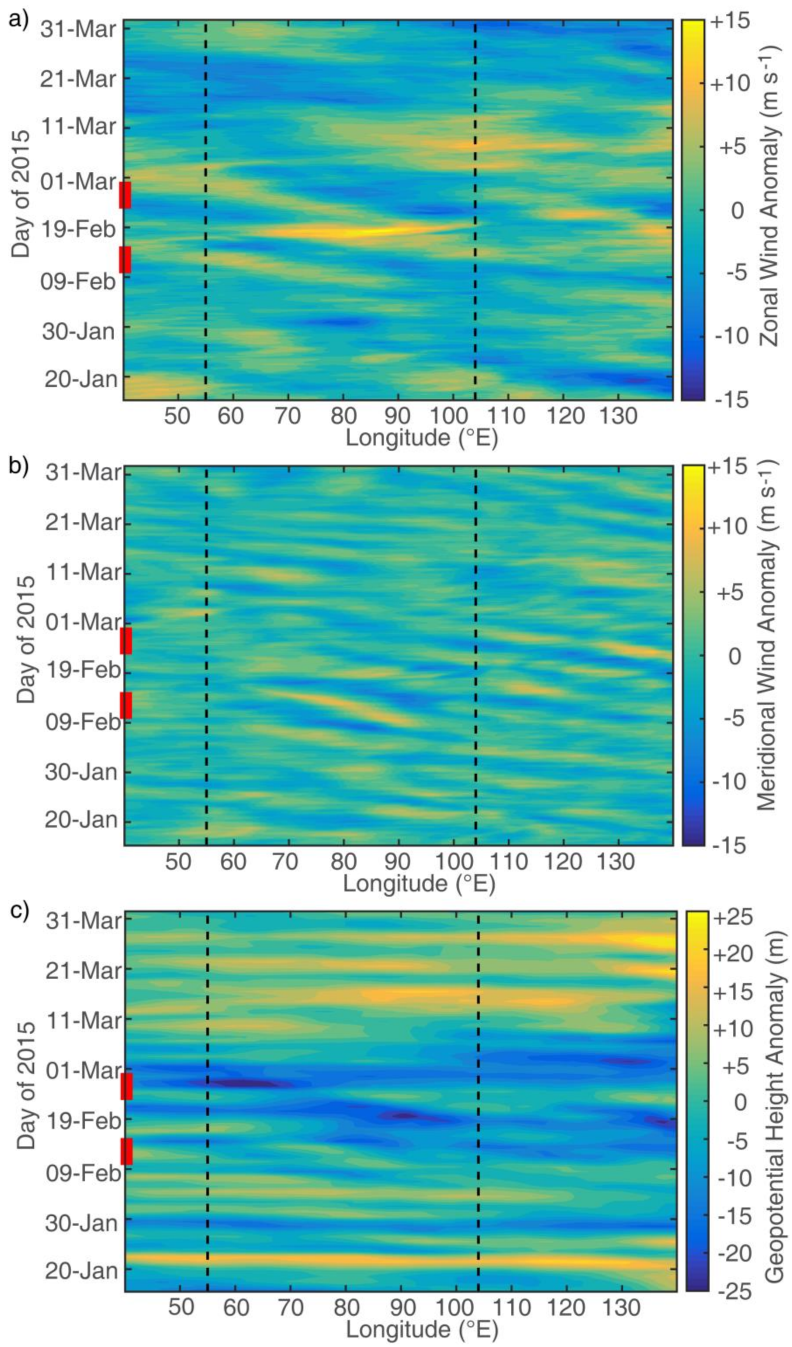

Figure 3.10: Hovmöller (time-longitude) diagram of ERA-I variables in lower-mid-troposphere (650 hPa) averaged 2.4-7.5°S: (a) zonal wind anomaly, (b) meridional wind anomaly, and (c) geopotential height anomaly. Dotted black lines are longitudes of Seychelles and Singapore. Red bars are periods of strong westerlies at surface (WWBs).

The exact classification of the tropospheric waves is rather tenuous when based on single reanalysis dataset. Figures 3.9-3.10 do most importantly show that wave-like disturbances propagated westward from central/eastern equatorial IO and were partly responsible for the anomalies observed in mid-troposphere over Seychelles during WWB periods. Tropospheric waves are convectively coupled in general so corresponding convection or precipitation indicators were expected to propagate with the mid-tropospheric wind and geopotential anomalies. Typical indicators of convective strength include infrared brightness temperature or OLR, which are remotely sensed by satellites (see Section 2.2.3). Figure 3.11 displays a Hovmöller diagram of infrared radiance observed by Meteosat-7 in IO, which can be directly related to infrared brightness temperature based on table from the European Organisation for the Exploitation of Meteorological Satellites (EUMETSAT 2016). The westward-propagating areas of low brightness temperature were evident, roughly correlated to the mid-tropospheric anomalies of westerly zonal wind. The lower radiance values correspond to deeper convection and propagated (westward) most noticeably from 65°E to 45-50°E for the first WWB (WWB1) and from 65°E to 55°E for the second WWB (WWB2). WWB2 featured convection that was weaker, less widespread, and less organized (i.e., direction of propagation is not clear) overall than in the case of WWB1. Another difference between the two WWB events was the possible emergence of an eastward-propagating envelope of convection that appeared to initiate around the time and location of the first WWB; the dashed line in Figure 3.11 indicates its approximated propagation. This eastward-propagating wave-like disturbance was made up of smaller-scale westward-propagating convective clusters and moved more slowly (10-12 m s^{-1}) than eastward-propagating dry Kelvin waves aloft (20 m s^{-1}). For the WWB2, no notable eastward propagation is evident on a large scale indicating weak convection, though there were perhaps instances of localized convection falling along a similar trajectory.

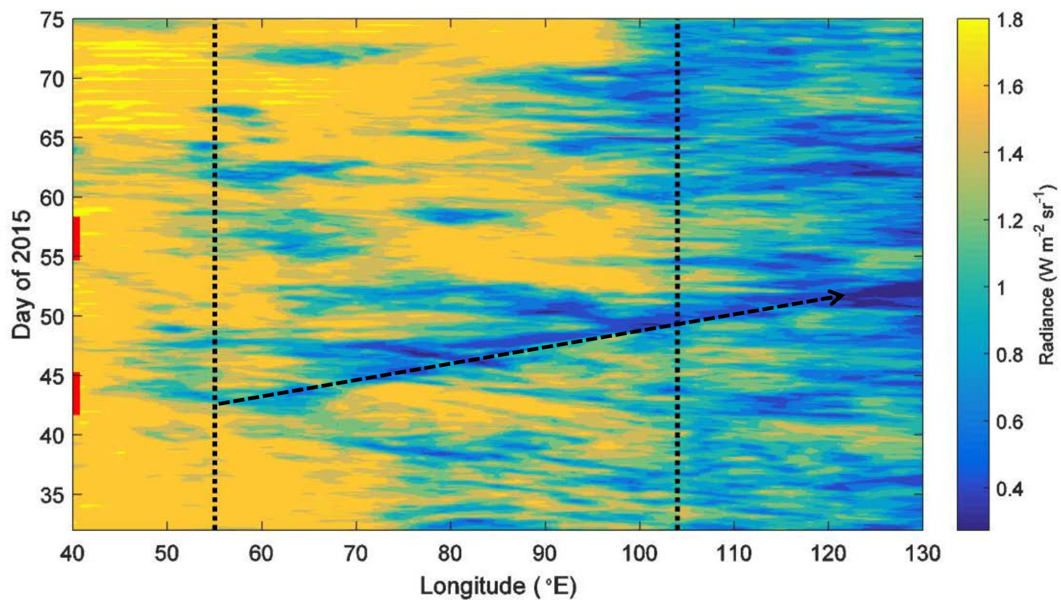

Figure 3.11: Hovmöller diagram of (infrared) radiance observed by Meteosat-7 for assessment of longitudinal propagation of infrared brightness temperature anomalies. Values have been averaged over latitudes ~2.5-7.5°S. The dashed arrow approximates the propagation of a convective envelope which moved eastward at ~10-12 m s^{-1} and possibly had origins associated with the first Kelvin wave and WWB. European Organisation for the Exploitation of Meteorological Satellites (EUMETSAT) was the source of and holds copyright on the original products used to create this diagram. Data products were accessed from Earth Observation Portal (http://archive.eumetsat.int/usc/) in October 2016.

Finally in Figure 3.12 the Hovmöller diagrams depicting the lower-tropospheric (~2 km) disturbances are shown. These diagrams are useful for delineating how the WWBs that appear at surface are related to the mid-tropospheric disturbances noted in Figures 3.9 to 3.11. For zonal and geopotential anomalies the disturbances look similar to those in Figure 3.10, except that the westerly anomalies appeared more intense in the region immediately surrounding Seychelles during the WWB periods. It is difficult to determine the respective arrival times of westerly anomalies based on comparisons of Figures 3.10 and 3.12, but Figure 3.13 shows more clearly that these waves had a eastward-tilted vertical structure in lower-mid troposphere as is common for certain convectively-coupled wave types like westward inertio-gravity waves. The data for Figure 3.13 were averaged over 2-day period so they do not represent the more significant tilts observed in individual profiles (not pictured). Owing to this tilted structure, the westerly wind anomalies from the wave-like tropospheric disturbances arrived first at the surface and subsequently at mid-levels of troposphere. This timing was also slightly perceptible from radiosonde data at Seychelles (Fig. 3.2a) around WWB periods. The eastward tilt in the lower troposphere coupled with westward propagation suggested that convectively-coupled westward inertio-gravity waves were a possible candidate for these disturbances. It should be noted that prominent surface meridional anomalies did not accompany the in-phase zonal and geopotential anomalies, which continued propagating westward from Seychelles during and immediately after the WWBs.

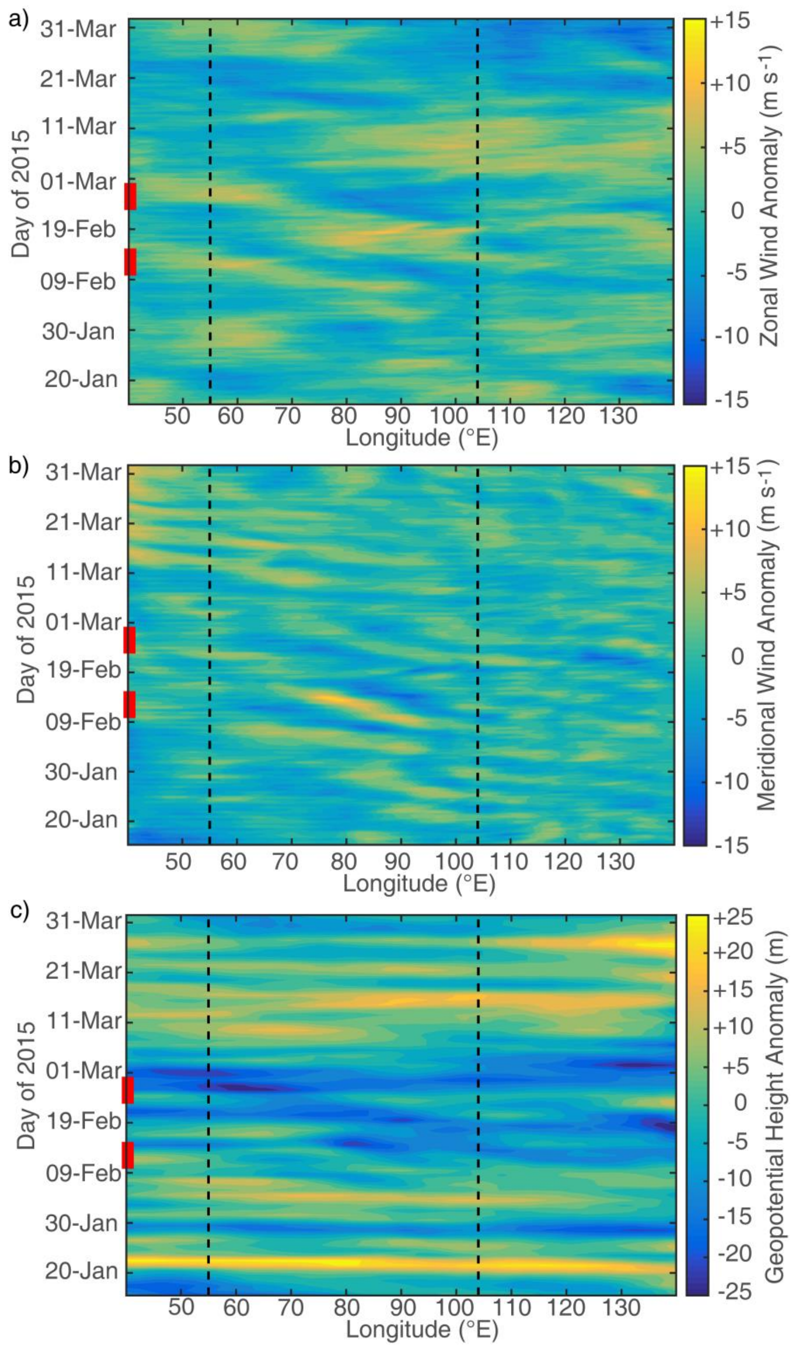

Figure 3.12: Hovmöller (time-longitude) diagram of ERA-I variables in lower troposphere (850 hPa) averaged ~2.5-7.5°S: (a) zonal wind anomaly, (b) meridional wind anomaly, and (c) geopotential height anomaly. Dotted black lines are longitudes of Seychelles and Singapore. Red bars are periods of strong westerlies at surface (WWBs).

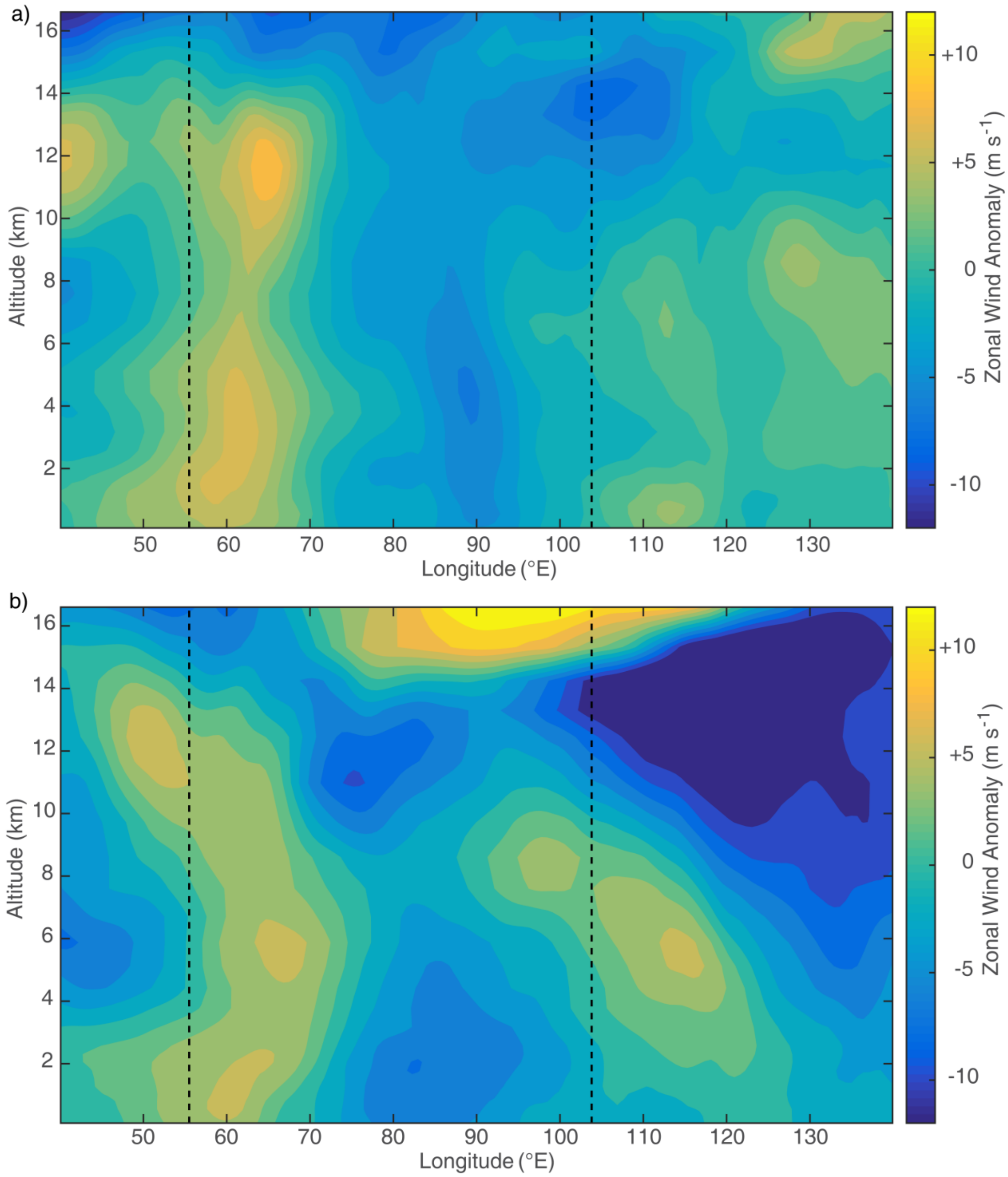

Figure 3.13: Vertical cross-sections of zonal wind anomalies in troposphere, averaged over first two days of identified WWBs: (a) 11-12 February and (b) 24-25 February. Results were averaged over same latitudes as in Figures 3.8-3.12 (~2.5-7.5°S) with black dotted lines indicating locations of Seychelles and Singapore. The westward tilt is obvious even after 2-day averaging if dotted black line for Seychelles is used as a (zero-tilt) reference. For individual cross-sections, the tilt was more pronounced.

3.5 Wave Interactions and Westerly Wind Bursts

The dry Kelvin wave phase in upper troposphere and westward-propagating convectively-coupled disturbances coexisted within a vertical column of troposphere in western Indian Ocean during the WWB periods, as identified in the previous sections. This coexistence could have been coincidental with no initial interactions between the upper- and lower-level waves, but in this section we argue that this would not be a satisfactory explanation of the dynamic events surrounding the WWBs in Seychelles. Recently, eastward-propagating Kelvin wave-like disturbances in upper troposphere have been linked to MJO-onset (Powell and Houze 2015; Sakaeda and Roundy 2015, 2016) so there is a precedent for upper-level anomalies influencing development of convection below.

As Figure 3.7 shows, downward-propagating high geopotential anomalies existed in the upper troposphere just prior to the appearance of deep convection signals in the west-central Indian Ocean during WWB2 (Fig. 3.11); high geopotential anomalies in upper-troposphere were also described by Sakaeda and Roundy (2016). Simultaneously, the low geopotential phase of a westward-propagating disturbance moved towards Seychelles region as shown in Figure 3.12 at lower levels. Another view of this disturbance is given in the panels of Figure 3.14, from which it is clear that the disturbance resembled a tropical depression propagating both westward and southward in the days prior to WWB2 (19-23 February). This disturbance brought the relatively low surface pressures to the equatorial region near Seychelles and even had an attached tropical cyclone forming to the south (15-20°S). Therefore the vertical pressure gradient over entire troposphere reached a maximum value, only to be surpassed during WWB1 when a similar pattern propagated in from the eastern IO (Figs. 3.9-3.12). Figure 3.15 depicts the steepening of the pressure gradient before both WWB events by showing the difference in geopotential height between top (175-200 hPa) and bottom (975-1000 hPa) of troposphere less the background (average) geopotential height difference during 6-week experimental period. This metric was an indicator of whether lower and upper tropospheric pressure anomalies were in tune (i.e. a tracer of pressure gradient anomaly), and we hypothesize that larger values of this metric are favorable for vertical pressure gradient coupling and the initiation of possible vertical exchange mechanisms.

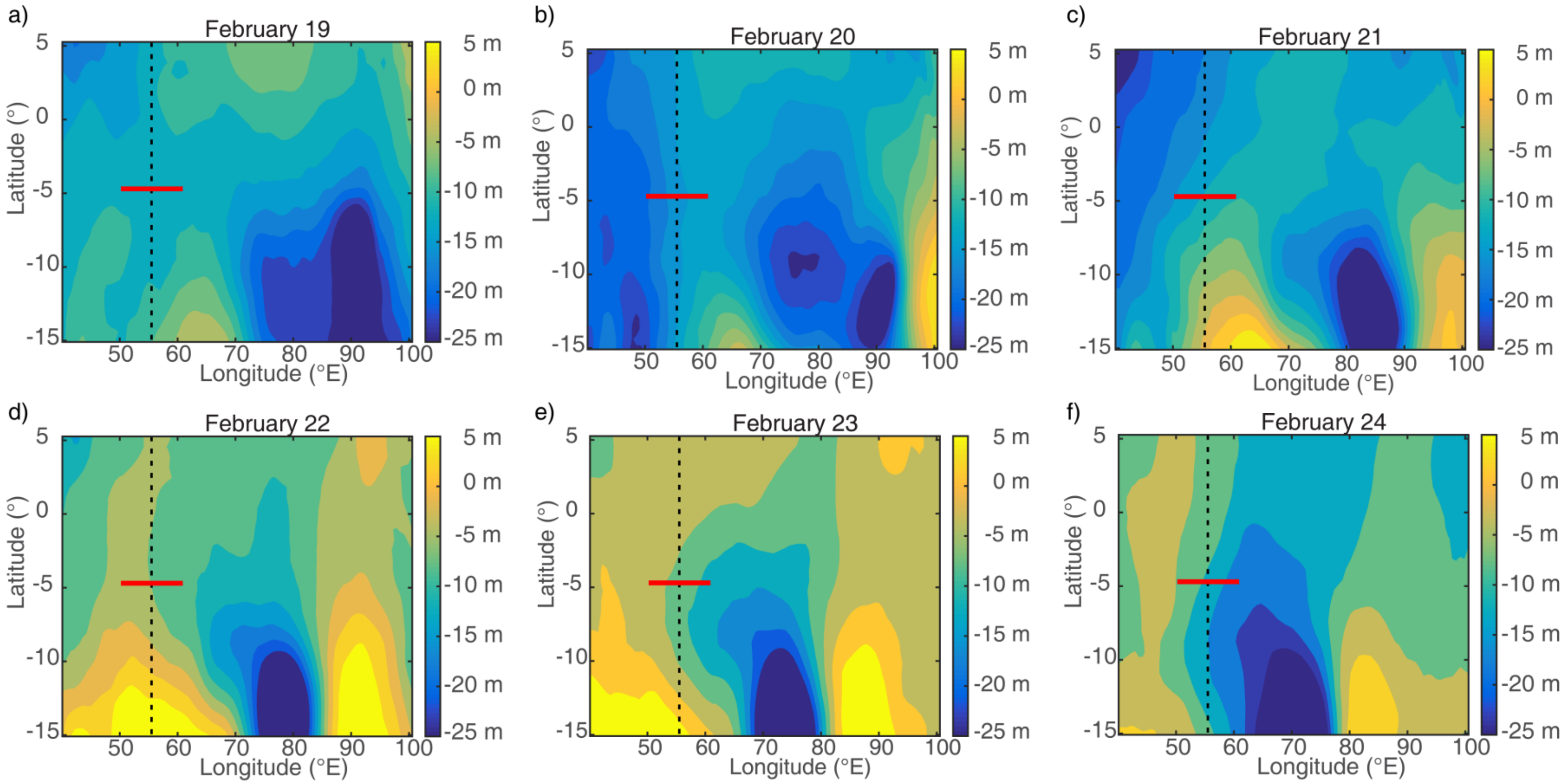

Figure 3.14: Horizontal cross-sections of daily-averaged surface (900-1000 hPa) geopotential height anomalies from ERA-I data for (a) 19 Feb, (b) 20 Feb, (c) 21 Feb, (d) 22 Feb, (e) 23 Feb, and (f) 24 Feb, the first day of the second WWB. Intersections of red lines and black dotted lines give the approximate location of Seychelles. Meridional and zonal wind anomalies were approximately coupled to this disturbance

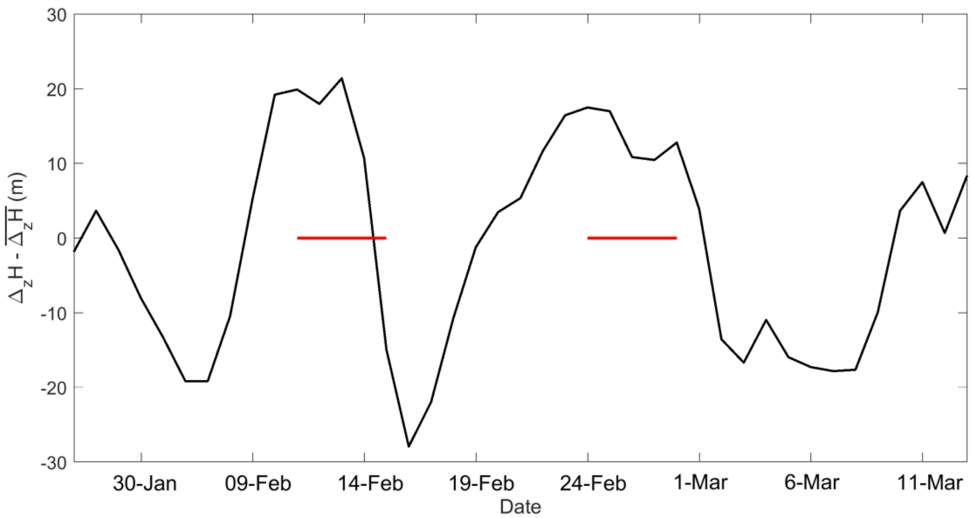

Figure 3.15: Daily vertical geopotential height difference (200 hPa versus 1000 hPa) minus background geopotential height difference, a type of pressure gradient anomaly, calculated from ERA-I data. Red lines are WWB periods and are plotted at the zero geopotential height difference level.

The simplified vertical momentum budget equation provided a framework for (crudely) analyzing the impacts of such anomalously large pressure gradients on vertical exchanges in the atmosphere. Assuming steady and horizontally homogeneous flow, the vertical momentum budget equation is

$$\bar{w}\frac{\partial \bar{w}}{\partial z} \approx -\frac{1}{\rho}\frac{\partial \bar{p}}{\partial z} + \bar{b} - \frac{\partial \overline{u_i' w'}}{\partial x_i}, \tag{3.14}$$

(Ⅰ) (Ⅱ) (Ⅲ) (Ⅳ)

where symbols have their usual meaning. The pressure gradient term (Ⅱ) was most obviously affected by the vertically co-aligning high and low pressure anomalies of the upper and lower tropospheric waves. It was estimated as it appears in Eq. 3.14 based on direct calculation from ERA-I data to have values of -1.3×10^{-2} and -1.1×10^{-2} m s^{-2} for

WWB1 and WWB2, respectively. The other three terms should approximately balance this enhancement to pressure gradient term from the co-aligning geopotential anomalies. The vertical advection term (Ⅰ) was scaled as $\bar{w} \cdot \partial \bar{w}/\partial z \sim W^2/h$, where W is the mean vertical velocity and h is a characteristic vertical length scale for troposphere. Data from reanalysis or Lidar observations in boundary layer can provide some vertical velocity estimates for W (see Chapter 4). The range of values found was from 1-2 cm s^{-1} in reanalysis to 0.5-1 m s^{-1} based on Lidar measurements at ~0.5-1 km. If the length scale is taken as 10 km, the term (Ⅰ) was from 10^{-8} to 10^{-4} m s^{-2}. The other terms were not available from standard model reanalysis so averaged measurements from flux tower in Seychelles were substituted. The buoyancy term (Ⅲ) was approximated based on measured buoyancy flux, $g\alpha\overline{w'T'}$, and the friction velocity, u^*, as $\bar{b} \approx g\alpha\overline{w'T'}/u^*$, where g is the gravitational acceleration (~10 m s^{-2}), α is the coefficient of thermal expansion (300^{-1} K^{-1}), u^* is the friction velocity, and $\overline{w'T'}$ is the kinematic temperature flux. The flux tower measured $\overline{w'T'}$ ~ 4-5×10^{-3} m K s^{-1} during WWBs. $\overline{w'u'}$ from tower was about -0.1 m^2 s^{-2} so that the friction velocity was estimated as $\sqrt{2 \times 0.1} \approx 0.5$ m s^{-1}, and hence the term (Ⅲ) is about -3×10^{-4} m s^{-2}. The final term, the Reynolds stress gradient term (Ⅳ), was estimated using $\partial\overline{u_i'w'}/\partial x_i \sim 3(\overline{w'\,u'}/l)$, where the integral length scale l was reckoned as 50 meters based on time series from 10-m sonic anemometer. Thus the term (Ⅳ) was ~ 6×10^{-3} m s^{-2}, about half the magnitude of the pressure gradient term (Ⅱ) but at least an order of magnitude higher than the terms (Ⅰ) or (Ⅲ).

Overall, the momentum budget equation (Eq. 3.14) suggests what transport mechanisms may dominate during the convectively-coupled wave phase observed during WWBs. While this is a simplified approach and may be mainly applicable within the ABL, it certainly highlights that turbulent eddy motions may play a critical role in the development of these convectively-coupled waves and their vertical transport of horizontal momentum. Horizontal momentum transported by this term (Ⅳ) in Eq. 3.14 would appear as a source term in horizontal momentum equation near surface (Tulich and Mapes 2008) and could possibly explain the appearance of much stronger westerly anomalies at the surface during this vertical pressure-gradient dominated phase of the passing wave-like disturbances. Further investigations using large eddy simulations including vertical shear effects are being performed by Dr. Eric Skyllingstad (Oregon State University) as an ONR-funded collaborative effort to delineate transport processes during the development of this type of convective disturbance.

Potential impacts of WWBs in the surface layer will depend on their horizontal length scales, for which we have included estimates below; Figure 3.13 and above discussions give an idea of the vertical length and time scales. The high geopotential phase of Kelvin wave may affect a horizontal area given by the zonal fluid parcel displacement scale and the Rossby equatorial deformation radius. The former would govern the longitudinal scale of WWB impacts and was estimated to be 300 to 650 kilometers based on zonal wind anomaly of 12 m s^{-1} and ground-based wave frequency. We have assumed in this estimation that the interaction with lower troposphere occurred over one-eighth to one-fourth of Kelvin wave cycle (high geopotential phase) so only the corresponding fraction of zonal displacement scale would be relevant. In latitudinal direction, the Kelvin wave's influence was confined by the Rossby equatorial deformation radius, which follows from Eq. 3.12 and was calculated to be ~1100 km. The horizontal cross-sections during first two days of each WWB are shown in Figure 3.16, and the peak westerly anomalies near Seychelles exhibited scales close to the estimates. The longitudinal scales evident in Figure 3.16 seem larger because the two-day averaging of disturbances which were not stationary during the WWB periods but propagating longitudinally. Smaller longitudinal scales, which were closer to estimates, were evident in the instantaneous cross-sections (not pictured). The strong westerly anomalies southeast of Seychelles, especially notable for second WWB, were possibly modulated by the same westward-propagating disturbances. They were not directly linked, however, to the peak positive anomalies observed near Seychelles since they were separated by more than 1000 km in the case of WWB2, so by more than the equatorial Rossby deformation radius. Overall, the horizontal length scale estimates based on Kelvin wave were in reasonable agreement with the extent of westerly anomalies at surface that appeared in reanalysis. Additionally the length scale estimates demonstrated that these events affected a large portion of the ocean surface, on the scale of one-half million square kilometers.

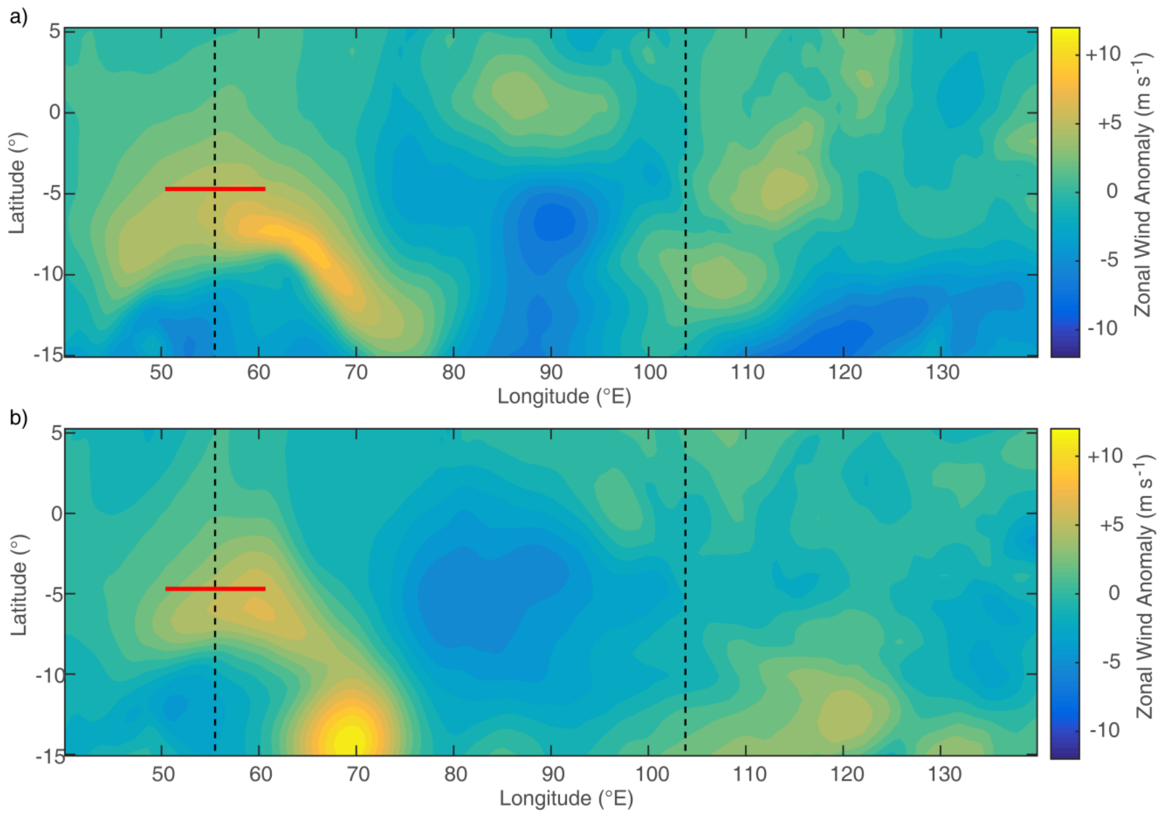

Figure 3.16: Horizontal cross-sections of zonal wind anomalies at surface (< 1 km), averaged over first two days of identified WWBs: (a) 11-12 February and (b) 24-25 February. The intersection of red line and black dotted line gives approximate location of Seychelles, and the length of the red line is equivalent to a horizontal (zonal) distance of ~1100 km. The vertical axis length (15°S-5°N) covers a meridional distance of ~2200 km.

The largescale spatial and temporal features of these westerly wind bursts at the surface demonstrated a degree of coherence with Kelvin waves aloft, which was overall suggestive that the simultaneous disturbances were related and not coincidental. Most notably from Figure 3.11, the westward-propagating convection that passed over Seychelles during WWBs was mainly strong and organized during the 4-day period, identified as roughly a quarter cycle of Kelvin wave phase in upper troposphere. Even though traces of the convection existed before the WWB2 to the east, the signals were not continuous with the line of convection manifest near Seychelles (Fig. 3.11). After the WWB period, the tropospheric disturbance changed significantly with no accompanying convective signal and the appearance of upper-tropospheric meridional anomalies (Figure 3.8b). Overall, the evidence supported the hypothesis that the high geopotential phase of Kelvin waves resonated with lower tropospheric low pressure centers to intensify or trigger the convective events near Seychelles that were accompanied by intensified westerly momentum anomalies in the boundary layer.

3.6 Summary and Conclusions

Observations taken during the ASIRI-RAWI campaign demonstrated the dominating presence of Kelvin waves in the tropical tropopause layer, which was more notable than any other equatorial wave activity during the observational period (1 February to 15 March). The Kelvin waves were carefully identified (Section 3.2), and localized Kelvin wave breaking due to shear (K-H) instabilities was presented (Section 3.3). These instabilities might cause some irreversible mixing, but in general the waves persisted in upper troposphere down to ~12-14 km throughout the month of February in western IO. Eastward-propagating tropospheric zonal wind anomalies and convection, i.e., convectively-coupled Kelvin waves, did not accompany the upper-level dry Kelvin wave, which are both well-known phenomena (Kiladis et al. 2009). Instead at lower levels disturbances moved into the western IO from the east; they resembled tropical depressions (low pressure centers), which are known from the literature to sometimes originate from equatorial Rossby or mixed Rossby-gravity waves (Molinari et al. 2007; Zhou and Wang 2007). While these disturbances could not be identified as a particular kind of shallow equatorial planetary wave (Matsuno 1966), they importantly brought relatively low geopotential air to lower troposphere of western IO, which coupled with high geopotential of Kelvin phase aloft to form a strong vertical pressure gradient anomaly. These localized, anomalous conditions, which occurred with the same quasi-biweekly period as the Kelvin wave aloft, were favorable for the initiation of vertical exchange processes.

The two events captured during ASIRI-RAWI field campaign in February were notable for the strong westerly wind bursts that accompanied convection and potential vertical exchange. The exact nature of the convective patterns at the surface was not identified, but the vertical structure from reanalysis with eastward vertical tilt may suggest westward inertio-gravity waves as a possible candidate. The actual surface measurements taken at Seychelles are utilized in Chapter 4 to examine the impact of the described largescale disturbances on physical processes in ABL. The analysis presented in this chapter is based on the commonly used reanalysis and satellite datasets over a relatively short ~2 month time period, but a longer period focusing on only Seychelles region and boreal winter months from 2009-2016 was checked preliminarily to see how widespread these phenomena were. These investigations uncovered one event exhibiting patterns very similar to those described for the two WWB events above (Figs. 3.3, 3.4, 3.12, 3.15, 3.16, etc.); it occurred around the winter solstice in 2009 (21 December). While this suggests that these coupled disturbances may be relatively rare events, the search was certainly not exhaustive enough to rule out more occurrences. Hopefully the largescale patterns have been presented with enough detail here to allow an investigation of the climatological significance of these events in future studies.

CHAPTER 4:

IMPACTS OF LARGESCALE OSCILLATIONS ON ATMOSPHERIC BOUNDARY LAYER AND OCEANIC MIXED LAYER

Largescale oscillations were described in Chapter 3 as they traversed the Indian Ocean while moving vertically through stratospheric and tropospheric layers. In this chapter, these wave-like patterns' impacts on the lower atmospheric boundary layer and the ocean's surface mixed layer are investigated. The disturbances were previously identified as westerly wind bursts (WWBs), which appropriately describes their main feature, though it will be shown that the events had more implications than high wind speed at surface.

4.1 Literature Review

Equatorial planetary waves and related intraseasonal oscillations have gained significant attention in the literature on tropical meteorology and climate as highlighted in last chapter. Present in both the atmosphere and ocean, the interactions between oceanic and atmospheric oscillations can influence the global ocean-atmosphere climate system in far-reaching ways, e.g., phase transitions in El Niño cycle (Seo and Xue 2005). Therefore detailed measurements in the surface (mixed) layers of atmosphere and ocean where the air-sea interactions take place are of great importance. Nonetheless, a vast majority of the research on intraseasonal scale processes, as reviewed in previous chapter, has utilized model reanalysis and satellite products but not in-situ observations of smaller-scale, embedded processes. Radiosonde observations, as in Figure 3.2, have been another useful resource for identifying impactful intraseasonal disturbances like MJO (Madden and Julian 1972). In the past 2-3 decades intensive, in-situ measurements for improving (or checking) the flux parameterizations in coupled ocean-atmosphere models have, by necessity, become a major area of research, aided by technological developments (Fairall et al. 2010), and therefore it has become opportune time to investigate how planetary waves produce an array of smaller-scale processes and influence air-sea exchanges.

Early experiments on the air-sea fluxes focused on the development of bulk parameterizations based on standard meteorological variables like wind speed and air temperature (e.g., Large and Pond 1981). Advancements in the study of equatorial oceans were incremental because the observational systems were quite complicated to deploy, often relying on ocean research vessels. It was not until the 1980s that larger observational datasets were collected in the equatorial oceans starting with the Tropic Heat I and II experiments which allowed for basic studies of how tropical ocean boundary layer responded to atmospheric forcing at different scales (Moum et al. 1989). The TOGA COARE field campaign allowed for great advancements in the field of ocean-atmosphere coupling (Webster and Lukas 1992). The dataset was used for the development and testing of most widely-used bulk parameterization schemes for air-sea fluxes (Fairall et al. 1996), and it became the first to capture in detail the oceanic side of the MJO (Shinoda and Hendon 1998 and references therein).

The intensive atmospheric boundary layer measurements during TOGA COARE revealed the limitations of GCMs (including ECMWF reanalysis) for accurate surface flux forecasts/hindcasts, particularly "during short-lived deep convective events," which encompass most of the intraseasonal convectively-coupled wave activity in the tropics (Weller and Anderson 1996). This finding would justify subsequent field experiments like CINDY2011/DYNAMO, which helped better establish the range of impacts that MJO and embedded convectively-coupled Kelvin waves can have on oceanic mixed layer (Moum et al. 2016, 2014). While the focus has been on the air-sea coupling associated with larger disturbances like MJO, impacts of short-period westward-inertio gravity waves on ocean SST were studied by Takayabu et al. (1996) in the context of TOGA COARE.

Field campaigns at the scales of TOGA COARE and DYNAMO are rare because of the massive commitments of resources and personnel required. Additionally, ocean observations, even during intensive observational periods, can only capture glimpses of the dynamics below the sea surface. Therefore modeling tools have been developed to better understand the ocean's response to atmospheric variability on synoptic to seasonal scales, making up for the scarcity of detailed ocean data. The ocean one-dimensional (1D) mixed layer models help in this regard, to guide analysis and interpretation of limited datasets. Many of these models use the prognostic approach of directly solving the 1D equations for momentum, scalars, and turbulent kinetic energy with parameterizations for the mixing by higher-order turbulence moments. The earliest of these was developed based on lab experiments by Turner and Kraus (1967). Later based on ocean observations, Pacanowski and Philander (1981) developed a 1st order closure model using measurements from equatorial undercurrent where shear is important for the mixing, which has applicability for oceanic thermocline. Another 1st order closure scheme called the "K" profile mixing parameterization (KPP) was developed for 1D modeling (Large et al. 1994) and used widely in TOGA COARE (Shinoda and Hendon 1998 and references therein) and thereafter. Noh and Kim (1999) developed yet another 1st order parameterization, designed to be more realistic for ocean mixed layers where vertical flux divergence and not shear production dominate the turbulent mixing. In addition to the popular 1st order closure schemes, mixed layer models have used more complex 2nd order schemes (Mellor and Yamada 1982) as well as more simplified bulk layer schemes (Price et al. 1986). Applications for these 1D mixed layer models include investigation of ocean SST response to intraseasonal variability (Shinoda and Hendon 1998) such as MJO (Bernie et al. 2005), which aid interpretation of TOGA COARE and similar datasets.

The application of 1D modeling is as a simplified tool for analyzing oceanic mixed layer behavior in the context of atmospheric variability. It is certainly not a substitute for three-dimensional ocean modeling and detailed observational campaigns conducted by physical oceanographers. In this chapter, the major impacts of identified intraseasonal disturbances on the variability of ABL vertical gradients and surface fluxes were the main research outcomes, with ocean model results providing opportunity for case study involving basic concepts of oceanic variability. The atmospheric side has not received as great emphasis in the review for this chapter because a more thorough general review of turbulence flux measurement and parameterization in the ABL follows in Chapter 5.

4.2 Convection and Vertical Transport at Experimental Site

Convectively-coupled waves are a major mechanism of moisture transport in the equatorial belt. While the convectively-coupled waves that passed over Seychelles (11-14 and 24-27 February) did not fit precisely into the framework of the linear wave types reported by (Kiladis et al. 2009) as discussed in Chapter 3, the evolving conditions in boundary layer were consistent with passing convective events. During the two identified periods (WWB1 and WWB2), enhanced localized convection was the main result of the vertical coupling that was directly observable on a largescale, but there were differences in the scale of convection, more so than in other aspects of these events. Figure 4.1 provides evidence of the vertical and horizontal scales of convective patterns at Seychelles site. Note that Figure 4.1b uses an identical dataset to Figure 3.11 (Meteosat-7 infrared measurements) but provides aerial view for better assessing the spatial scale than time-longitude diagram (Fig. 3.11). Figure 4.1 also demonstrates that the point and line measurements taken at Seychelles site were linked to larger-scale phenomena. These quasi-periodic phenomena impacted region surrounding Seychelles (mainly to the east) and therefore the ocean surface. This figure, which connects largescale aerial view to measurements directly from Seychelles surface, serves as a fitting transition into this chapter that focuses on the impacts observed in boundary layer locally at Seychelles.

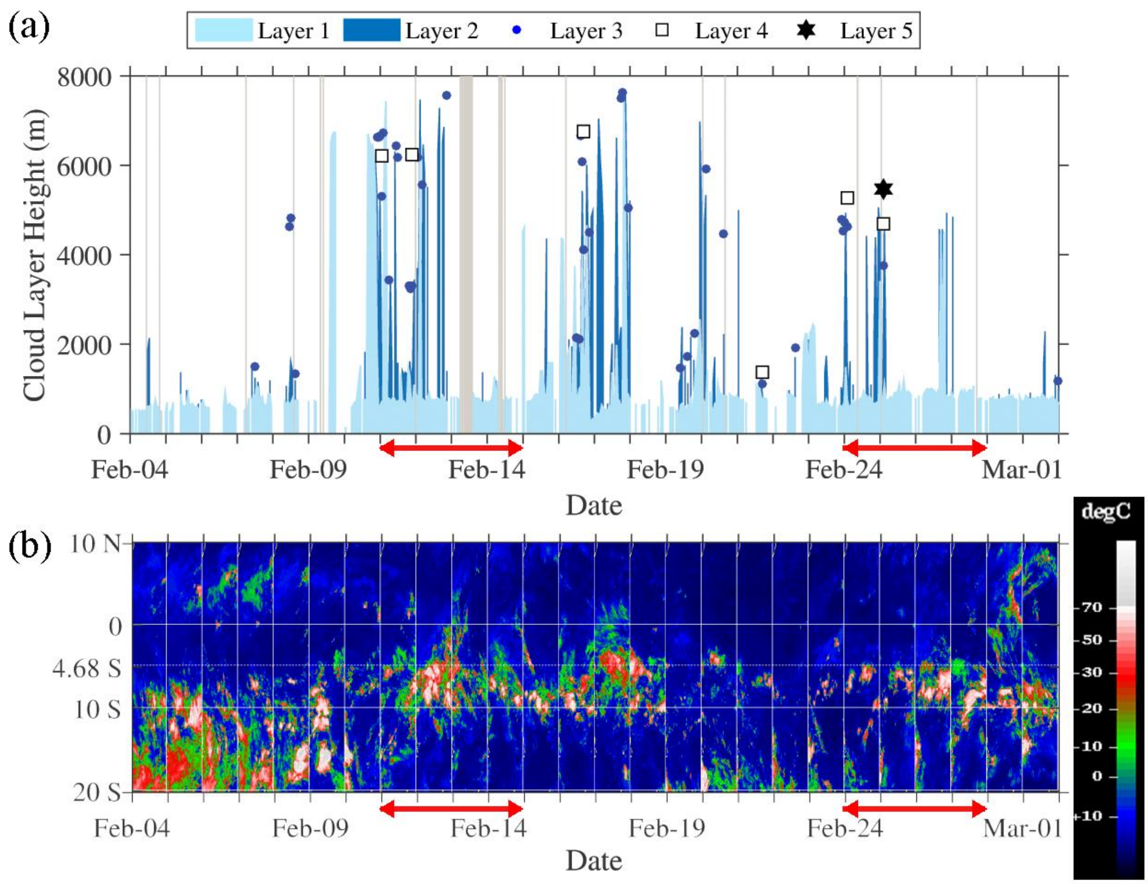

Figure 4.1: Largescale convective activity the in region of Seychelles. (a) Cloud layer heights from ceilometer located in Seychelles airport. For first and second cloud layers, light blue shading and dark blue shading, respectively, mark altitudes below the cloud base height. Layers 3-5 have symbol at cloud base height. Vertical grey bars indicate missing data. Horizontal red arrows designate same periods as lines in Chapter 3 figures (WWB1 and WWB2). (b) Time series images of infrared brightness temperatures measured by satellite (Meteosat-7) from 4 February to 2 March. Each of the 26 images was taken at 0000 UTC on a given day and included area from 10°N to 20°S and from 50°E to 60°E. Latitude of Mahé, Seychelles (4.68°S) marked by dotted white line in center. The images were treated with National Hurricane Center "rainbow" enhancement. Processed images were obtained from the Cooperative Institute for Meteorological Satellite Studies at the University of Wisconsin-Madison (http://tropic.ssec.wisc.edu/tropic.php).

4.2.1 Moisture transport

Increased cloud base heights and decreased cloud top temperatures in Figure 4.1 suggest significant changes to the moisture present in mid-troposphere during both WWBs. The full vertical extent of the moistening of troposphere can be viewed in Figure 4.2 based on data collected by microwave radiometer. Again as in Figure 4.1a, there was a difference in vertical scales between WWB1 and WWB2, which were estimated as ~9 km and ~6 km, respectively, from the relative humidity profiles. The water vapor above 5000 m is a result of convection occurring locally in Seychelles region which transported moist air from the marine boundary layer upward; the cloudiness is not just the result of stratiform clouds being advected into the area from a different region of convective activity. Although Figure 3.11 did indicate that the disturbances passing near Seychelles were moving in from the east, the high relative humidity throughout the profiles indicated active convection during much of the WWBs. Moist convection is an important component of hydrologic cycle, and since there were no significant precipitation events at Seychelles' airport site during these periods, the moisture transported upwards was eventually precipitated elsewhere.

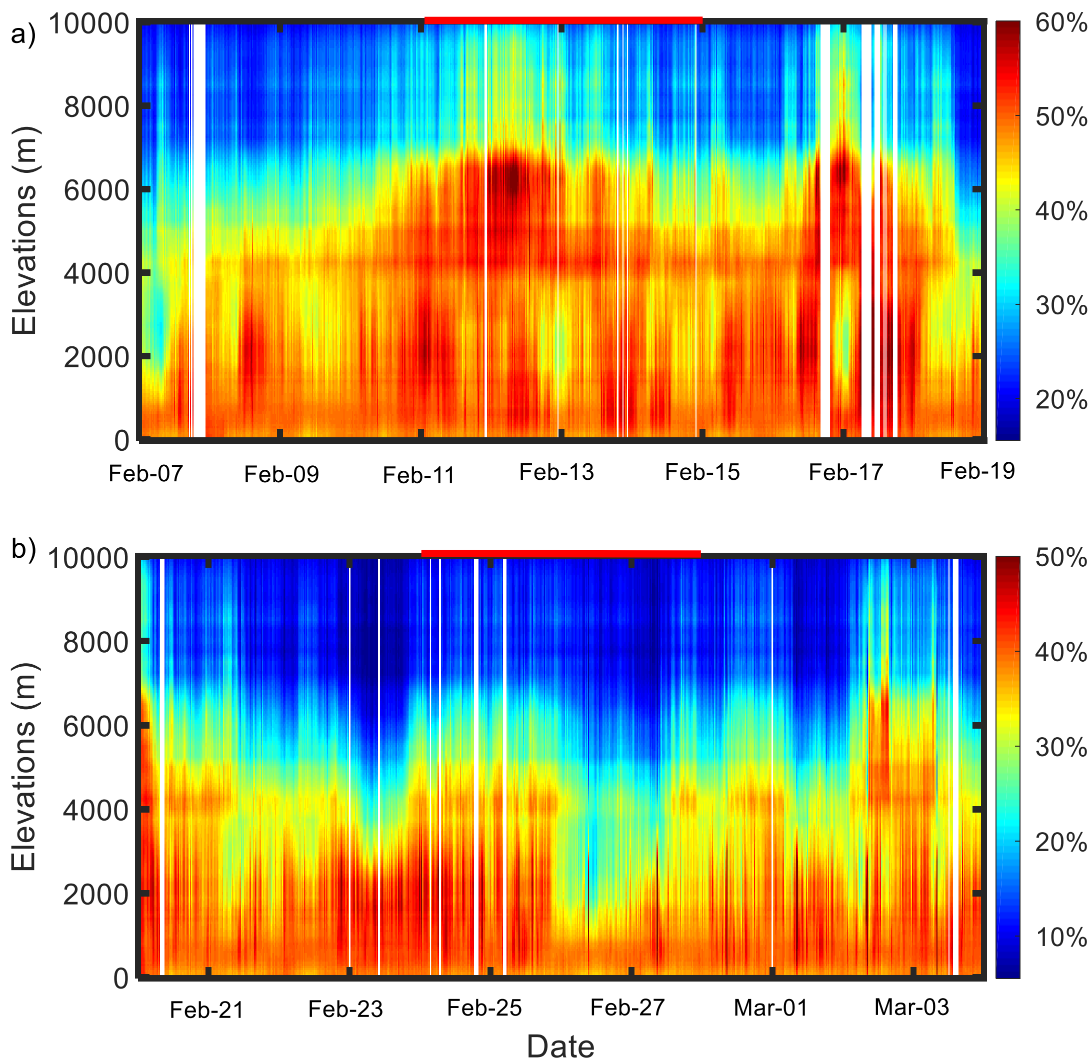

Figure 4.2: Time series of relative humidity profiles estimated by microwave radiometer before, during, and after (a) WWB1 and (b) WWB2. Here red bars are on top horizontal axis to avoid confusion with red data points on plot.

4.2.2 Vertical motions

Strong vertical motions are typically associated with convection, and the Doppler Lidar detected stronger vertical motions during WWBs as shown in Figure 4.3a and 4.4a. The vertical scans of Doppler Lidar deployed at Seychelles provided evidence of the increased magnitude of these vertical motions during the periods of enhanced upper-level moisture at Seychelles. Even though a day-long outage of Lidar during first event limited the data availability for WWBI, the larger magnitudes of vertical velocity during portions of this event were also significant. During the WWB2 in Figure 4.4a, strong negative vertical velocities of magnitude ~1 m s^{-1} dominated the boundary layer, accompanied by near-surface updrafts with positive vertical velocities (~0.5 m s^{-1}). While the fixed-point observations show the dominance of downdrafts, the convective activity is spread over a larger area replete with convective updrafts and downdrafts.

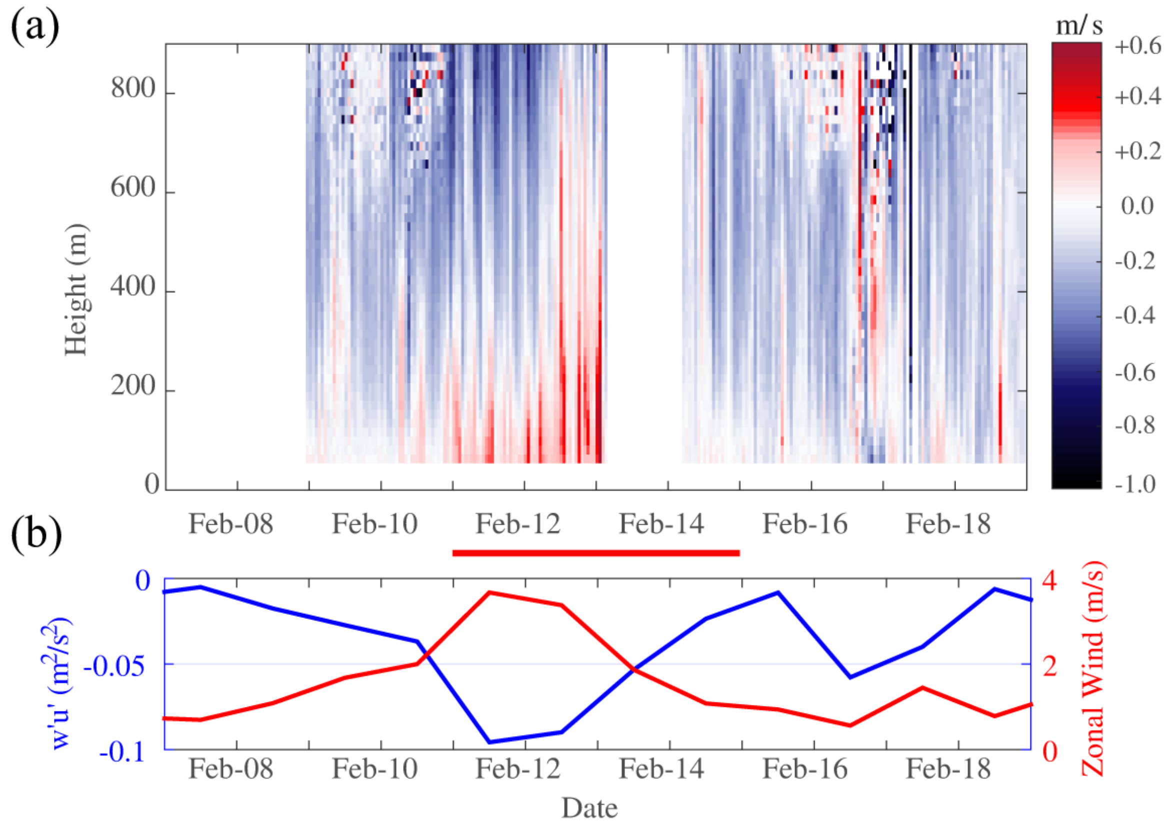

Figure 4.3: Surface measurements from Seychelles ground station before, during, and after the first observed westerly wind burst (WWB1). (a) Averaged hourly vertical velocity from Halo® Doppler Lidar vertical staring profiles. The vertical measurement resolution was 18 m, and the lowermost bins were left out of figure due to contamination. The noisiness in upper portions of some profiles, particularly before 11 February and on 16-18 February, was due to low signal-to-noise ratio at higher altitude due to periodic lack of aerosols. White space was due to Lidar not collecting data for these time periods. (b) Daily averaged Reynolds stress (blue) and westerly wind speed (red) measured by 10-m Young Model 81000 sonic anemometer on flux tower. The mean daily values were calculated based on hourly averages. The WWB period was marked with red line as in previous figures.

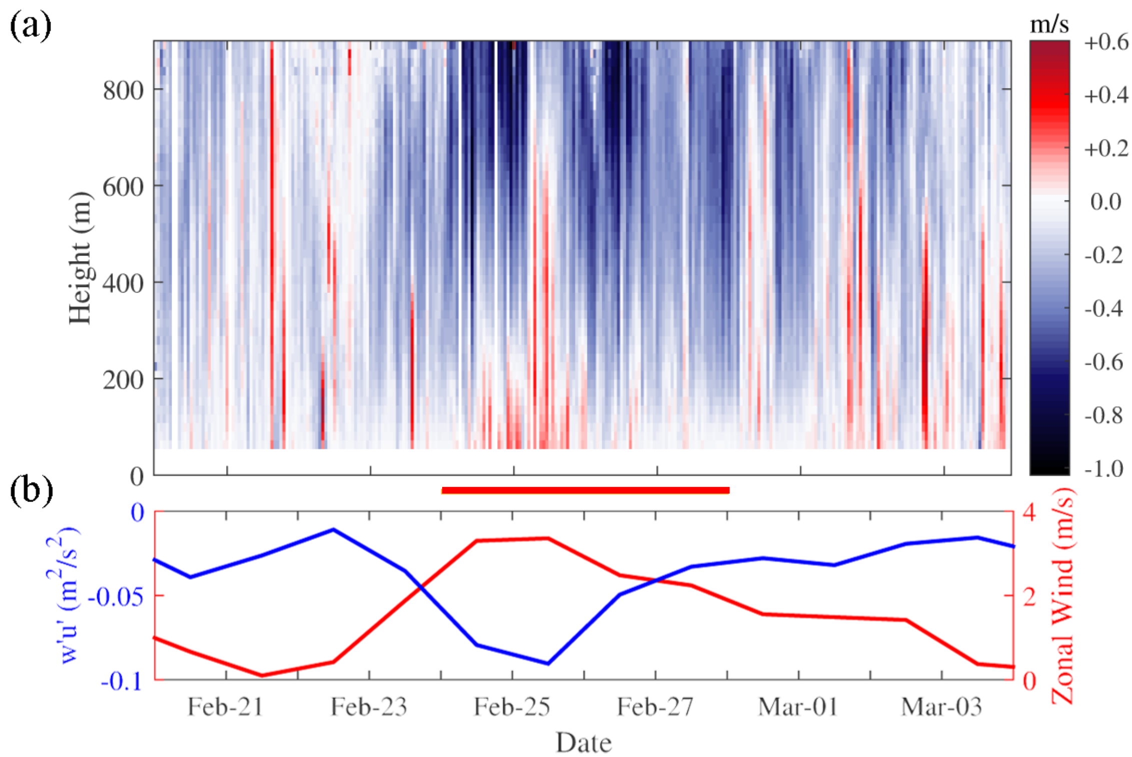

Figure 4.4: Surface measurements from Seychelles ground station before, during, and after the second observed westerly wind burst (WWB2). (a) Averaged hourly vertical velocity from Halo® Doppler Lidar vertical staring profiles. The vertical measurement resolution was 18 m, and the lowermost bins were left out of figure due to contamination. The noisiness in upper portions of some profiles was due to low signal-to-noise ratio at higher altitude due to periodic lack of aerosols. White space was due to Lidar not collecting data for these time periods. (b) Daily averaged Reynolds stress (blue) and westerly wind speed (red) measured by 10-m Young Model 81000 sonic anemometer on flux tower. The mean daily values were calculated based on hourly averages. The WWB period was marked with red line as in previous figures.

4.3 Energy Fluxes at Surface

4.3.1 Momentum

During the periods of enhanced vertical motions in the lower ABL, the energy balance at Seychelles surface station underwent significant changes. These periods were first identified as westerly wind bursts based on zonal velocity profiles from radiosondes; the surface measurements (10 m) confirmed this notion with maximum wind speeds and (negative) Reynolds stresses in Figures 4.3b and 4.4b during marked periods. These figures display how the tower measurements of increased momentum flux in surface layer were closely correlated with the larger magnitudes in Lidar vertical velocity. This suggests that vertical exchange processes of some kind were partly responsible for the changing wind conditions at surface; here we have proposed convective (up-down) motions that are not only thermally-driven but also pressure-driven (Fig. 3.15). The changing wind conditions, although from over coastal land, suggested that there would be an increased wind stress at sea surface during WWB (also see Figure 3.16), which could impact ocean mixed layer dynamics as well as drive waves and currents.

4.3.2 Moisture

The bursting winds caused enhanced turbulence near surface in ABL as was indicated by turbulence parameters such as Reynolds stress (Figs. 4.3b and 4.4b) and rms velocities (not pictured). Scalar transport would be enhanced with stronger turbulence, which is important for the convection due to vertical transport of water vapor (moisture). Figure 4.5 shows the moisture flux from 10-m flux tower (sonic anemometer and LI-COR® gas analyzer). The daily moisture flux attained a local maximum value on the first day of each WWB, significantly above the background value. The higher moisture fluxes was partly attributable more evaporation at surface (including sea surface since the flux tower at coastal site was downwind of an ocean bay), which is directly related to wind speed in many evapotranspiration formulations. Overall the upward moisture flux would contribute to the active convection that occurred in Seychelles region during WWBs. It should be noted that the moisture flux was above the average value for a couple days before WWB1 and below average before WWB2. Therefore, differing rates of moisture transport in surface layer during those pre-WWB days may affect the preconditioning of air mass near Seychelles for the (deep) convection following the vertical coupling. This is just hypothesis to explain the major difference between the two WWB events and needs verification. At the fixed station location the moisture flux declined after initial onset of strong convection due to transitioning to different stages of convection (i.e., stratiform) and fading westerly surface winds.

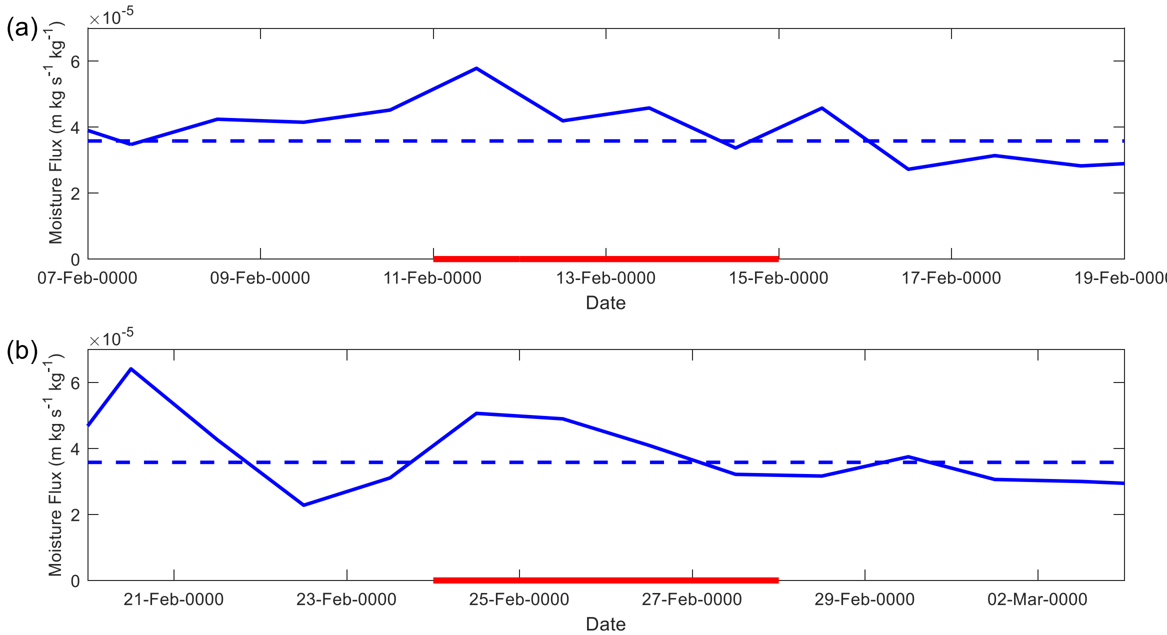

Figure 4.5: Kinematic vertical turbulent moisture flux ($\overline{wq}$) at Seychelles (10-m height) for (a) WWB1 and (b) WWB2. The dashed blue line is the mean (background) moisture flux observed during the field campaign (6 February to 15 March 2015).

4.3.3 Heat

The heat transport within ABL was also altered during the WWBs. Radiative forcing governs the total incoming heat flux with the heat balance at the lower air-sea or air-land interface given by equation

$$Q_{net} = -SW_{dn} + SW_{up} - LW_{dn} + LW_{up} + LH + SH \qquad (4.1)$$

where Q_{net} is the total heat flux into ocean or ground, SW_{dn} and SW_{up} are the upwelling and downwelling shortwave radiative fluxes, LW_{dn} and LW_{up} the same for longwave radiative fluxes, LH is the latent heat flux ($\rho_a L_e \overline{wq}$), and SH the sensible heat flux ($\rho_a c_p \overline{w\theta}$). The net downwelling radiative flux at surface is dependent on the albedo through the entire atmospheric column, and, due to convective cloud formation at the onset of surface WWBs, SW_{dn} decreased below background value (Fig. 4.6) during the first two days of WWBs. Since shortwave radiation is the principle energy source varying over diurnal to intraseasonal timescales, it can have significant impact on other variables in Eq. 4.1. Notably for ABL, the incoming radiative heat flux near the surface is correlated with the sensible heat flux (*SH*), i.e., the conductive heat flux from surface to atmosphere, as can be seen from Figure 4.6. Besides SW_{dn} and *SH*, the latent heat flux (*LH*) was the other measured variable that displayed significant changes during WWBs. The *LH* was directly related to moisture flux in Figure 4.5 so was not plotted to avoid redundancy. The downwelling longwave radiative flux (not pictured) remained comparatively constant through WWBs while the upwelling radiative fluxes were highly dependent on heterogeneous land surface beneath flux tower so not representative for studies at scales larger than horizontal microscales. The cumulative effect that the variables in Eq. 4.1 have on ocean heat flux (Q_{net}) is investigated in the following section.

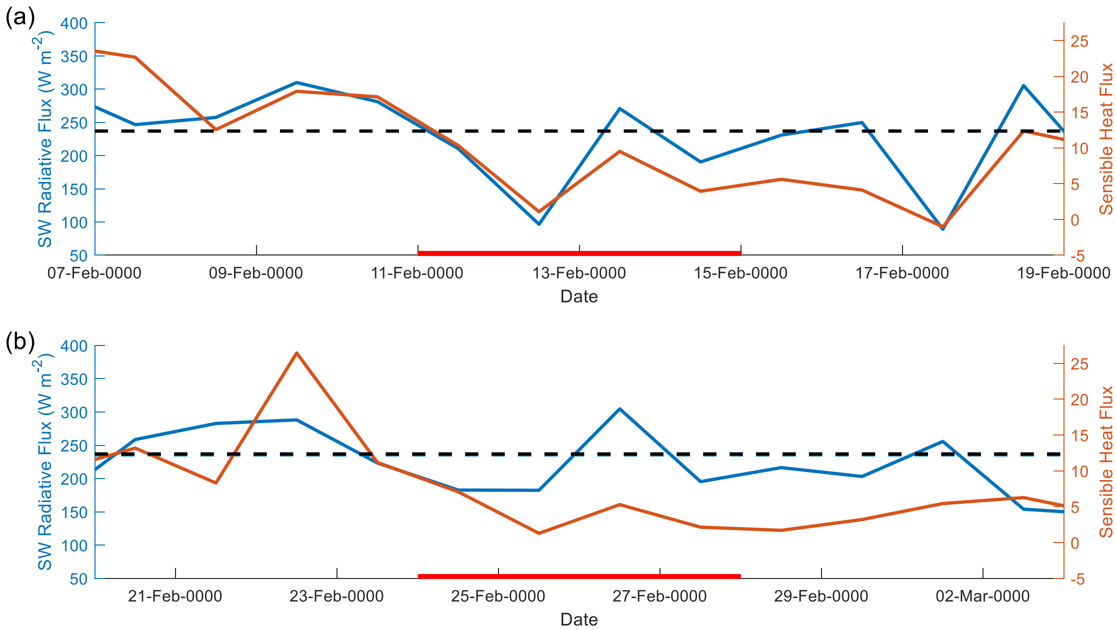

Figure 4.6: Shortwave radiative flux (SW_{dn}) and sensible heat flux (SH) from 10-m height at Seychelles station for (a) WWB1 and (b) WWB2. The dashed black line indicates the mean (background) value for both variables observed during the field campaign (6 February to 15 March 2015).

4.4 Air-Sea Interactions

The WWBs occurred primarily over ocean surface (Fig. 3.16), so understanding their impact on air-sea interactions in western equatorial Indian Ocean is an important aspect of this research. Measurements collected during ASIRI-RAWI were from over coastal land, but limited data near ocean surface were available from public-access datasets. Furthermore, oceanic mixed layer modeling was utilized to estimate the range of responses that upper ocean may have to WWBs' modulation of surface atmospheric conditions.

4.4.1 Ocean moorings

The Research Moored Array for African-Asian-Australian Monsoon Analysis and Prediction (RAMA) was utilized to obtain further data for this study. However, not all the buoys in the array were functioning during ASIRI-RAWI campaign. The only buoy in the region of interest for the tropospheric disturbances was located at 4°S 80°E, approximately 25° longitude (~2700 km) to the east of Seychelles site; some surface (3-4 m) meteorological variables are shown in Figure 4.7 for February 2015. Two pulses of above-average westerly winds corresponded to the passage of mid-lower-tropospheric disturbances over this portion of central IO (Figures 3.9-3.12). These bursts of wind velocity were correlated with higher humidity, lower temperature, and even precipitation events, suggesting that the tropospheric disturbances were convectively coupled at this longitude (Figure 3.11 may confirm this). The period of disturbances appeared to be 7-10 days at this buoy, which is different than the ~13-16 day period of the vertical coupling observed at Seychelles. This mismatch may more strongly support the idea that upper-level (geopotential) anomalies were important for determining the vertical interactions happening in western IO and that the sea surface disturbances are swayed by other disturbances as discussed earlier. Note the early-arriving, prolonged positive zonal wind anomaly for the second event may be related to short-lived, eastward-propagating burst of momentum at surface, which appeared in reanalysis in central IO but not near Seychelles (see in Figure 3.12 on 19 February around 80-90°E).

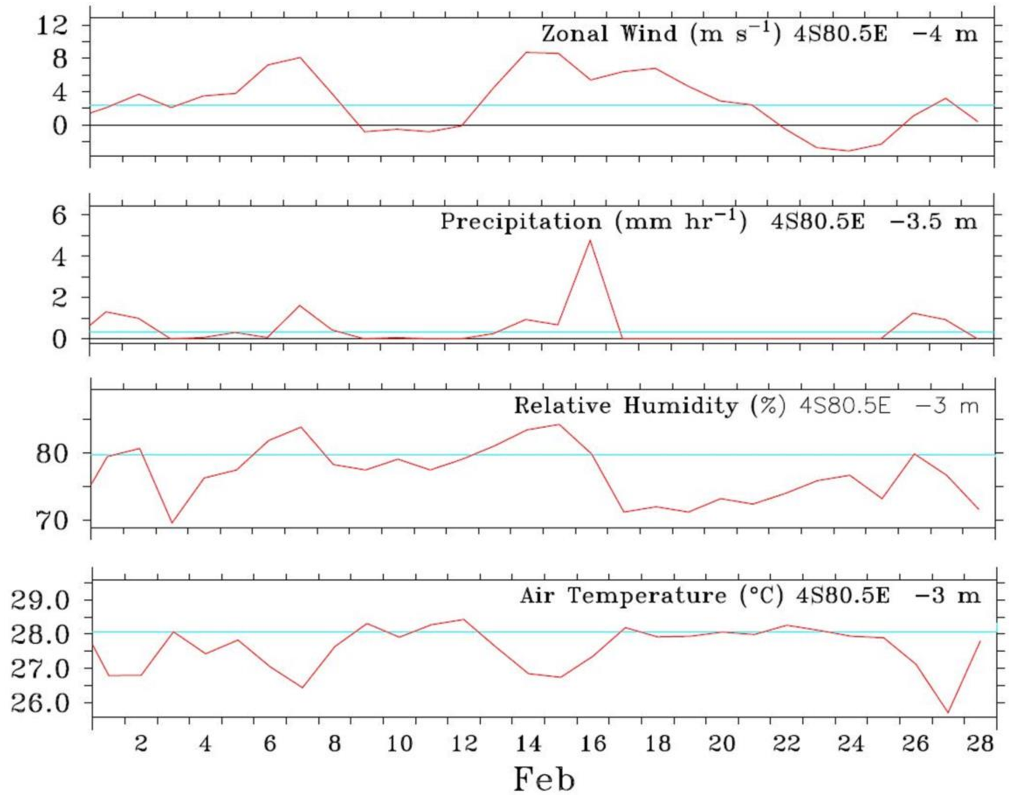

Figure 4.7: Surface meteorological variables from RAMA (McPhaden et al. 2009) buoy at 4°S 80.5°E in central Indian Ocean for month of February 2015: zonal wind velocity, precipitation rate, relative humidity, and air temperature. These plots were downloaded from https://www.pmel.noaa.gov/tao/drupal/disdel/ in May 2015.

4.4.2 Ocean mixed layer model

Owing to the limited availability of ocean observations during ASIRI-RAWI experiment in western IO, we have utilized a 1D ocean mixed layer model to estimate the generalized effects of the WWBs on sea surface temperature (SST) and ocean mixed layer dynamics. The model used has been an updated version of the Noh ocean mixed layer model for oceanic boundary layer (Noh and Kim 1999). A one-dimensional model, it is based on the prognostic equations of mean current velocity (zonal and meridional), temperature, salinity, and turbulent kinetic energy. The model's turbulence closure scheme was developed explicitly to represent the dynamics of the oceanic boundary layer. As is typical in such schemes, the turbulent fluxes are parameterized in gradient transport form with eddy diffusivities and viscosities, and the Noh model incorporates the effects of stratification via a turbulent Froude number $\sigma l/N$ where σ and l are the turbulence velocity and length scales, respectively. An updated version of the Noh model was utilized that accounts for effects of Langmuir circulations (Noh et al. 2011, 2016) for more realistic treatment even though these circulations are known to have less of impact in equatorial oceans

The numerical experiments were performed using the Noh mixed layer model by a collaborator at Yonsei University, Hyejin Ok, under the supervision of Dr. Yign Noh. We selected boundary conditions at ocean surface based on atmospheric observations taken at Seychelles flux tower. The main feature of the WWBs was the increased wind stress in surface layer of ABL so this was targeted for investigation in the numerical studies. The mean daily Reynolds stress increased from a background value of 0.03 m^2 s^{-2} to 0.10 m^2 s^{-2} for 4-day period to approximate the effects of a WWB (Figs. 4.3b and 4.4b). 15 days of this wind stress forcing condition at model's upper boundary are shown in Figure 4.8a. The Reynolds stress measured at tower during WWB (0.10 m^2 s^{-2}) was equivalent to a 10-m wind speed of 8.8 m s^{-1} over open water based on bulk formulations. This seems reasonable based on Figure 4.7 (top panel) which showed daily-averaged westerly wind speeds peaking over 8 m s^{-1} at 4-m height. Note that initial vertical profile for velocity applied to the ocean column was for zero velocity.

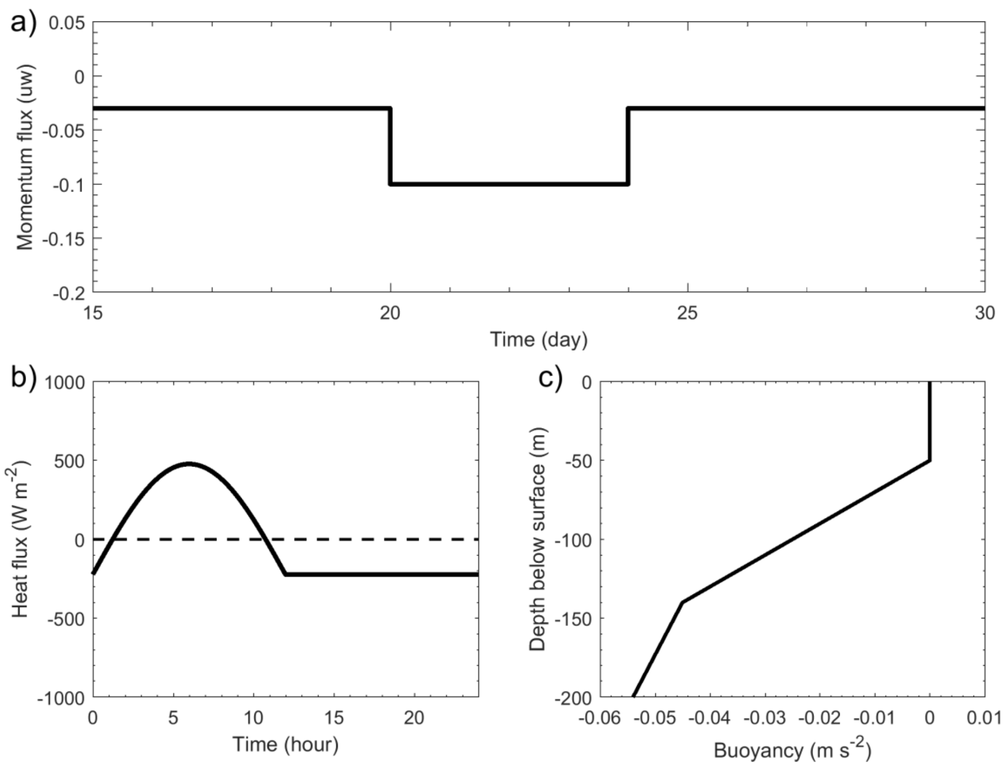

Figure 4.8: Initial and boundary conditions for ocean mixed layer model. (a) Reynolds stress ($\overline{uw}$) forcing condition applied to model during final 15 days of simulation with background value and 4 days of stronger WWB boundary conditions. (b) Diurnal thermal forcing applied as heat flux to upper layers of model every day of simulation. Note that Jerlov's water type II was considered (Paulson and Simpson 1977) so solar irradiance penetrated depths below top model level for the incoming shortwave radiative flux (sinusoidal portion) only. (c) Vertical profile of initial conditions for buoyancy for case of mixed layer depth (MLD) of 50 m and pycnocline stratification $N^2 = 5{\cdot}10^{-4}$.

The boundary conditions for heat flux were not considered to vary day-to-day during the simulations because, as mentioned, the focus was on the more significant momentum forcing changes. However, it was important to apply an appropriate heat flux in order to capture the diurnal variability of ocean mixed layer and how it was impacted by bursting winds. Eq. 4.1 was used to determine an appropriate diurnal cycle of ocean heat flux (Q_{net}) boundary conditions for top layers of the 1D ocean mixed layer model. Terms on right-hand side of Eq. 4.1 included those observed tower fluxes (SW_{dn}, SH, LH, and LW_{dn}) as well as upwelling radiative fluxes, which were estimated based on assumed ocean surface properties. For the upwelling radiative flux ($SW_{up} = \alpha_o \cdot SW_{dn}$), the ocean albedo α_o was assumed to be 0.06 so that it was a relatively small term. Upwelling longwave radiative flux ($LW_{up} = \sigma \cdot \mathrm{SST}^4$ where σ here is Stefan-Boltzmann constant) was assumed constant for simplicity based on SST of 30°C. The incoming shortwave radiative flux, the Earth system's principle energy source, had by far the largest mean value and diurnal amplitude, and therefore dominated the calculated Q_{net} as well as the fluctuations of other terms in Eq. 4.1 such as SH (see Figure 4.6). All other terms were opposite in sign and their cumulative effect was approximately constant. Therefore, a simple, idealized diurnal profile was developed to approximate real heat flux Q_{net}; one diurnal cycle of this heat flux is displayed in Fig. 4.8b. The idealized Q_{net} profile is approximated with a half-sinusoid of heating during daytime (12 hours; amplitude of 700 W m^2) representing mainly SW_{dn} and all-day constant cooling for other terms. The value applied for constant cooling was selected such that there was zero net heat flux between ocean and atmosphere over the course of simulations, as has been the practice in mixed layer modeling applications from the early days (Turner and Kraus 1967). This is done to avoid incorporating larger time scales of variability (seasonal to climate) on which significant net heat transfer between ocean and atmosphere may occur. Therefore diurnal heat cycle was kept neutral to prevent long-term accumulation or loss of heat by model.

Initial conditions for the ocean vertical profile were set based on a small number of observed vertical profiles from the same region around Seychelles and during the appropriate season (late boreal winter, i.e., February and March). These included observations of a Spray glider during NASCar intensive observational period in early 2017 (Centurioni et al. 2017) and some profiles from Argo float program's data archive from 2010-2015. Based on these observations, an idealized profile with a strong stratification of $N^2 = 5 \cdot 10^{-4}$ and MLD = 50 m was selected as displayed in Figure 4.8c. A couple profiles suggested that shallower MLD was possible when ocean was strongly stratified in this region so MLD = 10 m was also used to give an idea of range of ocean mixed layer responses possible. Results could depend strongly on these initial conditions as revealed by numerical experiments that are presented below and others; the scope of this case study was limited to exploring only the most realistic conditions. A model spin-up time of 15 days was used so that the initial conditions had sufficient time to adjust to background forcing and reach quasi-stationary state.

The results from simulations are displayed in Figures 4.9 and 4.10 below. MLD was defined here based on the depth at which a 0.2°C difference between local water temperature and SST first occurred. The total mixed layer deepening that occurred during WWBs for both initial conditions (MLD = 10 and 50 m) was similar (ΔMLD ≈ 4 m). Another key change to MLD during burst is the disappearance of a diurnal cycle. The heating during daytime with lower wind stress led to strong stratification in upper 10 m, but during WWBs strong wind stress competed with surface heating through enhanced turbulence mixing, eliminating the formation of a sublayer of significantly warmer (> 0.2°C) water near the surface. The temperature within the mixed layer, which is equivalent to SST based on MLD definition, decreased more during WWBs. The enhanced turbulence which was deepening the mixed layer causes the cooler water beneath the relatively steep pynocline to be entrained and mixed throughout layer, contributing to the decrease of overall temperature of the mixed layer. For the case of deeper MLD (Figure 4.8), the temperature decrease is less because the mixed layer is essentially more voluminous so addition of cooler water makes less of a difference. Therefore for shallower MLD case (Figure 4.9), the decrease of SST is more significant (by ~0.5 °C) with the entrainment of cooler water from below. The cooling due to turbulent mixing is irreversible for these simulations and could only be offset with an external net heat flux applied to the mixed layer. Although enhanced surface momentum flux (from Reynolds stresses in Figs. 4.3b and 4.4b) during WWBs was imparted on the upper ocean (Fig. 4.8), westerly currents within mixed layer were not increasing substantially. The currents are influenced by inertial motion due to small Coriolis force south of the equator where WWBs were centered (2.5-7.5°S) with a period of roughly 5.5 days (not shown). The Reynolds stresses do have a role in controlling the uppermost ocean surface currents.

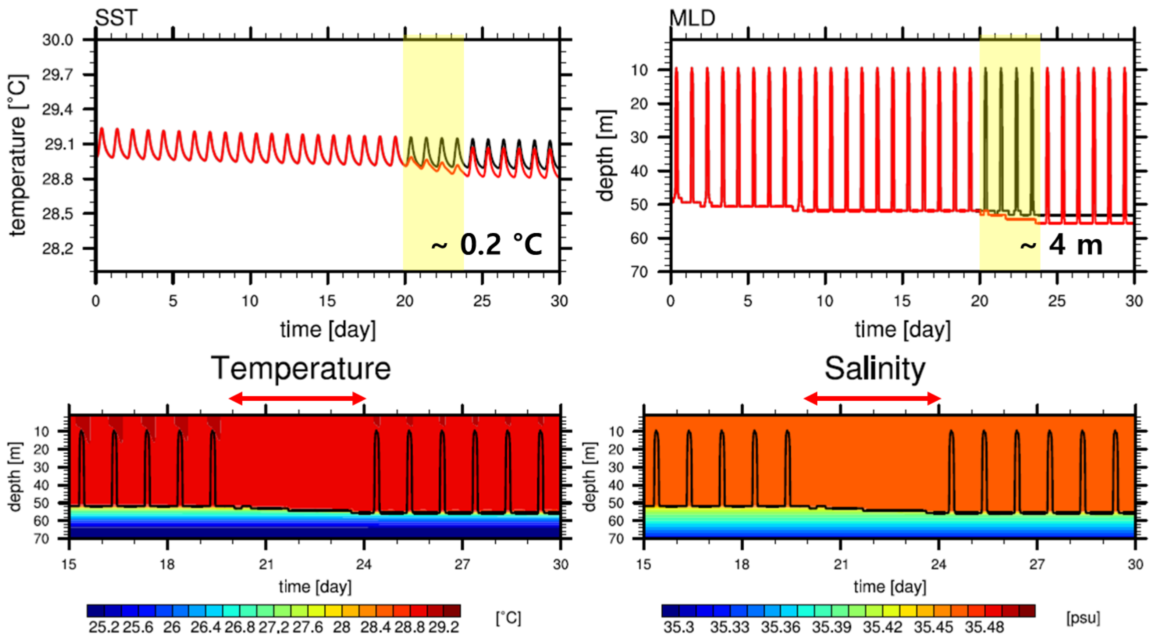

Figure 4.9: Results from numerical simulations of ocean mixed layer model using initial and boundary conditions given in Figure 4.8. The temporal evolution of key parameters SST and MLD for full simulation is given in the upper panels with yellow highlighting WWB. The background case (red) is compared to WWB case (black) here with the approximate differences caused by WWB as 0.2°C and 4 m for SST and MLD, respectively. Note that the first part of simulation in upper panels was for model spin-up. The lower panels provide time series contours for the final 15 days of simulation including WWB. Black lines here indicate MLD and red arrows the WWB period.

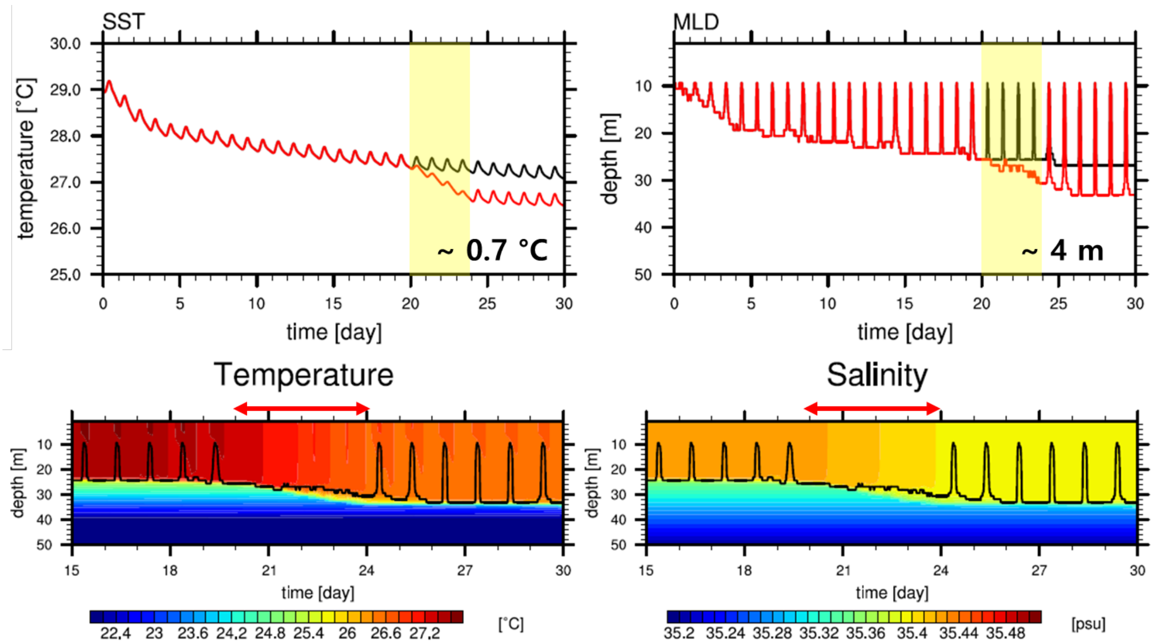

Figure 4.10: Results from numerical simulations of ocean mixed layer model using boundary conditions given in Figure 4.8a but initial conditions of 10-m MLD. The temporal evolution of key parameters SST and MLD for full simulation is given in the upper panels with yellow highlighting WWB. The background case (red) is compared to WWB case (black) with greater cooling of SST (0.7°C) and the same deepening of MLD (4 m) as compared to Figure 4.9. Note that the first part of simulation in upper panels was for model spin-up. The lower panels provide time series contours for the final 15 days of simulation including WWB. Black lines here indicate MLD and red arrows the WWB period.

4.5 Additional Case Study on Boundary Layer Modulation: Sri Lanka

Analyses of observations from Sri Lanka site were conducted in the context of ASIRI project in the Bay of Bengal (BoB), and preliminary results have been described in Wijesekera et al. (2016). The time series of meridional and zonal wind profiles are given in Figure 4.11a-b. Above 12 km there is some evidence of zonal wind anomalies from the Kelvin waves of Chapter 3 but with lower amplitudes and less consistency than at other sites (Fig. 3.2), which is appropriate given its greater distance from equator. Another equatorial wave might be present around 9-12 km with both meridional and zonal components, which is most clearly shown by the corresponding southerly and easterly anomalies in first several plotted profiles of Figs. 4.11a-b. This could be a mixed Rossby-gravity wave, but identification requires further investigation. Low Ri_g values above 10 km on 11 February (Fig. 4.11e) likely promoted turbulent mixing and downward descent of dry upper-tropospheric air prior to this date as shown in Figure 4.11c.

Downward descent of dry air continued from 10 km with approximately unstable atmospheric conditions until ~ 5 km, where stable layer with maximum gradient Richardson number Ri_g ~ 10-15 (Fig. 4.11e) impeded the descent, though downward mixing continued, albeit at a slower rate. By 15 February (Fig. 4.11e), maximum Ri_g decreased substantially to 4-5. Ri_g ~ 1 is the condition for maximum rate of stratified turbulent mixing (Strang and Fernando 2001a), so the values approaching 1 are favorable for enhanced mixing, especially considering the vertical measurement resolution (25 m) can influence evaluation of Ri_g values (De Silva et al. 1999). The enhanced mixing permitted transport of significant amounts of dry air towards the surface from aloft. In lowermost troposphere Ri_g is reduced to near 1 which might be the necessary condition for entrainment of the dry air into mixed layer directly above surface as in Bhat and Fernando (2016). The dry air mixed with existing surface moist air (70-90% relative humidity), thus reducing ground level relative humidity and also the temperature, as a result of evaporation (see 15-17 February in Fig. 4.11c-d). The high relative humidity prior to the event appears to have been contributed to by the rain events (9, 10, 11 and 13 February) whereas the drying of lower troposphere also may have been partly contributed by northerly flow from relatively drier Indian landmass starting on 14 February.

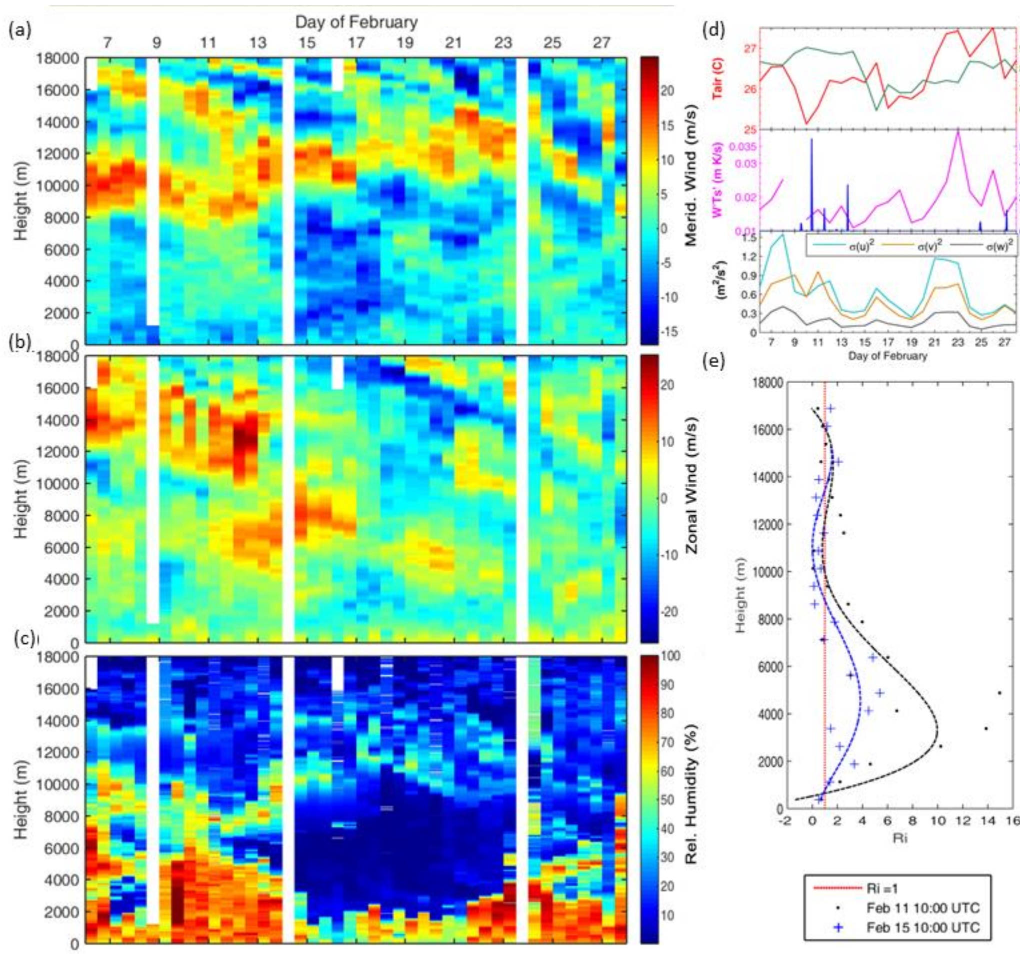

Figure 4.11: Upper air and surface measurements from Colombo, Sri Lanka (cf. Wijesekera et al. 2016): Height-time plots of (a) meridional wind, (b) zonal wind, and (c) relative humidity from the soundings at Department of Meteorology site; (d) Daily averaged values of relative humidity (*RH*), air temperature (*Tair*), rainfall rate (*Rain*) and streamwise, crosswise and vertical velocity variances $\sigma^2(u)$, $\sigma^2(v)$, $\sigma^2(w)$ as measured at the flux tower; (e) Vertical profiles of bin-averaged gradient Richardson number during two different representative soundings. The dashed lines are quartic polynomial fits to the bin-averaged data to show general trends.

The drop of surface temperature was associated with a reduction of convective activity near surface, as evident from the reduced heat flux and velocity variances (Fig 4.11e) as well as the height of convection (from ceilometer, not pictured). Reduced moisture further led to suppression of rainfall until 25 February, when surface moisture has increased close to the previous levels and the upper-level moisture has increased substantially to resuscitate rainfall activity. It is interesting to note that the same patterns for relative humidity and temperature have been observed in the RAMA mooring at 8°N 90°E in BoB, which is in the same latitudinal band of the Sri Lanka site. This suggests that the vertical transport phenomena observed in Sri Lanka may also be occurring in the BoB, with modulations of near-surface heat and moisture fluxes, thus affecting air-sea exchange processes. In all, the preliminary results from Sri Lanka pointed to the significant role that multi-scale processes, from regional scale upper atmospheric flows to entrainment across stratified layers to mixing in the ABL, play in air-sea interactions in the BoB.

4.6 Summary and Conclusions

The tropical ABL readily responds to combined forcing of disturbances passing over at a multitude of scales and at different heights. In this chapter the ABL's response to two quasi-periodic series of events in overlying layers was described. These periods were noted for strong westerly winds in surface layer (WWBs) as well as stronger vertical velocities linked to convective activity. Although there were differences in the scales of convection possibly due to moisture availabilities, similarities in the modulation of momentum, heat, and moisture fluxes by the quasi-periodic disturbances were clear. These WWB periods indeed saw some of the most anomalous surface conditions during the field campaign that occurred for multi-day periods.

Perhaps the most consequential ABL modifications from these anomalous events were the high low-level wind speeds and their implications for sea surface. Locally in Seychelles such high wind can have negative impacts on marine vessel operations for tourism and fishing industries, two of the biggest sectors of the national economy, but important for this work was the potential impact on air-sea interactions for coupled ocean-atmosphere modeling. Given the lack of relevant ocean data, a 1D ocean mixed layer model was used to estimate how the ocean may respond to WWBs, which occurred over hundreds of thousands of square kilometers. Simulations demonstrated that there was wide variability in oceanic behavior based on initial conditions, but a few scenarios were selected to check the range of possible oceanic responses. The mixed layer deepening was evident during periods of stronger momentum flux, producing turbulence through the vertical column of mixed layer. Most notable was the elimination of diurnal MLD because the stronger wind stress and hence turbulent mixing outcompeted buoyancy effect of daytime heating. The WWBs were also shown to have an effect on the SST, with magnitude depending on the initial state of mixed layer.

CHAPTER 5:

MEASUREMENTS OF MIXING PARAMETERS IN ATMOSPHERIC STABLY STRATIFIED PARALLEL SHEAR FLOW

5.1 Problem Statement and Literature Review

Quantification of turbulent mixing in stably stratified fluids is an intricate problem that has been studied extensively, yet continues to be at the center of much debate (Ivey et al. 2008). How much buoyancy flux is generated for a given turbulence production rate? And how much of this flux is converted irreversibly to increase the potential energy of the system? – These are important questions of great practical relevance in environmental flow modeling and in industrial applications. The buoyancy flux $\overline{bw}$ signifies the breakdown of mean buoyancy gradient to produce smaller scale inhomogeneities, which is an example of the 'stirring' phenomenon. 'Mixing' is the molecular scale (irreversible) homogenization of these smaller scale buoyancy inhomogeneities. The stirring and mixing terms explicitly appear in the turbulent kinetic energy (TKE; $\overline{q^2}/2$) and potential energy $\overline{b^2}/2N^2$ equations, respectively. Here b is the fluctuating buoyancy, w the fluctuating vertical velocity, and N the buoyancy (Brunt-Väisälä) frequency. If for simplicity we assume a parallel shear flow in x direction with mean velocity $\overline{U}(z)$, where z is the vertical coordinate antiparallel to gravity, then the turbulent kinetic energy equation is

$$\frac{\partial \overline{q^2/2}}{\partial t} + \overline{U}\frac{\partial \overline{q^2/2}}{\partial x} = -\overline{uw}\frac{\partial \overline{U}}{\partial z} - \frac{\partial M_z}{\partial z} + \overline{bw} + \overline{f_i u_i} - \varepsilon, \tag{5.1}$$

(Ⅰ) (Ⅱ) (Ⅲ) (Ⅳ) (Ⅴ) (Ⅵ) (Ⅶ)

where $M_z = \overline{q^2 w}/2 + \overline{pw}/\rho$ is the diffusive TKE flux, p the fluctuating pressure, ρ the fluid density, f_i a body force other than buoyancy, ε the TKE dissipation rate, and u_i = (u,v,w) are the instantaneous velocity fluctuations. By the same assumptions the turbulent potential energy equation is

$$\frac{\partial \overline{b^2/2N^2}}{\partial t} + \overline{U}\frac{\partial \overline{b^2/2N^2}}{\partial x} = -\overline{bw} - \frac{\partial \overline{b^2 w/2N^2}}{\partial z} - \varepsilon^b, \tag{5.2}$$

(Ⅷ) (Ⅸ) (Ⅹ) (Ⅺ) (Ⅻ)

where $\varepsilon^b = \kappa N^2 \overline{(\partial b/\partial x_j)(\partial b/\partial x_j)}$ is the potential energy dissipation rate and κ the molecular diffusivity. Eq. 5.2 shows that the rate of increase (Ⅷ), horizontal advection (Ⅸ), and vertical turbulent diffusion (Ⅺ) of buoyancy fluctuations are directly related to change of buoyancy flux $\overline{bw}$ (Ⅹ) while a portion of the potential energy fluctuations is irreversibly dissipated (Ⅻ). For stably stratified flows, $\overline{bw}$ is typically negative (it can oscillate for decaying turbulence) and causes a reduction of TKE in Eq. 5.1 (Ⅴ). Conversely, the production of TKE is often dominated by shear (Ⅲ), but the TKE at a given location can also be supplied by horizontal advection of TKE (Ⅱ) and the diffusive flux divergence (Ⅳ). Body forces (Ⅵ) other than buoyancy, if present, can also affect the TKE. The viscous dissipation (Ⅶ) always reduces the TKE, and the dissipation of turbulent potential energy fluctuations occurs by (Ⅻ).

In applications, (Ⅴ) becomes important because the eddy diffusivity of a scalar K_ρ used in models is directly related to it as $K_\rho = -\overline{bw}/N^2$. The measurement of $\overline{bw}$ in the ocean is difficult due to practical limitations, but ε is readily estimated from microstructure measurements. Therefore, to the first order, K_ρ is estimated using measured ε and the assumptions of stationarity, horizontal homogeneity, and the absence of diffusive flux divergence and other body forces. Eq. 5.1 then becomes

$$0 \approx -\overline{uw}\frac{\partial\overline{\overline{U}}}{\partial z} + \overline{bw} - \nu\overline{\left(\frac{\partial u_i}{\partial x_j}\right)\left(\frac{\partial u_i}{\partial x_j}\right)} = P - B - \varepsilon, \tag{5.3}$$

where P and $B(=-\overline{bw})$ have been introduced as notations for shear production (Ⅲ) and the magnitude of the buoyancy flux (Ⅴ). Similarly, Eq. 5.2 becomes

$$0 \approx -\overline{bw} - \varepsilon^b = B - \varepsilon^b. \tag{5.4}$$

The flux Richardson number, often called the mixing efficiency, is a commonly used parameter defined as the ratio of the buoyancy flux to the TKE production by shear, i.e.,

$$Ri_f = \frac{B}{P} \approx \frac{B}{B+\varepsilon} \approx \frac{\varepsilon^b}{\varepsilon^b+\varepsilon} = \frac{\Gamma}{1+\Gamma}, \tag{5.5}$$

where $\Gamma = B/\varepsilon \approx \varepsilon^b/\varepsilon \approx Ri_f/\left(1 - Ri_f\right)$ is called the mixing coefficient. Note that for the special conditions considered here B is also the rate of dissipation of potential energy fluctuations (or mixing) by Eq. 5.4. According to Ellison (1957), the flux form of the Richardson number Ri_f was first introduced by E. L. Deacon, and it has been widely used ever since. The eddy diffusivity can be written as

$$K_\rho = \Gamma\frac{\varepsilon}{N^2}. \tag{5.6}$$

Using the previously hypothesized value of $Ri_f \leq 0.15$ (Ellison 1957), Osborn (1980), obtained the result $\Gamma \leq 0.20$, and now it is customary for oceanographers to use a fixed value (Γ=0.2) when applying Eq. 5.6. This relationship obviously depends on the same assumptions made in deriving Eq. 5.3, that is a balance between P, B, and ε. While in Osborn model the TKE supply mechanism is taken as shear production (P), other supply mechanisms can be present, for example, the diffusive flux divergence (Hopfinger and Linden 1982) or fluctuating body forces (Maffioli et al. 2016). There is an open question of whether these different mechanisms or a combination thereof would lead to the same Γ. For example, Turner (1979) pointed out that mixing rates corresponding to internally (e.g., shear production) and externally (e.g., diffusive flux reaching the mixing location) generated turbulence can be fundamentally different. Additionally, even in the presence of a single turbulence generating mechanism, Γ can be dependent on multiple parameters (Ivey et al. 2008; Ivey and Imberger 1991; Mater and Venayagamoorthy 2014). Laboratory experiments (Linden 1980; Strang and Fernando 2001b), numerical simulations (Maffioli et al. 2016), and field data (Pardyjak et al. 2002; Monti et al. 2002; Lozovatsky and Fernando 2012) all point to the variability of Ri_f (and thereby Γ by Eq. 5.5), with dependence on one or more governing parameters. Yet, single parameter approaches to describe mixing continue to be in wide use, for instance, the level 2 and 2.5 order turbulence closure schemes of Mellor and Yamada (1982) that utilize sole dependence of Ri_f on the gradient Richardson number (Ri_g). If B and ε can be directly measured, and a parameterization is established for Γ then it is not necessary to follow an indirect route based on Eqs. 5.3-5.5 to obtain K_ρ because $\Gamma = (B/N^2)/(\varepsilon/N^2) = K_\rho/(\varepsilon/N^2)$. This eliminates some of the uncertainties discussed above. The challenge here is to delineate governing parameters that determine Γ.

While field measurements and theoretical estimates have been presented on Γ, there is no consensus on the value of Γ or its dependence on governing parameters. The wide spread of Γ and Ri_f reported can be attributed in part to the violation of assumptions underlying Eq. 5.3 as well as the possible dependencies of Γ and Ri_f on a number of external parameters, which in turn may depend on the flow configuration. In a recent comprehensive field study on mountain terrain flows, dubbed MATERHORN (Mountainous Terrain Atmospheric Modeling and Observations Program), the authors had the opportunity to directly measure all three variables of Eq. 5.3 in the field more robustly than in previous studies (see also Wyngaard and Coté 1971). Specifically, a flow configuration resembling an idealized stratified parallel shear flow was observed lasting ~90 minutes on one evening when all instruments were operational and data passed the quality control tests. P and B were measured using ultrasonic anemometers mounted on a standard flux tower, whereas a novel 'combo' probe system (Kit et al. 2010) was used to measure TKE dissipation rate ε directly. These measurements are presented in this paper and are compared with previous laboratory observations.

Direct measurement of ε and B, and hence Γ, was a major advantage of our combo system deployment as compared to past field studies, since it allowed investigations of Γ's dependence on governing parameters in support of practical applications. To this end, the present study concerns a horizontally homogeneous, stratified parallel shear flow with approximately constant N and shear $S = \partial \overline{U} / \partial z$, and with the turbulence embedded therein characterized by a length scale l and velocity scale $\sigma = \left(\overline{u^2}\right)^{1/2}$. It is then possible to write $\Gamma = f[N, S, \sigma, l, \nu, \kappa]$, where ν is the kinematic viscosity and f a function. Since ε can be written in the same form, it is possible to replace l by ε as an independent variable, and, by the application of π theorem, it is possible to write

$$\Gamma = f[N, S, \sigma, \varepsilon, \nu, \kappa], \tag{5.7a}$$

$$\Gamma = g\left[\frac{N^2}{S^2}, \frac{\varepsilon}{N\sigma^2}, \frac{\varepsilon}{\upsilon N^2}, \frac{\upsilon}{\kappa}\right], \tag{5.7b}$$

where $Ri_g = N^2/S^2$ is the gradient Richardson number, $Fr = \varepsilon/N\sigma^2$ is a Froude number, $Re_b = \varepsilon/\upsilon N^2$ is the Gibson parameter (Fernando 1991; Gibson 1980) or buoyancy Reynolds number, $Sc = \nu/\kappa$ is the Schmidt number, and g, g_1, ... are functions. If we assume that the molecular parameters (ν, κ) are unimportant at large Re_b of the atmospheric boundary layer, Eq. 5.7b reduces to

$$\Gamma = g_1[Ri_g, Fr], \tag{5.8}$$

and dependence on at least two parameters can be identified. In general, especially in field situations, turbulence may not be locally generated, and hence (σ, ε) are considered independent. However, if the turbulence in the flow is in local equilibrium with shear (e.g. Fernando 2003), then

$$Ri_g = \frac{N^2}{S^2} \sim \frac{N^2 l^2}{\sigma^2} = Fr_l^{-2} \sim Fr^{-2}, \tag{5.9a}$$

or

$$Fr = C Ri_g^{-1/2}. \tag{5.9b}$$

where C is a constant and in equilibrium flows Fr_l is related to Fr via the relationship $\varepsilon \sim \sigma^3/l$. Note that in equilibrium shear flows the time scales of flow $(\partial \overline{U}/\partial z)^{-1}$ and turbulence (l/σ) are on the same order, and hence $\sigma/l\cdot(\partial\overline{U}/\partial z)^{-1}$ is a constant. In addition, Ri_g of the flow should ensure local production of turbulence is occurring. Combining Eqs. 5.8 and 5.9, it is possible to obtain $\Gamma = \Gamma(Ri_g)$, which is valid for stratified shear flows in local equilibrium. Eq. 5.6 becomes $K_\rho = \Gamma(Ri_g) \cdot \varepsilon/N^2$ which is of direct relevance to modeling. The local equilibrium is possible if the terms (Ⅰ), (Ⅱ), and (Ⅵ) in Eq. 5.1 are negligible, which, sans term (Ⅳ), is the basis of Osborn formulation.

During limited periods of the MATERHORN experiments, the validity of assumptions underlying Eq. 5.3 and associated mixing parameterizations could be checked in the framework of Eq. 5.9b to provide results that are useful in applications. In this paper we investigate the efficacy of Eq. 5.9 for the case of flow configurations that are perceived as in equilibrium. The measurement conditions and data processing are described in Section 5.2. Section 5.3 presents and discusses the main results, and a summary with conclusions is provided in Section 5.4.

5.2 Data Collection and Analysis

5.2.1 Measurements and processing

The first full-scale field deployment of combo probes was introduced in Section 2.4 and required overcoming onerous technical challenges. As such data acquisition was not possible for the entirety of the one-month field campaign in October 2012. Furthermore even when data acquisition was occurring, the oncoming wind direction for useful data was limited to a 120° arc due to interference of the sonic anemometer's supports (Fig. 2.8c). Notwithstanding, when conditions were right the combo system offered the advantage of collecting an in-situ calibration dataset for the hot-film probe. Occasionally in the past hot-film probes have been deployed in the field, relying on either laboratory calibrations prior to deployment (Wyngaard and Coté 1971; Skelly et al. 2002) or laborious calibrations in the field (Gulitski et al. 2007); both are stymied by sensor drift. The in-situ, neural-network based calibration procedure used for the combo probes minimizes the sensor drift as well as thermal-stratification effects as compared to past calibration procedures. A separate calibration, particularly an off-site calibration, can introduce significant uncertainties since this calibration data was collected at a different time and under different conditions as compared to the field data being measured. A time interval of 5 seconds at the end of each recorded one-minute data block was selected for aligning the hot-film probe to mean wind direction sensed by sonic anemometers, and a calibration dataset would be built from parcels of minutes where mean wind direction remained nearly constant (less than 10° change between consecutive minutes). Error estimates based on this calibration technique are not expected to exceed 1% because of the strict constraints applied to data undergoing calibration, which are similar to those applied under laboratory conditions (Kit et al. 2010).

The averaging time used for turbulence calculations was an important consideration but was bounded by one minute, the longest segments of continuous hot-film data available. The eddy turnover time was found to be on the order of the shear time scale $(\partial \overline{U}/\partial z)^{-1}$ ~ 5 seconds so only averaging times greater than this were considered to contain representative information on stratified turbulence. The internal wave time scale $2\pi N^{-1}$ was ~60 seconds, and thus the maximum possible one-minute averaging time was used. The results were checked against those obtained with 20-second averaging, and the two were generally consistent. Based on one-minute averaging period, various turbulence quantities were calculated and are reported on in next section. The buoyancy flux magnitude (B) was calculated from the sonic anemometer data (accuracy ±15%), the rms velocity (σ) from both sonic anemometer and hot-film probe (which agreed within 5%), and the TKE production (P) based on the mean velocity gradients from tower sonic anemometers (4 m and 10 m) and Reynolds stresses from the 6-m sonic anemometer. The vertical temperature gradients for the calculation of N^2 were determined using thermocouples at 5 m and 7 m. Calculations of ε are discussed in next subsection.

While a month of semi-continuous data collection was attempted, careful combing of data by Kit et al. (2017) showed that only a few hours of data could be considered as belonging to the stratified parallel shear flow category. The nocturnal flow data were even more limited. A nocturnal period with several segments of data and relatively steady wind speed and direction (see Fig. 5.1) was used by Kit et al. (2017) in their analysis of high-frequency intermittent bursts, and we opted to use the same period for this study. This period lasted from approximately 10:00 PM to 11:30 PM Local Time (LT) on 19 October, 2012, wherein the near-surface boundary layer transitioned from relatively strong stability ($Ri_g > 1$) to weak stability ($Ri_g \sim 0.25$). For this period, time series of calibrated 3D wind velocity measurements were obtained, and two data segments in particular were selected during which turbulence characteristics remained relatively stationary and devoid of transitioning flow. We denote these segments (symbol: Σ), which will make up the bulk of the analysis, based on the degree of stable stratification during each segment; subscript (s) was used to denote strongly stratified periods and (w) for weakly stratified. The first segment, Σ_s, covered three minutes of very stable ($Ri_g \geq 1$), what appeared to be near-laminar, conditions. Twenty minutes of the second segment, Σ_w, were characterized by weakly stratified (oscillating) turbulence with much lower Ri_g (≤ 0.4 excluding one of the minutes). The comparison of Σ_s and Σ_w allowed evaluation of turbulence under different degrees of stability. The evolution of stable boundary layer for the entire 90-minute period containing these segments of hot-film data is discussed in next section (Section 5.3).

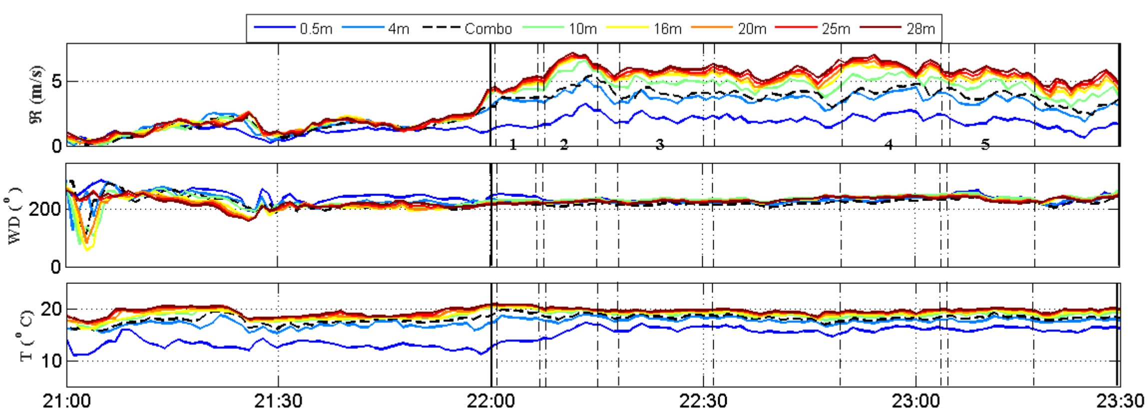

Figure 5.1: Time series of multi-level tower measurements are directly taken from Kit et al. (2017). They show from 22:00 to 23:30 Local Time when a stratified parallel shear flow was observed: wind speed (top), wind direction (WD; middle), and temperature (T; bottom) measurements. The vertical dashed-dotted lines and numbers on horizontal axes in top panel are related to the analysis periods used by Kit et al. (2017) and are not directly relevant to the current work. See Figure 5.2 for analysis periods used in this work.

5.2.2 Dissipation estimation

By far the most common technique to estimate the dissipation rate is based on the local isotropy hypothesis, from which it follows that

$$\varepsilon = 3\upsilon\left[\overline{\left(\frac{\partial u}{\partial x}\right)^2} + \overline{\left(\frac{\partial v}{\partial x}\right)^2} + \overline{\left(\frac{\partial w}{\partial x}\right)^2}\right] = 15\nu\,\overline{\left(\frac{\partial u}{\partial x}\right)^2}, \tag{5.10}$$

where $\partial()/\partial x$ is the instantaneous spatial derivative of a velocity component. The last term follows from $\overline{(\partial v/\partial x)^2} = \overline{(\partial w/\partial x)^2} = 2 * \overline{(\partial u/\partial x)^2}$ for isotropic turbulence. Taylor's 'frozen turbulence' hypothesis is commonly applied to convert from the measured $\partial()/\partial t$ at single point to the spatial derivative in Eq. 5.10 (Wyngaard and Coté 1971). In the present work, the stream-wise gradients of transverse and lateral velocity components (v and w) were also measured so that the local isotropy assumption could be approximately checked. This estimation technique requires robust measurements of velocity gradients at the finest, dissipative (~ 1 mm) scales. Precise measurements at these scales may not have been completely achieved by the utilized double-X hot-film probe configuration, which covered a volume with a maximum dimension of ~7 mm. Therefore additional checks were done to better quantify any possible biases associated with potential measurement limitations.

Another technique to estimate ε is based on the Kolmogorov inertial subrange of the one-dimensional velocity spectra (Kaimal and Finnigan 1994)

$$E_{11}(k_1) = \alpha_{1k}\varepsilon^{2/3}k_1^{-5/3}, \tag{5.11}$$

where α_{1k} is the 'universal' Kolmogorov constant and k_1 is the longitudinal wave number. With Taylor's hypothesis and rearrangement Eq. 5.11 becomes

$$\varepsilon = \frac{2\pi}{U}\left[\frac{E_{11}(f)_{in}(f)_{in}^{5/3}}{\alpha_{1k}}\right]^{3/2}, \tag{5.12}$$

where $E_{11}(f)_{in}$ and the signal frequency f_{in} span only the assumed intermediate frequencies of the inertial subrange. This technique depends on the assumed value for α_{1k}, which has reported values ranging between 0.45 and 0.6 (Kaimal and Finnigan 1994; Elsner and Elsner 1996), and hence uncertainty for ε can be as high as 50%. Also, as pointed out by Kit et al. (2017), if there is small-scale turbulence production such as 'bursts,' then Eq. 5.12 does not represent the actual dissipation. Eq. 5.12, however, has the advantage of only relying on the precision of probe's measurements at the intermediate wave numbers (frequencies) of the inertial subrange and has been utilized with some success in hot-wire anemometry (Azad and Kassab 1989) and in (limited-resolution) sonic anemometry (Grachev et al. 2015; Lozovatsky and Fernando 2012). In this work, we have calculated dissipation directly using Eq. 5.10, which is the best direct method for obtaining ε.

Quality checks were conducted on estimated ε. For example, for the 20-minute low-Ri_g data segment (Σ_w) the averaged ε was 0.005 m^2 s^{-3} which corresponded to α_{1k}= 0.59. This calculation assumed an inertial subrange from 5 Hz to 50 Hz based on the inspection of spectra. The estimated α_{1k} values showed little sensitivity (<2%) to adjustments of the lower cut-off from 1 to 10 Hz. The 50 Hz upper cut-off frequency was selected to be just below the frequency of Taylor microscale $\lambda = (15\nu\sigma^2/\varepsilon)^{1/2}$ (the average value was ~60 Hz in frequency space), where viscous effects may first become important (Long 1982). The estimated value for α_{1k} (0.59) was close to the upper end of range from past atmospheric measurements (Williams and Paulson 1977), though it is smaller than some previous estimates (Gibson et al. 1970; Sheih et al. 1971) and consistent with the recent high-Re direct numerical simulations of Ishihara et al. (2016; personal communication). While estimation of ε for Σ_w is reasonable, the method is expected to have some limitations due to overall probe size (~ 7 mm), that may lead to attenuation at the highest frequencies used in dissipation estimation by Eq. 5.10.

During Σ_s, the Ozmidov to Kolmogorov scale ratio, the Gibson parameter $\varepsilon/(\nu N^2)$, had values on the order 10^3, and therefore, according to (Gargett et al. 1984), local isotropy assumption is also expected to be applicable for this data segment. The small-scale gradients of different velocity components for Σ_s, however, indicated that the approximate relationship for local isotropy, $\overline{(\partial v/\partial x)^2} \approx \overline{(\partial w/\partial x)^2} \approx 2 * \overline{(\partial u/\partial x)^2}$, was not satisfied. In order to minimize uncertainties so introduced by non-isotropy, all three velocity components were employed for calculation of ε (the first identity of Eq. 5.10) though this form still assumes isotropy at local scales for appropriate velocity derivatives in y and z directions. For Σ_w the isotropy relationships were well satisfied, but all three components were used in final estimation of ε for consistency, though this tended to have very little effect on the final result.

5.3 Results and Discussion

5.3.1 Flow evolution

As mentioned, at 22:00-23:30 LT on 19 October, 2012, the flow resembled a stably (temperature) stratified parallel shear flow, with winds having the same direction with height and both velocity and temperature increasing away from the ground (Fig. 5.1). Figure 5.2 provides additional details of the flow variables during this period. These include: the Reynolds number based on Taylor microscale λ and σ (Re_λ; Fig. 5.2a), Gibson parameter (Re_b; Fig. 5.2b), Reynolds stresses (Fig. 5.2c), TKE dissipation rate (Fig. 5.2d), vertical temperature flux (Fig. 5.2e), vertical gradient-based quantities of N^2 and S^2 (Fig. 5.2f), TKE and mean velocity (Fig. 5.2g), and gradient Richardson number Ri_g and Froude number Fr (Fig. 5.2h). After careful inspection, the overall analysis period was divided (somewhat subjectively) into periods of evolving turbulence and non-evolving (quasi-stationary, including oscillatory) turbulence; the latter are highlighted in yellow and were subjected to further analysis. Note that not all quantities have data covering the entire period (Figs. 5.2a-b,d,h), which is due to non-compliance of criteria for obtaining reliably calibrated hot-film measurements (mainly near-constant wind direction and relatively low variations of mean and rms velocities). Periods that lacked full data coverage were excluded from the analysis. Some interesting observations on the flow evolution are given below.

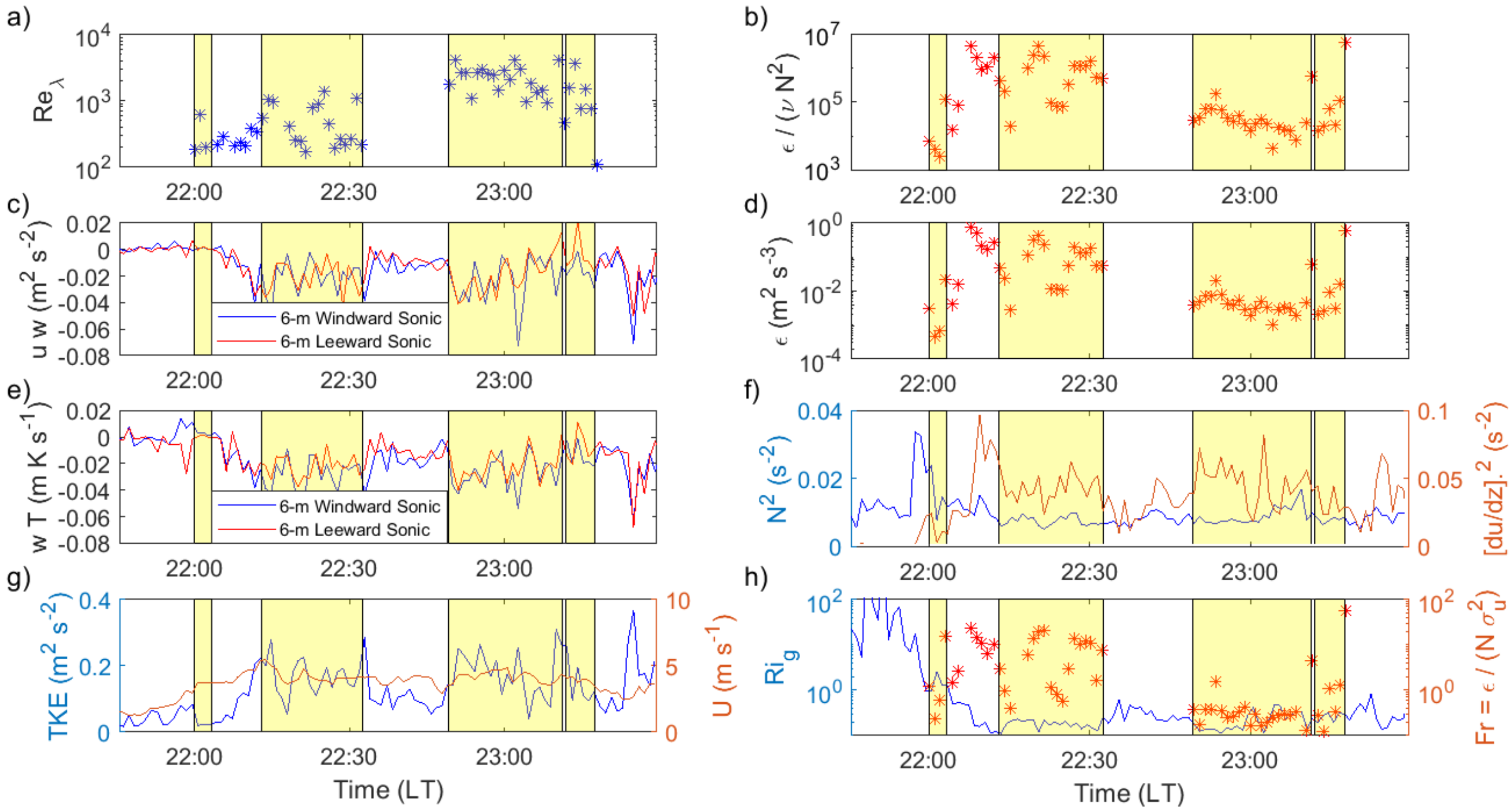

Figure 5.2: Combo probe measurements at 6-m level on the evening of 19 October, 2012: (a) Reynolds number based on Taylor microscale $Re_\lambda = (\lambda\sigma)/\nu$, (b) Gibson parameter Re_b, (c) Reynolds stress $\overline{u'w'}$, (d) dissipation rate ε, e) kinematic heat flux $\overline{w'T'}$, (f) tower-based gradient measurements of Brunt-Väisälä frequency N^2 (blue) and vertical shear squared $(\partial U/\partial z)^2$ (red), (g) TKE (blue) and mean wind speed U (red), and (h) gradient Richardson number Ri_g (blue) and turbulent Froude number Fr (red). The yellow-shaded areas are four periods **A**, **B**, **C**, and **D** identified as non-evolving and nominally quasi-stationary for some or all variables and for which all measurements were available. **A** is in the regime Σ_s, and **C** in Σ_w. Less data points are shown in (a), (b), (d), and (h) because of the lack of ε measurements due to failure of the data in quality control tests for calibration. Two sets of measurements in (c) and (e) are from sonic anemometers at 6-m level separated several meters horizontally.

The 15 minutes prior to 22:00 LT displayed a clear transition from virtually shear-free, near-laminar flow to developing turbulence. $\overline{U}$ and TKE gradually increased (Fig. 5.2g), and in the 5 minutes immediately before 22:00 there was a large increase of N^2 and S^2 (Fig. 5.2f). This was followed by a three minute period (identified as **A**) of near-constant $\overline{U}$, TKE, Ri_g, and turbulent fluxes (Fig. 5.2c,e-h). The shear S and N^2 were lower during this period compared to few preceding minutes, when Ri_g was higher but decreasing and the production of TKE was increasing. Overall, **A** was recognized as a nominally quasi-stationary period of low TKE with Ri_g hovering right above a value of 1.0. **A** is the same period as the relatively high-Ri_g regime Σ_s described in the preceding section, which will be analyzed further in the next two subsections. It should be noted that some quantities in **A** are still varying, and additional tests are needed to ensure stationarity.

After **A**, a 10-minute period of clearly evolving turbulence resumed with TKE (among other quantities) rising significantly. At ~22:13, TKE approximately peaked (Fig. 5.2g), and Ri_g stabilized around ~ 0.2 (Fig. 5.2h). For the next 20 minutes (identified as **B**) conditions were considered as nominally quasi-stationary for some variables. TKE, Ri_g, and fluxes (Figs. 5.2c,e-g) oscillated slowly about some fixed values, signifying the traits of stratified turbulence. Not all variables could be considered quasi-stationary; ε and related quantities like the Gibson parameter (Fig. 5.2b) fluctuated significantly in magnitude during this period suggesting that the flow may still be developing and not yet truly stationary. After **B**, there was a 15-20 minute period characterized by relatively lower TKE and higher Ri_g (~0.3-0.4), but unfortunately calibrated hot-film data are not available for this period (due to not passing the quality checks).

The next 20 minutes of data from approximately 22:50 to 23:10 (identified as **C** in Figure 5.2 and identical to Σ_w introduced above) were valuable as an extended quasi-stationary period where TKE was relatively high, $Ri_g \approx 0.1\text{-}0.3$, $Re_b \sim 10^4\text{-}10^5$, $Re_\lambda > 10^3$, and ε remained relatively constant but less than in preceding ~45 minutes. The increase of Ri_g around 23:00 was accompanied by a reduction in TKE showing that turbulent transport had been momentarily impeded. In the absence of significant mixing, the vertical shear S increased in the next couple minutes prompting a drop in Ri_g, setting off instabilities, and peaking TKE. The variables then cycled again to increase Ri_g (~0.2-0.4). The TKE is relatively low for the latter part of **C** until another drop of Ri_g and a TKE maximum in the final 1-2 minutes (Figs. 5.2g-h).

For about one minute after the conclusion of **C**, rapid variations of some parameters continue, most notably ε (Fig. 5.2d) by more than one order of magnitude (this was a case of turbulent bursting identified by Kit et al. 2017). Therefore this minute was excluded from consideration. TKE settled during the next 5 minutes (identified as **D**) to relatively constant values along with other parameters. Immediately following **D**, there was again a large jump in ε, and a flow transition began with wind directions slowly changing, which also meant that hot-film data were no longer available. At 23:30 the wind direction and speed changed dramatically (not pictured). After this transition, sizable segments of hot-film data could not be calibrated due to fluctuating wind directions and general nonstationary behavior.

5.3.2 Energy spectra

Two representative spectra for the high-Ri_g Σ_s (**A** from Figure 5.2; 3-minute average Ri_g=1.4) and the low-Ri_g Σ_w (**C** from Figure 5.2; 20-minute average Ri_g=0.2) are shown in Figures 5.3a and 5.3b, respectively. The Σ_w case (Fig. 5.3b) has a wider Kolmogorov (-5/3) subrange from k_1 = 2-4 m^{-1} to 100-200 m^{-1}, with a clear departure from $k_1^{-5/3}$ occurring at the lower end of this range for w-component. As discussed below, this departure can be attributed to anisotropy of stratified turbulence rather than to the blocking of eddies by the ground. A similar trend was evident in Σ_s (Fig. 5.3a) with anisotropy in w occurring at higher wave numbers such that the departure occurred at much smaller scales (<1 m) and thus shrunk the $k_1^{-5/3}$ subrange. An interesting observation for Σ_w was the continuance of horizontal spectra along -5/3 slope for about half a decade below k_1 ~ 3 m^{-1} until the vertical spectra began to deviate from $k_1^{-5/3}$.

The above observations are consistent with fundamental concepts of stratified turbulence. As pointed out by Riley and Lindborg (2008), the anisotropy sets in at scales larger than the Ozmidov scale $L_o = (\varepsilon/N^3)^{1/2}$, which can be shown to be proportional to the vertical scale $L_v = \sigma_w/N$, where σ_w is the vertical rms velocity, i.e. $L_o \sim L_v$. On the other hand, when stratification effects are strong, the horizontal scale L_h of turbulence can be much larger ($L_h > L_v$), and there can be a cascade of energy via breakdown of horizontal motions. Riley and Lindborg (2008) argued that larger anisotropic motions are limited by $L_b = \sigma/N$, and layers of horizontal motions appear with shear σ / L_b across them. Ensuing shear or 'zig-zag' instabilities at scale L_b are responsible for cascading along horizontal scales up to $L_o \sim L_v$ beyond which regular 3D Kolmogorov cascading resumes. Such vertically limited and horizontally growing turbulence is evident in the laboratory experiments of De Silva and Fernando (1998) and Maderich et al. (2001).

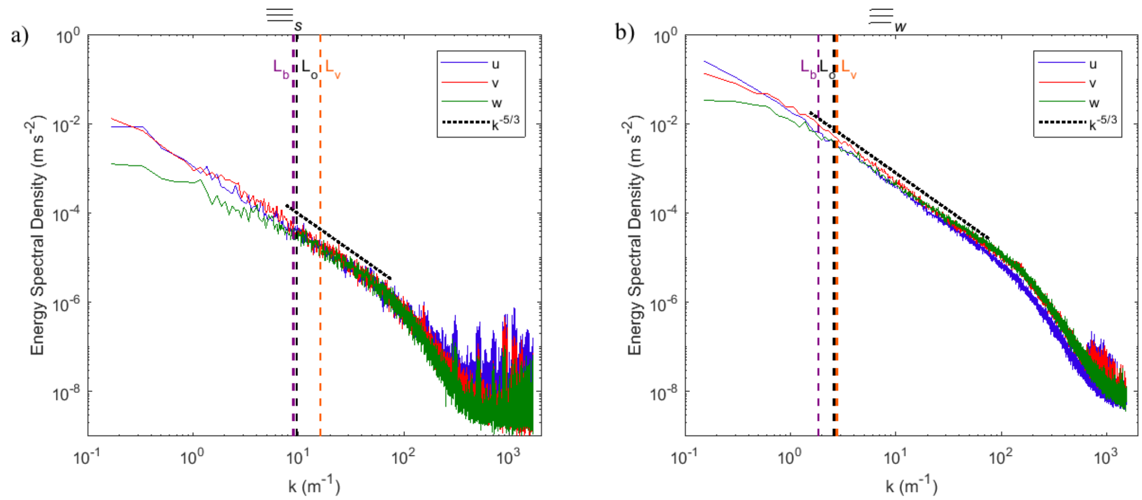

Figure 5.3: One-dimensional TKE spectra for velocity components (u, v, and w) from the two data segments constructed by ensemble-averaging 10-second data increments: (a) the three-minute Σ_s and (b) the 20-minute Σ_w. A -5/3 slope (dotted) line plotted along a portion of the inertial subrange helps to depict the departure from Kolmogorov theory. Canonical length scales for stratified turbulence are indicated by vertical (dashed) lines. The noisier appearance of data in (a) relates to the fewer 10-second data segments (18) available to build ensemble-averaged spectra. Note that above 300 to 600 m^{-1} the data becomes contaminated by noise which is expected based on total probe volume spanning ~5-10 mm.

For comparison, the length scales L_b, L_o, and L_v are shown in Figure 3. In the more weakly stratified regime Σ_w (Fig. 5.3b), the departure from isotropy occurs close to $L_v \approx 0.98L_o$. Below this wave number, the vertical spectra begins to flatten out, while, as discussed, the horizontal spectra continue along the -5/3 slope as postulated by Riley and Lindborg (2008) until slightly beyond the scale L_b or so, above which cascading of horizontal motions becomes untenable. On the other hand, for Σ_s, L_v is relatively smaller than other scales ($L_v \approx 0.62L_o$) due to strong anisotropy, whereas $L_b \approx 1.07L_o$. Hence horizontal cascade may not be tenable and all three components depart from $k_1^{-5/3}$starting from $L_o \approx L_b$, though w departs more substantially due to anisotropy and/or geometry of 6-m measuring height (see below).

Other notable differences between Σ_s and Σ_w are evident in Figure 5.3. For Σ_s the energy density, particularly at large scales, was approximately an order of magnitude smaller than in Σ_w, which reflects the contrasting conditions between the cases. The TKE contained by vertical component at energy-injecting scales (low k_1) was visibly smaller relative to horizontal components in Σ_s (Fig. 5.3a) as compared to Σ_w (Fig. 5.3b), which is a result of stronger stratification. Note that the closeness to the ground also imposes a dynamical constraint on turbulent motions, in that the vertical motions are blocked and the integral scales based on w-component are approximately the height above the ground. This causes the anisotropy for vertical motions to set in at a wave number $2\pi/6$ ~ 1 m^{-1}. In both Figures 5.3a and 5.3b, the anisotropy sets in at scales before this, closer to L_o and hence is expected to be primarily a result of stratification.

Finally, a comparison of the dissipative regions (highest wave numbers > 100 m^{-1}) of the two cases in Figure 5.3 reveals varying degrees of isotropy, which were discussed earlier as it pertained to dissipation estimation (Section 5.2.2). In Σ_s there is no clear distinction between different components at high wave numbers due in part to noisiness of compiled data which utilized less ensemble-averaged increments. On the other hand, in Σ_w the v- and w-components are approximately a factor of 2 times greater than the u-component, which is the proper relationship for isotropic turbulence. Such idealized behavior gave additional confidence in the estimate of dissipation rate and subsequently the mixing coefficient Γ from some of data points in Σ_w.

5.3.3 Turbulent kinetic energy budget

Since Eq. 5.3 is not expected to be exactly satisfied in real field measurements, it can be rewritten in terms of a Residual R as

$$R = P - B - \varepsilon, \tag{5.13a}$$

$$R = \frac{\partial \overline{q^2}/2}{\partial t} + \overline{U}\frac{\partial \overline{q^2}/2}{\partial x} + \frac{\partial}{\partial z}\left(\frac{\overline{q^2 w}}{2} + \frac{1}{\rho}\overline{pw}\right) + Er, \tag{5.13b}$$

where R in Eq. 5.13a is principally composed of the terms on right-hand side of Eq. 5.13b (see also Eq. 5.1), which include nonstationarity, advection of TKE by mean flow, energy flux divergence, and the cumulative measurement errors Er. For Osborn model, R is set to zero, and thus it is useful to investigate the role of the four terms in Eq. 5.13b that potentially violate the assumptions of Osborn (1980). The two cases of Σ_s and Σ_w are shown in Figure 5.4, where P, B, and ε were directly measured and R was enumerated. In the high-Ri_g Σ_s, R was approximately equal to ε whereas P and B were comparably small due to the highly evolving nature of the flow. As evident from Figures 5.2g-h, the flow is highly nonstationary surrounding Σ_s, with Ri_g as high as 100 preceding this period, which may explain the anomalous energy budget particularly at 22:00 LT. The persistent ε and matching R during a period of small buoyancy flux and shear production may indicate that Σ_s was a period of strongly stratified turbulence dominated by factors neglected in Osborn model. Nonstationarity could be a factor, but the paucity of data in Σ_s precludes further inferences on the terms in R that are most dominant.

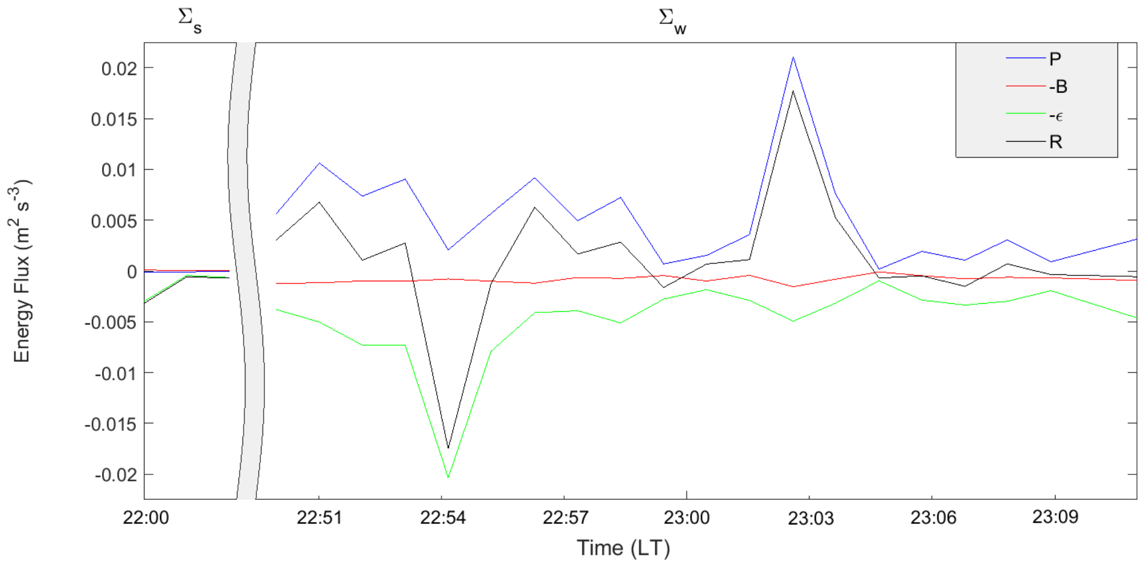

Figure 5.4: Terms of simplified TKE budget (Eq. 5.3) based on one-minute averaging period are plotted along with Residual R. The three minutes of Σ_s are displayed to the left, which are followed by a break in the horizontal time axis, and then the twenty minutes of Σ_w are plotted. B and ε are multiplied by -1 as they appear in the equation.

For clarity, the conspicuously nonstationary period after **A** and the subsequent segment **B**, which had strongly fluctuating ε (Fig. 5.2d), are not shown in Figure 5.4, but the energy budget during Σ_w (**C**) is shown, for which all terms generally have larger magnitudes than during Σ_s. This period starts with a nominally stationary period from 22:50-22:53 LT, where R was small but positive. There was a sudden change at 22:54 LT with large ε, which was followed by a seven-minute quasi-stationary period 22:55-23:02 LT with small R values. Around 23:03 LT, a strong shear production (P) event dominated other terms, causing large R values. A six-minute quasi-stationary period from 22:05 LT onward concluded Σ_w, during which R was very small and fluctuated around zero.

While small R implies that conditions for Osborn formulation are more likely satisfied, it does not guarantee homogeneous and stationary turbulent flow over relatively longer period, and thus an additional constraint was imposed in selecting the data for inferring flux relationships. This constraint was that turbulence and mean shear were in equilibrium as in Eq. 5.9b. In order to estimate the coefficient C of Eq. 5.9b, the period 23:05-23:11 LT was selected, during which R remained consistently small and thus could potentially be considered as the most stationary and homogeneous of all available periods. The average C for this period was $C \approx 0.15 \pm 0.05$, with the spread based on the standard deviation. A band of data points was selected satisfying this criterion, and all selected data points had relatively small R. For example, the selected data included those from the range 23:06-23:08 LT (average $R = -4\times10^{-4}$) as well as data points in the quasi-stationary periods of ~22:50-22:53 and ~22:55-23:02 LT. The following subsection presents and discusses the results from this careful selection based on energy budget, with the selected data shown in Figures 5.5 and 5.6b. Only the data within this band in Figure 5.5 was considered to potentially follow $\Gamma = \Gamma(Ri_g)$ for Section 3.4. Nine of the final ten data points were from Σ_w (**C**) and one from **D**.

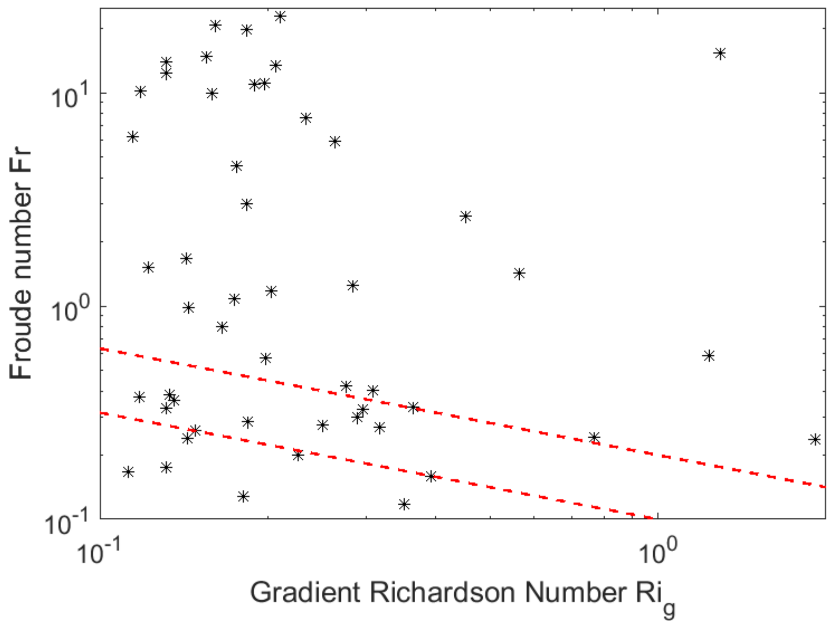

Figure 5.5: Gradient Richardson number Ri_g versus Froude number Fr comparison for all data points. The bounds of Ri_g-Fr relationship used to select data points by criterion (Eq. 5.9b) are shown by dashed red lines, that is $Fr = CRi_g^{-1/2}$, where C = 0.15±0.05.

The Residual term R is worth further discussion given its importance in our determination of final results. Of the four terms in Eq. 5.13b, only the first can be directly evaluated in principal using time series data from sonic, though the time discontinuities every minute for hot-film realignment make this estimation somewhat problematic. During Σ_w we roughly estimated the temporal derivative contribution at 20-second resolution to be on the order of 10^{-3} to 10^{-5} m^2 s^{-3}. For the energy flux divergence term, the third moments $\overline{q^2w}$ were measurable at multiple levels by sonic anemometers so its contribution to TKE budget could be estimated. The average value for this third-order divergence term during Σ_w was 2×10^{-4} m^2 s^{-3} and could occasionally reach values on order 10^{-3}, but there was no correlation of these values with R so they could not be considered the dominant term, just adding to the cumulative effect of Eq. 5.13b. The pressure transport portion of flux divergence was not directly measured, and its behavior under stable conditions is not widely known.

The final term Er in Eq. 5.13b contains the cumulative measurement-related errors and limitations. It could include contributions from unresolved turbulent fluctuations, for example the buoyancy flux at higher wave numbers not resolved by sonic anemometer. Note that buoyancy fluctuations were measured at 32 Hz and therefore at a lower spatial and temporal resolution than velocity fluctuations from the hot film that were measured at 2 kHz. This limitation may affect the measured B by an estimated 10-15% but cannot be quantified until future experiments with fine-scale temperature probes. Systematic calibration errors for hot-film probe have been cited as 0.5% in a past study using standard calibration techniques, which can contribute an estimated 15% error in ε (Kit et al. 1997). Overall, the relatively large values of R that occasionally occurred seem connected with effects of nonstationarity and horizontal inhomogeneity of the local TKE budget, the latter of which is anticipated to be especially significant for complex terrain. While the large negative R in the fifth minute of Σ_w could have other origins (Kit et al. 2017), the combined evidence from Figures 5.2 and 5.4 shows that the nonstationary and inhomogeneous nature of natural flows has serious implications for simplified TKE budget assumed in models (Elsner and Elsner 1996; Osborn 1980), even for the nominally idealized stratified shear flows selected for analysis here.

5.3.4 Mixing coefficient Γ

As discussed, a major quantity of interest for turbulent mixing is K_ρ, which, when normalized, is the same as the mixing coefficient Γ, that is $K_\rho/(\varepsilon N^{-2}) = B/\varepsilon = \Gamma$, and hence the discussion here will be on Γ. It was argued that Γ is dependent on multiple parameters (Eq. 5.7), which are onerous to delineate using field data in particular. It was also argued that Γ can be considered as a function of Ri_g only when turbulence is in equilibrium with mean shear, and that equilibrium state can be diagnosed using a Fr-Ri_g relationship (Eq. 5.9). Mixing coefficients so evaluated can be compared with those obtained from controlled laboratory experiments, such as Strang and Fernando (2001), conducted under idealized stationary and horizontally homogeneous conditions. Figure 5.6a shows all Γ data, 54 data points in total, as a function of Ri_g, and it clearly indicates that Ri_g is not the only governing parameter. However, data points that did satisfy the equilibrium criteria described in the preceding subsection are displayed in Figure 5.6b. Also plotted on Figures 5.6a-b are the fitted (or bin-averaged) laboratory results of Strang and Fernando (2001). A good correspondence can be seen between laboratory data and the 10 equilibrium-satisfying field data points for a limited range of Ri_g. Our data suggested $\Gamma \approx Ri_g^{0.4}$ for $0.1<Ri_g<0.3$, a slightly different relationship than the empirical $\Gamma(Ri_g)$ model of Mellor and Yamada (1974), which is also plotted in Figure 5.6. All data in Figures 5.4-5.6 are given in Table A.2 with asterisks marking rows of data deemed to satisfy equilibrium shear flow conditions and thus are appearing in Figure 5.6b.

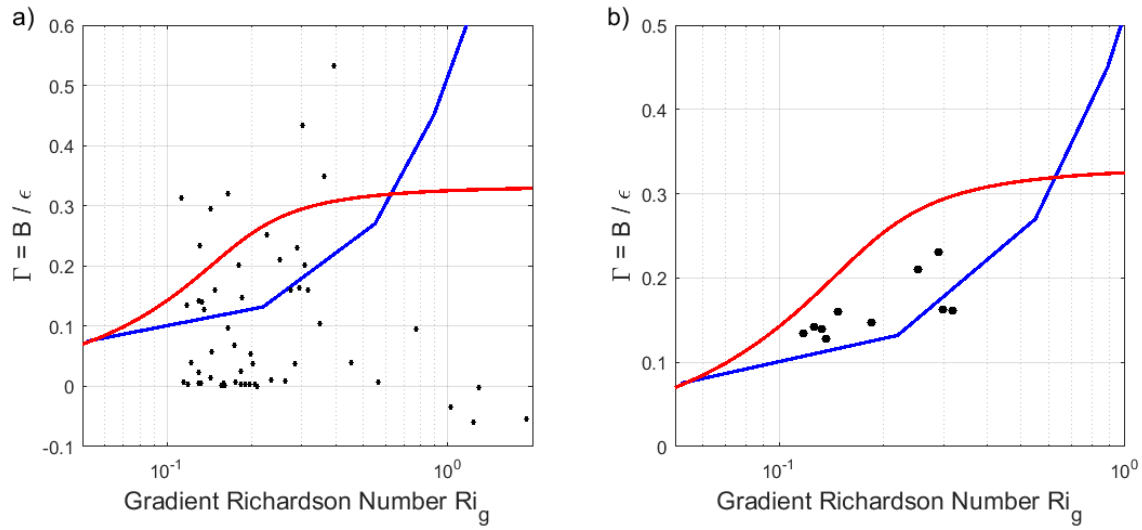

Figure 5.6: Gradient Richardson number Ri_g versus mixing coefficient Γ for combo data recorded on evening of 19 October, 2012, including (a) all data points and (b) select data points that demonstrated $Fr = CRi_g^{-1/2}$ relationship as defined in Figure 5.5 and Section 5.3.3. Blue line is approximate trend found in laboratory measurements of Strang and Fernando (2001). Red line is the empirical relationship postulated by Mellor and Yamada (1974) and widely used in geophysical modeling applications.

5.4 Summary and Conclusions

Fine-scale turbulence measurements were made using a novel combo probe during the MATERHORN Program's fall 2012 campaign, which in addition featured measurements of complex terrain flows across a swath of spatiotemporal scales (Fernando and Pardyjak 2013; Fernando et al. 2015). The combo system automatically rotated the 3D hot-film probe into mean wind direction sensed by the co-located sonic anemometer, allowing opportune positioning of the hot-film probe during a ~90 minute period of stratified parallel shear flow, which was identified via wind and temperature profiles measured from the densely instrumented (flux) tower that housed the combo probe (Fig. 2.8 and Kit et al. 2017). The dataset collected during this period was used in this thesis for fundamental turbulent mixing studies. Within several subintervals of nominally stationary flow, important mixing parameters, the mixing coefficient Γ and the flux Richardson number Ri_f (mixing efficiency), were calculated. In oceanographic studies, the Osborn (1980) model is used to evaluate the buoyancy flux, and this model assumes Γ ~ 0.2 or $Ri_f \sim 0.15$ for conditions satisfying stationarity, horizontal homogeneity, and negligible (volume-averaged) energy flux divergence. These assumptions imply that the TKE production rate P, the magnitude of the buoyancy flux B, and the rate of dissipation of TKE ε are in balance with zero residual terms, i.e., $R = P - B - \varepsilon \approx 0$.

In the present work, the assumptions of the of the Osborn model for the case of an atmospheric stratified shear flow were investigated using direct measurements of P, B, and ε. The balance ($P - B - \varepsilon = 0$) was not satisfied in general, even for nominally stationary flows, but there were some periods, both short and long, where $R \approx 0$. It was argued that when $R \approx 0$ the turbulence in the flow could be in equilibrium with shear, which was ascertained using an additional test. During equilibrium conditions, Γ and Ri_f are function of the gradient Richardson number Ri_g alone, under which conditions the relationship $Fr = CRi_g^{-1/2}$ must be satisfied. Using data from the longest available $R \approx 0$ segment, C was evaluated as $C = 0.15 \pm 0.05$. About 10% of minutes the 90-minute period satisfied the equilibrium shear flow constraint, and for these data points the calculated Γ and Ri_f were in good agreement with the results of controlled laboratory experiments on stationary stratified shear flows. Our field data, however, spanned only a limited parameter range ($0.1 \le Ri_g \le 0.3$).

To conclude, the present study of atmospheric stratified shear flows has shown that (i) the mixing parameters Γ and Ri_f in the field depend on multiple parameters, (ii) there are special conditions under which mixing parameters are a function solely of Ri_g, (iii) data satisfying conditions in (ii) can be satisfactorily compared with controlled laboratory experiments having similar flow configurations, and (iv) the usage of field data-based mixing parameters and parametrizations for environmental flow models should be done with caution as they may depend on multiple governing parameters determined by the flow configuration and operating conditions, with mixing coefficient varying from near zero (or even negative for restratification) to about 0.5 in the present study.

CHAPTER 6:

CONCLUSIONS

Carefully planned field observations over equatorial oceans help delineate multi-scale meteorological processes with far-reaching implications for global weather and climate research. In turn these observations assist development of seamless models that can accurately simulate key phenomena involving a multitude of spatiotemporal scales. Large experimental datasets collected during TOGA COARE and CINDY2011/DYNAMO as well as expanding networks of satellite and autonomous ocean sensors, have made such studies of scale interactions possible although integrative, across-the-scales analyses remain rare. In this thesis, the scale continuum of vertical exchanges has been partly addressed (i.e., intraseasonal scales and below) in the context of ASIRI-RAWI project conducted by University of Notre Dame researchers, including the author, and international research partners. This investigation has also taken advantage of access to largescale datasets (e.g., reanalysis) and a unique fine-scale turbulence dataset from MATERHORN to parse information covering a larger range of scales. Research findings of this thesis have demonstrated the roles of shear instabilities and convective motions as mechanisms of vertical exchange within the equatorial Indian Ocean (IO) region atmosphere from lower stratosphere to atmospheric boundary layer (ABL). These findings are summarized below.

Measurements across a range scales during ASIRI-RAWI captured a series of interacting phenomena between the lower stratosphere and surface layer of ABL that have not been described together previously. A striking observation was the presence, at ~13 to 20 km in altitude, of equatorial planetary Kelvin waves from all three sites, which could be confirmed by the reanalysis datasets. These waves belong to the family of equatorial intraseasonal oscillations and were found to play important roles in vertical exchange of properties through a series of interacting smaller-scale phenomena. The Kelvin waves caused variability with the same quasi-biweekly period (~16 days) in tropical tropopause layer (TTL), dubbed 'tropopause jumps,' as well as occurrences of westerlies throughout vertical profile of troposphere, particularly at surface, i.e., westerly wind bursts (WWBs). In TTL, the 'jumps' were related to shear (Kelvin-Helmholtz) instabilities which appeared due to a combination of background and wave shear. These instabilities appear to cause vertical mixing of atmospheric constituents, including irreversible mixing, as has been found in earlier studies in eastern IO (Fujiwara et al. 2003), but this is the first time that these instabilities were observed in western IO, suggesting a more widespread link between Kelvin waves and vertical stratosphere-troposphere exchange processes. It was unclear to what extent these TTL instabilities were influencing the lower layers, but they unequivocally confirmed the presence of Kelvin waves in, above, and below TTL during February 2015.

The Kelvin waves were of baroclinic nature and thus propagated vertically down to the upper troposphere, to altitudes as low as ~12-13 km. High geopotential anomalies in-phase with westerly wind anomalies of Kelvin waves interacted with low geopotential (pressure) phase of smaller-scale disturbances in the mid-troposphere and below to trigger a strong vertical pressure gradient anomaly. This anomaly led to strong updrafts and downdrafts in the troposphere, and surface instrumentation deployed in this study captured patterns of moist convection and surface fluxes that resembled convectively-coupled waves. These results indicated that the pressure gradient anomaly may have initiated and intensified westward-propagating convectively-coupled waves. The strong westerlies arriving first at surface may have been partly a phase propagation of such a mid-tropospheric wave, but their strengthening across entire troposphere was caused by rapid turbulent transport processes associated with lower-atmospheric up/downdrafts (similar to thermal convection but now mainly driven by the vertical pressure gradients). Turbulence and entrainment from the up/downdrafts promoted vertical mixing of westerly momentum from upper-tropospheric Kelvin wave and the westward-moving mid-tropospheric disturbance throughout the troposphere in localized area of western IO. While convective motions on large scales may be partly related to buoyancy or moisture-driven convection, the pressure gradient is hypothesized to be the major driver of convection in our case, which is generally consistent with conclusions of Powell and Houze (2015) and Sakaeda and Roundy (2016)

To our knowledge, this was the first set of detailed observations on the coupling of stratospheric/upper-tropospheric anomalies of Kelvin waves with surface layer anomalies, which indicated that dry Kelvin waves may have significant impacts on convection and air-sea interactions in the equatorial region. The estimated region of meridional influence was 1100 km (Rossby radius; see Figure 3.16) and the longitudinal scale of a localized wind burst was ~300-600 km.

Given the significant surface flux modulations observed Seychelles coastal observational site, particularly of westerly momentum, a one-dimensional ocean mixed layer model was utilized to evaluate potential impacts on ocean surface layer. Idealized case study of WWBs showed that the response of (modeled) ocean mixed layer was highly dependent on initial conditions, and were on order of ~ 0.2-1°C for sea surface tempearture cooling and ~ 5 m for mixed layer deepening.

Stably stratified shear flows are a pervasive flow configuration in many oceanic, atmospheric, and engineering applications. In the context of ABL above the equatorial oceans, stable stratification may occur within cold pools created by downdrafts during periods of deep convection, but other environmental examples abound from sheared oceanic thermocline of equatorial undercurrent to the nighttime SBL over cool land surfaces. A study of this generalizable flow configuration was warranted, and measurements from hot-film combo probe deployed as part of MATERHORN's technology development initiative served this purpose, capturing stably stratified parallel shear flow in nocturnal SBL over complex terrain (Kit et al. 2017). The hot-film probes could resolve the finest (Kolmogorov) scales of turbulence, not available from ASIRI-RAWI instrumentation, and allowed for fundamental turbulent mixing studies. Mixing parameters Γ and Ri_f were calculated and varied significantly (2-3 orders of magnitude; see Table A.2) with multiple flow parameters, even within the nominally stationary turbulence of 90-minute period analyzed. A criterion was proposed for determining when mean shear flow was in equilibrium with turbulence, and this method proved robust at identifying data points that varied with single flow parameter (gradient Richardson number Ri_g), as in the case of laboratory studies of similar flow configurations. Still the large variability observed for the majority of period (90%) suggested that mixing parameterizations for environmental flow models should be carefully developed when using field measurements and that mixing may even be treated as quasi-stochastic process.

The present work acknowledges the multitude of scales that influence atmospheric variability, and the complexity of all scale interactions cannot be synthesized within scope of single thesis. Yet in a few focused studies, this thesis has addressed scales of relevance to the ASIRI-RAWI project, namely a portion of the intraseasonal time scales (<45 days and below) and within equatorial Indian Ocean (spatial scales on order 1000 km and below). The impact of the observed phenomena beyond targeted temporal scales would be a beneficial direction for future research. For instance, a third upper-level Kelvin wave crest (see ~12 March in Figure 3.2) appeared in observations and may have contributed to an MJO event later in March 2015, as gleaned from RMM index (Wheeler and Hendon 2004; http://www.bom.gov.au/climate/mjo/) which showed a resurgence in MJO strength following experimental period. This possibility would be similar to what has been recently proposed for other wave-like disturbances in a 2011 MJO event (Powell and Houze 2015) and MJOs in general (Sakaeda and Roundy 2016), which cited dynamic convective initiation like was hypothesized in Chapter 3 for the initiation of the convectively-linked WWBs. Moreover future work could address whether the described phenomena contributed to the strong 2015-2016 El Niño, a phenomena that has been associated with (oceanic) Kelvin waves and WWBs in past studies. These oceanic Kelvin waves could be triggered by the atmospheric Kelvin waves and associated WWBs. Finally, it is important to understand better how common these phenomena are outside of study period to better judge their broader impact. We hope this work has been robust in its descriptions of these phenomena to allow research groups specializing in the mining of long-term satellite and reanalysis datasets to utilize these results. Overall, the knowledge of the evolution of equatorial Kelvin waves and their impacts across a swath of space-time scales, planetary to ABL turbulence, is an important contribution from this thesis for improving predictability of global circulation models.

APPENDIX A:

MISCELLANEOUS TABLES

A.1 Definitions

These tables contain information that will aid in the application of results presented in this thesis. Table A.1 is included so readers may convert easily between pressure levels (hectopascals) and altitude (meters), if preferred, for aid in interpretation of text and figures in Chapter 3. Table A.2 is a resource for all data used to create Figures 5.4-5.6 in Chapter 5. It should be helpful to readers who wish to apply this unique dataset to their own studies or for comparisons.

TABLE A.1

PRESSURE-ALTITUDE EQUIVALENTS AT SEYCHELLES (5°S, 55°E)

Pressure (hPa)	Altitude (m)
1000	100
975	325
950	550
925	800
900	1,025
875	1,275
850	1,525
825	1,775
800	2,050
775	2,300
750	2,575
700	3,175
650	3,775
600	4,425
550	5,125
500	5,875
450	6,700
400	7,600
350	8,600
300	9,725
250	10,975
225	11,675
200	12,450
175	13,300
150	14,250
125	15,325
100	16,600
70	18,600

TABLE A.2

MINUTE-AVERAGED TURBULENCE AND FLOW PARAMETERS

Minute	**$10^3 \cdot \varepsilon$ ($m^2\ s^{-3}$)**	**σ_u ($m\ s^{-1}$)**	**$10^3 \cdot N^2$ (s^{-2})**	**$10^3 \cdot P$ ($m^2\ s^{-3}$)**	**$10^4 \cdot B$ ($m^2\ s^{-3}$)**	**Ri_g**	**Γ**
1[a]	2.96	0.127	24	-0.11	-1.02	1.0	-0.035
2	.451	0.153	6.7	-0.095	-.246	1.9	-0.055
3	.659	0.0954	15	-0.014	-.394	1.2	-0.060
4	22.2	0.117	11	-0.056	-.555	1.3	-0.003
5	4.20	0.155	15	-0.41	.329	0.56	0.008
6	16.4	0.238	12	1.0	6.51	0.45	0.040
7	763	0.576	10.	2.9	3.59	0.21	0.000
8	518	0.538	15	3.7	8.64	0.16	0.002
9	212	0.410	13	3.5	5.79	0.20	0.003
10	165	0.529	9.0	12	12.8	0.11	0.008
11	261	0.542	7.7	2.8	8.27	0.12	0.003
12[b]	48.2	0.449	6.5	7.6	10.8	0.13	0.022
13	23.7	0.539	6.9	11	13.5	0.14	0.057
14	2.83	0.277	8.4	2.0	5.68	0.31	0.201
15	116	0.489	6.7	3.2	10.2	0.26	0.009
16	325	0.506	8.2	8.9	19.4	0.13	0.006
17	422	0.535	5.6	3.6	18.4	0.18	0.004
18	228	0.379	5.9	0.37	3.67	0.16	0.002
19	11.2	0.341	6.7	2.4	4.14	0.20	0.037
20	11.5	0.390	9.0	6.5	11.2	0.17	0.098
21	10.8	0.457	8.1	3.9	5.86	0.20	0.054
22	54.7	0.429	9.7	8.1	13.4	0.18	0.024
23	192	0.387	9.2	3.4	7.90	0.21	0.004
24	135	0.412	6.5	4.6	7.77	0.16	0.006
25	137	0.367	6.7	3.1	6.93	0.13	0.005
26	184	0.449	6.9	2.6	6.92	0.19	0.004
27	54.4	0.655	5.8	7.8	8.20	0.14	0.015
28	58.0	0.301	7.0	3.2	6.07	0.23	0.010
29[c]	3.77	0.341	7.7	5.6	12.1	0.17	0.320
30	5.03	0.554	8.7	11	11.7	0.13	0.233
31*	7.31	0.488	6.8	7.4	9.81	0.12	0.134
32*	7.25	0.478	6.8	9.0	10.2	0.13	0.140

TABLE A.2 (CONTINUED)

Minute	**$10^3 \cdot \varepsilon$ (m² s⁻³)**	**σ_u (m s⁻¹)**	**$10^3 \cdot N^2$ (s⁻²)**	**$10^3 \cdot P$ (m² s⁻³)**	**$10^4 \cdot B$ (m² s⁻³)**	**Ri_g**	**Γ**
33	20.2	0.403	6.8	2.1	7.86	0.12	0.039
34*	7.89	0.496	7.9	5.7	10.1	0.14	0.128
35	4.08	0.447	7.2	9.2	12.0	0.14	0.295
36*	3.96	0.406	8.4	4.9	6.36	0.15	0.161
37*	5.15	0.425	7.3	7.2	7.31	0.13	0.142
38	2.82	0.281	7.2	0.69	4.51	0.28	0.160
39	1.86	0.365	7.7	1.5	9.89	0.39	0.533
40*	2.93	0.345	7.3	3.6	4.30	0.18	0.147
41	4.97	0.554	9.4	21	15.5	0.11	0.312
42	3.22	0.421	8.3	7.6	8.11	0.23	0.252
43	.973	0.186	13	0.18	.927	0.77	0.095
44*	2.90	0.332	9.4	1.9	4.66	0.32	0.161
45*	3.35	0.313	13	1.1	7.75	0.29	0.231
46*	2.97	0.316	12	3.1	6.24	0.25	0.210
47	1.94	0.216	15	0.90	6.78	0.36	0.350
48	4.60	0.585	11	3.1	9.30	0.18	0.202
49	60.3	0.412	6.2	3.5	4.72	0.18	0.008
50[d]	2.00	0.286	8.0	2.1	8.66	0.30	0.434
51	2.56	0.500	7.5	0.13	2.68	0.35	0.105
52	9.11	0.304	8.2	4.2	6.16	0.17	0.068
53*	2.94	0.315	8.1	2.8	4.79	0.30	0.163
54	16.3	0.371	8.9	5.1	6.09	0.28	0.037

REFERENCES

Alappattu, D. P., and P. K. Kunhikrishnan, 2010: First observations of turbulence parameters in the troposphere over the Bay of Bengal and the Arabian Sea using radiosonde. *J. Geophys. Res. Atmos.*, **115**, D06105, doi:10.1029/2009JD012916.

Andrews, D. G., J. R. Holton, and C. B. Leovy, 1987: *Middle Atmosphere Dynamics*. Academic Press, San Diego, 489 pp.

Azad, R., and S. Kassab, 1989: New method of obtaining dissipation. *Exp. Fluids*, **7**, 81–87, doi:10.1007/BF00207299.

Bernie, D. J., S. J. Woolnough, J. M. Slingo, and E. Guilyardi, 2005: Modeling Diurnal and Intraseasonal Variability of the Ocean Mixed Layer. *J. Clim.*, **18**, 1190–1202, doi:10.1175/JCLI3319.1.

Bhat, G. S., and H. J. S. Fernando, 2016: Remotely Driven Anomalous Sea-Air Heat Flux Over the North Indian Ocean During the Summer Monsoon Season. *Oceanography*, **29**, 232–241, doi:10.5670/oceanog.2016.55.

Brown, A., S. Milton, M. Cullen, B. Golding, J. Mitchell, and A. Shelly, 2012: Unified Modeling and Prediction of Weather and Climate: A 25-Year Journey. *Bull. Am. Meteorol. Soc.*, **93**, 1865–1877, doi:10.1175/BAMS-D-12-00018.1.

Centurioni, L. R., and Coauthors, 2017: Northern Arabian Sea Circulation-Autonomous Research (NASCar): A Research Initiative Based on Autonomous Sensors. *Oceanography*, **30**, 78–91, doi:10.5670/oceanog.2017.224.

Chatterjee, P., and B. N. Goswami, 2004: Structure, genesis and scale selection of the tropical quasi-biweekly mode. *Q. J. R. Meteorol. Soc.*, **130**, 1171–1194, doi:10.1256/qj.03.133.

Chen, G., and C. H. Sui, 2010: Characteristics and origin of quasi-biweekly oscillation over the western North Pacific during boreal summer. *J. Geophys. Res. Atmos.*, **115**, D14113, doi:10.1029/2009JD013389.

Chen, S., and Coauthors, 2015: A Study of CINDY/DYNAMO MJO Suppressed Phase. *J. Atmos. Sci.*, **72**, 3755–3779, doi:10.1175/JAS-D-13-0348.1.

Cho, H. K., K. P. Bowman, and G. R. North, 2004: Equatorial waves including the Madden-Julian oscillation in TRMM rainfall and OLR data. *J. Clim.*, **17**, 4387–4406, doi:10.1175/3215.1.

Conry, P., A. Sharma, M. J. Potosnak, L. S. Leo, E. Bensman, J. J. Hellmann, and H. J. S. Fernando, 2015: Chicago's Heat Island and Climate Change: Bridging the Scales via Dynamical Downscaling. *J. Appl. Meteorol. Climatol.*, **54**, 1430–1448, doi:10.1175/JAMC-D-14-0241.1.

Cronin, T. W., K. A. Emanuel, and P. Molnar, 2015: Island precipitation enhancement and the diurnal cycle in radiative-convective equilibrium. *Q. J. R. Meteorol. Soc.*, **141**, 1017–1034, doi:10.1002/qj.2443.

Dee, D. P., and Coauthors, 2011: The ERA-Interim reanalysis: Configuration and performance of the data assimilation system. *Q. J. R. Meteorol. Soc.*, **137**, 553–597, doi:10.1002/qj.828.

Dias, J., and G. N. Kiladis, 2014: Influence of the basic state zonal flow on convectively coupled equatorial waves. *Geophys. Res. Lett.*, **41**, 6904–6913, doi:10.1002/2014GL061476.

Dias, J., and G. N. Kiladis, 2016: The Relationship between Equatorial Mixed Rossby–Gravity and Eastward Inertio-Gravity Waves. Part II. *J. Atmos. Sci.*, **73**, 2147–2163, doi:10.1175/JAS-D-15-0231.1.

Dias, J., N. Sakaeda, G. N. Kiladis, and K. Kikuchi, 2017: Influences of the MJO on the space-time organization of tropical convection. *J. Geophys. Res. Atmos.*, **122**, 8012–8032, doi:10.1002/2017JD026526.

Ellison, T. H., 1957: Turbulent transfer of heat and momentum from an infinite rough plane. *J. Fluid. Mech.*, **2**, 456–466, doi:10.1017/S0022112057000269.

Elsner, J. W., and W. Elsner, 1996: On the measurement of turbulence energy dissipation. *Meas. Sci. Technol.*, **7**, 1334–1348, doi:10.1088/0957-0233/7/10/005.

EUMETSAT, 2016: METEOSAT-7 Temperature to Radiance Conversion Tables. 5. https://www.eumetsat.int/website/home/Data/Products/Calibration/MFGCalibration/index.html (Accessed October 25, 2016).

Eurpoean Centre for Medium Range Weather Forecasts, 2009: ERA-Interim Project. doi:10.5065/D6CR5RD9.

Fairall, C. W., E. F. Bradley, D. P. Rogers, J. B. Edson, and G. S. Young, 1996: Bulk parameterization of air-sea fluxes for Tropical Ocean-Global Atmosphere

Coupled-Ocean Atmosphere Response Experiment. *J. Geophys. Res. Ocean.*, **101**, 3747–3764, doi:10.1029/95JC03205.

Fairall, C. W., and Coauthors, 2010: Observations to Quantify Air-Sea Fluxes and Their Role in Climate Variability and Predictability. *Proceedings of OceanObs'09: Sustained Ocean Observations and Information for Society, Vol. 2.*, Venice, Italy, FSA Publication, 299–313.

Fernando, H. J. S., 1991: Turbulent Mixing in Stratified Fluids. *Annu. Rev. Fluid Mech.*, **23**, 455–493, doi:10.1146/annurev.fl.23.010191.002323.

Fernando, H. J. S., 2003: Turbulent patches in a stratified shear flow. *Phys. Fluids*, **15**, 3164–3169, doi:10.1063/1.1949203.

Fernando, H. J. S., and E. R. Pardyjak, 2013: Field Studies Delve Into the Intracacies of Mountain Weather. *Eos*, **94**, 313–315, doi:10.1002/2013EO360001.

Fernando, H. J. S., and Coauthors, 2015: The MATERHORN: Unraveling the Intricacies of Mountain Weather. *Bull. Am. Meteorol. Soc.*, **96**, 1945–1968, doi:10.1175/BAMS-D-13-00131.1.

Flannaghan, T. J., and S. Fueglistaler, 2011: Kelvin waves and shear-flow turbulent mixing in the TTL in (re-)analysis data. *Geophys. Res. Lett.*, **38**, L02801, doi:10.1029/2010GL045524.

Fueglistaler, S., A. E. Dessler, T. J. Dunkerton, I. Folkins, Q. Fu, and P. W. Ote, 2009: Tropical tropopause layer. *Rev. Geophys.*, **47**, 2008RG000267, doi:10.1029/2008RG000267.

Fujiwara, M., and M. Takahashi, 2001: Role of the equatorial Kelvin wave in stratosphere-troposphere exchange in a general circulation model. *J. Geophys. Res.*, **106**, 22763–22780, doi:10.1029/2000JD000161.

Fujiwara, M., K. Kita, and T. Ogawa, 1998: Stratosphere-troposphere exchange of ozone associated with the equatorial Kelvin wave as observed with ozonesondes and rawinsondes. *J. Geophys. Res.*, **103**, 19173–19182, doi:10.1029/98JD01419.

Fujiwara, M., F. Hasebe, M. Shiotani, N. Nishi, H. Vömel, and S. J. Oltmans, 2001: Water vapor control at the tropopause by equatorial Kelvin waves observed over the Galápagos. *Geophys. Res. Lett.*, **28**, 3143–3146, doi:10.1029/2001GL013310.

Fujiwara, M., M. K. Yamamoto, H. Hashiguchi, T. Horinouchi, and S. Fukao, 2003: Turbulence at the tropopause due to breaking Kelvin waves observed by the Equatorial Atmosphere Radar. *Geophys. Res. Lett.*, **30**, doi:10.1029/2002GL016278.

Gargett, A. E., T. R. Osborn, and P. W. Nasmyth, 1984: Local isotropy and the decay of turbulence in a stratified fluid. *J. Fluid Mech.*, **144**, 231–280, doi:10.1017/S0022112084001592.

Gibson, C. H., 1980: Fossil Temperature, Salinity and Vorticity Turbulence in the Ocean. *Mar. Turbul. Elsevier Oceanogr. Ser.*, **28**, 221–257, doi:10.1016/S0422-9894(08)71223-6.

Gibson, C. H., G. R. Stegen, and R. B. Williams, 1970: Statistics of the fine structure of turbulent velocity and temperature fields measured at high Reynolds number. *J. Fluid Mech.*, **41**, 153–167, doi:10.1017/S0022112070000551.

Gottschalck, J., P. E. Roundy, C. J. Schreck III, A. Vintzileos, and C. Zhang, 2013: Large-Scale Atmospheric and Oceanic Conditions during the 2011–12 DYNAMO Field Campaign. *Mon. Weather Rev.*, **141**, 4173–4196, doi:10.1175/MWR-D-13-00022.1.

Grachev, A. A., E. L. Andreas, C. W. Fairall, P. S. Guest, and P. O. G. Persson, 2015: Similarity theory based on the Dougherty-Ozmidov length scale. *Q. J. R. Meteorol. Soc.*, **141**, 1845–1856, doi:10.1002/qj.2488.

Grise, K. M., and D. W. J. Thompson, 2012: Equatorial Planetary Waves and Their Signature in Atmospheric Variability. *J. Atmos. Sci.*, **69**, 857–874, doi:10.1175/JAS-D-11-0123.1.

Gulitski, G., M. Kholmyansky, W. Kinzelbach, B. Luthy, A. Tsinober, and S. Yorish, 2007: Velocity and temperature derivatives in high-Reynolds-number turbulent flows in the atmospheric surface layer. Part 1. Facilities, methods and some general results. *J. Fluid Mech.*, **589**, 57–81, doi:10.1017/S0022112007007495.

Haertel, P. T., and R. H. Johnson, 1998: Two-day disturbances in the equatorial western Pacific. *Q. J. R. Meteorol. Soc.*, **124**, 615–636, doi:10.1256/smsqj.54610.

Ham, S., S. Y. Hong, and S. Park, 2014: A study on air-sea interaction on the simulated seasonal climate in an ocean-atmosphere coupled model. *Clim. Dyn.*, **42**, 1175–1187, doi:10.1007/s00382-013-1847-0.

Hamilton, K., 1999: Dynamical coupling of the lower and middle atmosphere: Historical background to current research. *J. Atmos. Solar-Terrestrial Phys.*, **61**, 73–84, doi:10.1016/S1364-6826(98)00118-7.

Hayashi, Y., 1977: Space-Time Power Maximum Spectral Entropy Analysis Method Using the Maximum Entropy Method. *J. Meteorol. Soc. Japan*, **55**, 415–420, doi:10.2151/jmsj1965.55.4_415.

Holton, J. R., 1992: *An Introduction to Dynamic Meteorology*. 3rd ed. Academic Press, San Diego, 511 pp.

Holton, J. R., and R. S. Lindzen, 1968: A Note on "Kelvin" Waves in the Atmosphere. *Mon. Weather Rev.*, **96**, 385–386, doi:10.1175/1520-0493(1968)096<0385:ANOKWI>2.0.CO;2.

Holton, J. R., and R. S. Lindzen, 1972: An Updated Theory for the Quasi-Biennial Cycle of the Tropical Stratosphere. *J. Atmos. Sci.*, **29**, 1076–1080, doi:10.1175/1520-0469(1972)029<1076:AUTFTQ>2.0.CO;2.

Holton, J. R., P. H. Haynes, M. E. McIntyre, A. R. Douglass, R. B. Rood, and L. Pfister, 1995: Stratosphere-troposphere exchange. *Rev. Geophys.*, **33**, 403–439, doi:10.1029/95RG02097.

Holton, J. R., M. J. Alexander, and M. T. Boehm, 2001: Evidence for short vertical wavelength Kelvin waves in the Department of Energy-Atmospheric Radiation Measurement Nauru99 radiosonde data. *J. Geophys. Res.*, **106**, 20,125-20,129, doi:10.1029/2001JD900108.

Hopfinger, E. J., and P. F. Linden, 1982: Formation of thermoclines in zero-mean-shear turbulence subjected to a stabilizing buoyancy force. *J. Fluid Mech.*, **114**, 157–173, doi:10.1017/S0022112082000081.

Hurrell, J. W., G. A. Meehl, D. C. Bader, T. L. Delworth, B. Kirtman, and B. Wielicki, 2009: A Unified Modeling Approach to Climate System Prediction. *Bull. Am. Meteorol. Soc.*, **90**, 1819–1832, doi:10.1175/2009BAMS2752.1.

Immler, F., K. Krüger, M. Fujiwara, G. Verver, M. Rex, and O. Schrems, 2008: Correlation between equatorial Kelvin waves and the occurrence of extremely thin ice clouds at the tropical tropopause. *Atmos. Chem. Phys.*, **8**, 4019–4026, doi:10.5194/acp-8-4019-2008.

Ishihara, T., K. Morishita, M. Yokokawa, A. Uno, and Y. Kaneda, 2016: Energy spectrum in high-resolution direct numerical simulations of turbulence. *Phys. Rev. Fluids*, **1**, 82403, doi:10.1103/PhysRevFluids.1.082403.

Ivey, G. N., and J. Imberger, 1991: On the Nature of Turbulence in a Stratified Fluid. Part I: The Energetics of Mixing. *J. Phys. Oceanogr.*, **21**, 650–658, doi:10.1175/1520-0485(1991)021<0650:OTNOTI>2.0.CO;2.

Ivey, G. N., K. B. Winters, and J. R. Koseff, 2008: Density stratification, turbulence, but how much mixing? *Annu. Rev. Fluid Mech.*, **40**, 169–184, doi:10.1146/annurev.fluid.39.050905.110314.

Kaimal, J. C., and J. J. Finnigan, 1994: *Atmospheric Boundary Layer Flows: Their Structure and Measurement*. 1st ed. Oxford Univ Press, New York, 289 pp.

Kalnay, E., and Coauthors, 1996: The NCEP/NCAR 40-Year Reanalysis Project. *Bull. Am. Meteorol. Soc.*, **77**, 437–471, doi:10.1175/1520-0477(1996)077<0437:TNYRP>2.0.CO;2.

Kikuchi, K., G. N. Kiladis, J. Dias, and T. Nasuno, 2017: Convectively coupled equatorial waves within the MJO during CINDY/DYNAMO: slow Kelvin waves as building blocks. *Clim. Dyn.*, **49**, doi:10.1007/s00382-017-3869-5.

Kiladis, G. N., and M. Wheeler, 1995: Horizontal and vertical structure of observed tropospheric equatorial Rossby waves. *J. Geophys. Res.*, **100**, 22981–22997, doi:10.1029/95JD02415.

Kiladis, G. N., M. C. Wheeler, P. T. Haertel, K. H. Straub, and P. E. Roundy, 2009: Convectively coupled equatorial waves. *Rev. Geophys.*, **47**, 2008RG000266, doi:10.1029/2008RG000266.

Kiladis, G. N., J. Dias, and M. Gehne, 2016: The Relationship between Equatorial Mixed Rossby–Gravity and Eastward Inertio-Gravity Waves. Part 1. *J. Atmos. Sci.*, **73**, 2123–2145, doi:10.1175/JAS-D-15-0230.1.

Kim, J.-E., and M. J. Alexander, 2013: Tropical precipitation variability and convectively coupled equatorial waves on submonthly time scales in reanalyses and TRMM. *J. Clim.*, **26**, 3013–3030, doi:10.1175/JCLI-D-12-00353.1.

Kit, E., E. J. Strang, and H. J. S. Fernando, 1997: Measurement of turbulence near shear-free density interfaces. *J. Fluid Mech.*, **334**, 293–314, doi:10.1017/S0022112096004442.

Kit, E., A. Cherkassky, T. Sant, and H. J. S. Fernando, 2010: In Situ Calibration of Hot-Film Probes Using a Collocated Sonic Anemometer: Implementation of a Neural Network. *J. Atmos. Ocean. Technol.*, **27**, 23–41, doi:10.1175/2009JTECHA1320.1.

Kit, E., C. M. Hocut, D. Liberzon, and H. J. S. Fernando, 2017: Fine-Scale turbulent bursts in stable atmospheric boundary layer in complex terrain. *J. Fluid Mech.*, **833**, 745–772, doi:10.1017/jfm.2017.717.

Kravtsov, S., M. G. Wyatt, J. A. Curry, and A. A. Tsonis, 2014: Two contrasting views of multidecadal climate variability in the twentieth century. *Geophys. Res. Lett.*, **41**, 6881–6888, doi:10.1175/JCLI-D-12-00353.1.

Kubota, H., K. Yoneyama, J.-I. Hamada, P. Wu, A. Sudaryanto, and I. B. Wahyono, 2015: Role of Maritime Continent Convection during the Preconditioning Stage of the

Madden-Julian Oscillation Observed in CINDY2011/DYNAMO. *J. Meteorol. Soc. Japan*, **93A**, 101–114, doi:10.2151/jmsj.2015-050.

Large, W. G., and S. Pond, 1981: Open Ocean Momentum Flux Measurements in Moderate to Strong Winds. *J. Phys. Oceanogr.*, **11**, 324–336, doi:10.1175/1520-0485(1981)011<0324:OOMFMI>2.0.CO;2.

Large, W. G., J. C. McWilliams, and S. C. Doney, 1994: Oceanic Vertical Mixing: A Review and a Model with a Nonlocal Boundary-Layer Parameterization. *Rev. Geophys.*, **32**, 363–403, doi:10.1029/94rg01872.

Leccese, M. R., 2004: Vaisala Radiosonde RS92: On Trial in Italy. *Vaisala News*.

Linden, P. F., 1980: Mixing across a density interface produced by grid turbulence. *J. Fluid Mech.*, **100**, 691–703, doi:10.1017/S002211208000136X.

Liu, C., and E. J. Zipser, 2005: Global distribution of convection penetrating the tropical tropopause. *J. Geophys. Res. Atmos.*, **110**, D23104, doi:10.1029/2005JD006063.

Long, R. L., 1982: A new theory of the energy spectrum. *Bound.-Layer Meteorol.*, **24**, 137–160.

Lozovatsky, I. D., and H. J. S. Fernando, 2012: Mixing efficiency in natural flows. *Philos. Trans. R. Soc.*, **371**, doi:10.1098/rsta.2012.0213.

Madden, R. A., and P. R. Julian, 1972: Description of Global-Scale Circulation Cells in the Tropics with a 40–50 Day Period. *J. Atmos. Sci.*, **29**, 1109–1123, doi:10.1175/1520-0469(1972)029<1109:DOGSCC>2.0.CO;2.

Maderich, V. S., G. J. F. Van Heijst, and A. Brandt, 2001: Laboratory experiments on intrusive flows and internal waves in a pycnocline. *J. Fluid Mech.*, **432**, 285–311.

Maffioli, A., G. Brethouwer, and E. Lindborg, 2016: Mixing efficiency in stratified turbulence. *J. Fluid Mech.*, **794**, doi:10.1017/jfm.2016.206.

Maruyama, T., 1994: Upward Transport of Westerly Momentum due to Disturbances of the Equatorial Lower Stratosphere in the Period Range of about 2 Days — A Singapore Data Analysis for 1983-1993. *J. Meteorol. Soc. Japan*, **72**, 423–432.

Mater, B. D., and S. K. Venayagamoorthy, 2014: The quest for an unambiguous parameterization of mixing efficiency in stably stratified geophysical flows. *Geophys. Res. Lett.*, **41**, 4646–4653, doi:10.1002/2014GL060571.

Matsuno, T., 1966: Quasi-Geostrophic Motions in the Equatorial Area. *J. Meteorol. Soc. Japan*, **44**, 25–43.

McPhaden, M. J., and Coauthors, 2009: RAMA: The research moored array for African-Asian-Australian monsoon analysis and prediction. *Bull. Am. Meteorol. Soc.*, **90**, 459–480, doi:10.1175/2008BAMS2608.1.

Mega, T., M. K. Yamamoto, H. Luce, Y. Tabata, H. Hashiguchi, M. Yamamoto, M. D. Yamanaka, and S. Fukao, 2010: Turbulence generation by Kelvin-Helmholtz instability in the tropical tropopause layer observed with a 47 MHz range imaging radar. *J. Geophys. Res. Atmos.*, **115**, D18115, doi:10.1029/2010JD013864.

Mellor, G. L., and T. Yamada, 1974: A Hierarchy of Turbulence Closure Models for Planetary Boundary Layers. *J. Atmos. Sci.*, **31**, 1791–1806, doi:10.1175/1520-0469(1974)031<1791:AHOTCM>2.0.CO;2.

Mellor, G. L., and T. Yamada, 1982: Development of a Turbulence Closure Model for Geophysical Fluid Problems. *Rev. Geophys. Sp. Phys.*, **20**, 851–875, doi:10.1029/RG020i004p00851.

Molinari, J., K. Lombardo, and D. Vollaro, 2007: Tropical Cyclogenesis within an Equatorial Rossby Wave Packet. *J. Atmos. Sci.*, **64**, 1301–1317, doi:10.1175/JAS3902.1.

Monti, P., H. J. S. Fernando, M. Princevac, W. C. Chan, T. A. Kowalewski, and E. R. Pardyjak, 2002: Observations of Flow and Turbulence in the Nocturnal Boundary Layer over a Slope. *J. Atmos. Sci.*, **59**, 2513–2534, doi:10.1175/1520-0469(2002)059<2513:OOFATI>2.0.CO;2.

Moum, J. N., D. R. Caldwell, and C. A. Paulson, 1989: Mixing in the equatorial surface layer and thermocline. *J. Geophys. Res. Ocean.*, **94**, 2005–2022, doi:10.1029/JC094iC02p02005.

Moum, J. N., and Coauthors, 2014: Air-sea interactions from westerly wind bursts during the November 2011 MJO in the Indian Ocean. *Bull. Am. Meteorol. Soc.*, **95**, 1185–1199, doi:10.1175/BAMS-D-12-00225.1.

Moum, J. N., K. Pujiana, R. C. Lien, and W. D. Smyth, 2016: Ocean feedback to pulses of the Madden-Julian Oscillation in the equatorial Indian Ocean. *Nat. Commun.*, **7**, 13203, doi:10.1038/ncomms13203.

Nakazawa, T., 1988: Tropical Super Clusters within Intraseasonal Variations over the Western Pacific. *J. Meteorol. Soc. Japan*, **66**, 823–839.

Noh, Y., and H. J. Kim, 1999: Simulations of temperature and turbulence structure of the oceanic boundary layer with the improved near-surface process. *J. Geophys. Res.*, **104**, 15621–15634, doi:10.1029/1999JC900068.

Noh, Y., G. Goh, and S. Raasch, 2011: Influence of Langmuir Circulation on the Deepening of the Wind-Mixed Layer. *J. Phys. Oceanogr.*, **41**, 472–484, doi:10.1175/2010JPO4494.1.

Noh, Y., H. Ok, E. Lee, T. Toyoda, and N. Hirose, 2016: Parameterization of Langmuir circulation in the ocean mixed layer model using LES and its application to the OGCM. *J. Phys. Oceanogr.*, **46**, 57–78, doi:10.1175/JPO-D-14-0137.1.

Oke, T. R., 1978: Energy and mass exchanges. *Boundary Layer Climates*, Methuen & Co. Ltd., New York, 3–30.

Osborn, T. R., 1980: Estimates of the Local Rate of Vertical Diffusion from Dissipation Measurements. *J. Phys. Oceanogr.*, **10**, 83–89, doi:10.1175/1520-0485(1980)010<0083:EOTLRO>2.0.CO;2.

Pacanowski, R. C., and S. G. H. Philander, 1981: Parameterization of Vertical Mixing in Numerical Models of Tropical Oceans. *J. Phys. Oceanogr.*, **11**, 1443–1451, doi:10.1175/1520-0485(1981)011<1443:POVMIN>2.0.CO;2.

Pardyjak, E. R., P. Monti, and H. J. S. Fernando, 2002: Flux Richardson number measurements in stable atmospheric shear flows. *J. Fluid Mech.*, **459**, 307–316, doi:10.1017/S0022112002008406.

Parker, W. S., 2016: Reanalyses and observations: What's the Difference? *Bull. Am. Meteorol. Soc.*, **97**, 1565–1572, doi:10.1175/BAMS-D-14-00226.1.

Paulson, C. A., and J. J. Simpson, 1977: Irradiance Measurements in the Upper Ocean. *J. Phys. Oceanogr.*, **7**, 952–956, doi:10.1175/1520-0485(1977)007<0952:IMITUO>2.0.CO;2.

Peatman, S. C., A. J. Matthews, and D. P. Stevens, 2014: Propagation of the Madden--Julian Oscillation through the Maritime Continent and scale interaction with the diurnal cycle of precipitation. *Q. J. R. Meteorol. Soc.*, **140**, 814–825, doi:10.1002/qj.2161.

Pires, P., J.-L. Redelsperger, and J.-P. Lafore, 1997: Equatorial Atmospheric Waves and Their Association to Convection. *Mon. Weather Rev.*, **125**, 1167–1184, doi:10.1175/1520-0493(1997)125<1167:EAWATA>2.0.CO;2.

Powell, S. W., and R. A. Houze, 2015: Effect of dry large-scale vertical motions on initial MJO convective onset. *J. Geophys. Res. Atmos.*, **120**, 4783–4805, doi:10.1002/2014JD022961.

Price, J. F., R. A. Weller, and R. Pinkel, 1986: Diurnal Cycling: Observations and Models of the Upper Ocean Response to Diurnal Heating, Cooling, and Wind Mixing. *J. Geophys. Res.*, **91**, 8411–8427, doi:10.1029/JC091iC07p08411.

Randel, W. J., and F. Wu, 2005: Kelvin wave variability near the equatorial tropopause observed in GPS radio occultation measurements. *J. Geophys. Res. D Atmos.*, **110**, D03102, doi:10.1029/2004JD005006.

Randel, W. J., and E. J. Jensen, 2013: Physical processes in the tropical tropopause layer and their roles in a changing climate. *Nat. Geosci.*, **6**, 169–176, doi:10.1038/ngeo1733.

Ratnam, M. V., T. Tsuda, S. Mori, and T. Kozu, 2006: Modulation of Tropopause Temperature Structure Revealed by Simultaneous Radiosonde and CHAMP GPS Measurements. *J. Meteorol. Soc. Japan*, **84**, 989–1003, doi:10.2151/jmsj.84.989.

Reed, R. J., and E. E. Recker, 1971: Structure and Properties of Synoptic-Scale Wave Disturbances in the Equatorial Western Pacific. *J. Atmos. Sci.*, **28**, 1117–1133, doi:10.1175/1520-0469(1971)028<1117:SAPOSS>2.0.CO;2.

Rienecker, M. M., and Coauthors, 2011: MERRA: NASA's modern-era retrospective analysis for research and applications. *J. Clim.*, **24**, 3624–3648, doi:10.1175/JCLI-D-11-00015.1.

Riley, J. J., and E. Lindborg, 2008: Stratified Turbulence: A Possible Interpretation of Some Geophysical Turbulence Measurements. *J. Atmos. Sci.*, **65**, 2416–2424, doi:10.1175/2007JAS2455.1.

Sakaeda, N., and P. E. Roundy, 2015: The Development of Upper-Tropospheric Wind over the Western Hemisphere in Association with MJO Convective Initiation. *J. Atmos. Sci.*, **72**, 3138–3160, doi:10.1175/JAS-D-14-0293.1.

Sakaeda, N., and P. E. Roundy, 2016: The development of upper-tropospheric geopotential height anomaly in the Western Hemisphere during MJO convective initiations. *Q. J. R. Meteorol. Soc.*, **142**, 942–956, doi:10.1002/qj.2696.

Sato, K., and T. J. Dunkerton, 1997: Estimates of momentum flux associated with equatorial Kelvin and gravity waves. *J. Geophys. Res. Atmos.*, **102**, 26247–26261, doi:10.1029/96JD02514.

Sato, K., F. Hasegawa, and I. Hirota, 1994: Short-Period Disturbances in the Equatorial Lower Stratosphere. *J. Meteorol. Soc. Japan*, **72**, 859–872, doi:10.2151/jmsj1965.72.6_859.

Schreck, C. J., and J. Molinari, 2009: A Case Study of an Outbreak of Twin Tropical Cyclones. *Mon. Weather Rev.*, **137**, 863–875, doi:10.1175/2008MWR2541.1.

Seo, K. H., and Y. Xue, 2005: MJO-related oceanic Kelvin waves and the ENSO cycle: A study with the NCEP Global Ocean Data Assimilation System. *Geophys. Res. Lett.*, **32**, L07712, doi:10.1029/2005GL022511.

Sheih, C. M., H. Tennekes, and J. L. Lumley, 1971: Airborne Hot-Wire Measurements of the Small-Scale Structure of Atmospheric Turbulence. *Phys. Fluids*, **14**, 201–215, doi:10.1063/1.1693416.

Sherwood, S. C., 2000: A Stratospheric "Drain" over the Maritime Continent. *Geophys. Res. Lett.*, **27**, 677–680, doi:10.1029/1999GL010868.

Shimizu, A., and T. Tsuda, 1997: Characteristics of Kelvin waves and gravity waves observed with radiosondes over Indonesia. **102**, 26159–26171, doi:10.1029/96JD03146.

Shinoda, T., and H. H. Hendon, 1998: Mixed Layer Modeling of Intraseasonal Variability in the Tropical Western Pacific and Indian Oceans. *J. Clim.*, **11**, 2668–2685, doi:10.1175/1520-0442(1998)011<2668:MLMOIV>2.0.CO;2.

De Silva, I. P. D., and H. J. S. Fernando, 1998: Experiments on collapsing turbulent regions in stratified fluids. *J. Fluid Mech.*, **358**, 29–60, doi:10.1017/S0022112097008094.

De Silva, I. P. D., H. J. S. Fernando, F. Eaton, and D. Hebert, 1996: Evolution of Kelvin-Helmholtz billows in nature and laboratory. *Earth Planet. Sci. Lett.*, **143**, 217–231, doi:10.1016/0012-821X(96)00129-X.

De Silva, I. P. D., A. Brandt, L. J. Montenegro, and H. J. S. Fernando, 1999: Gradient Richardson number measurements in a stratified shear layer. *Dyn. Atmos. Ocean.*, **30**, 47–63, doi:10.1016/S0377-0265(99)00015-9.

Skelly, B. T., D. R. Miller, and T. H. Meyer, 2002: Triple-Hot-Film Amemometer Performance in CASES-99 and a Comparison with Sonic Anemometer Measurements. *Bound.-Layer Meteorol.*, **105**, 275–304, doi:10.1023/A:1019906521898.

Skyllingstad, E. D., and S. P. de Szoeke, 2015: Cloud-Resolving Large-Eddy Simulation of Tropical Convective Development and Surface Fluxes. *Mon. Weather Rev.*, **143**, 2441–2458, doi:10.1175/MWR-D-14-00247.1.

Smagorinksky, J., 1982: Large-scale climate modelling and small-scale physical processes. *Land Surface Processes in Atmospheric General Circulation Models*, P.S. Eagleson, Ed., Cambridge Univ Press, Cambridge, 3–18.

Strang, E. J., and H. J. S. Fernando, 2001a: Vertical Mixing and Transports through a Stratified Shear Layer. *J. Phys. Oceanogr.*, **31**, 2026–2048, doi:10.1175/1520-0485(2001)031<2026:VMATTA>2.0.CO;2.

Strang, E. J., and H. J. S. Fernando, 2001b: Entrainment and mixing in stratified shear flows. *J. Fluid Mech.*, **428**, 349–386, doi:10.1017/S0022112000002706.

Straub, K. H., G. N. Kiladis, and P. E. Ciesielski, 2006: The role of equatorial waves in the onset of the South China Sea summer monsoon and the demise of El Niño during 1998. *Dyn. Atmos. Ocean.*, **42**, 216–238, doi:10.1016/j.dynatmoce.2006.02.005.

Sumi, Y., and H. Masunaga, 2016: A Moist Static Energy Budget Analysis of Quasi-2-Day Waves Using Satellite and Reanalysis Data. *J. Atmos. Sci.*, **73**, 743–759, doi:10.1175/JAS-D-15-0098.1.

Suzuki, J., and M. Shiotani, 2008: Space-time variability of equatorial Kelvin waves and intraseasonal oscillations around the tropical tropopause. *J. Geophys. Res. Atmos.*, **113**, D16110, doi:10.1029/2007JD009456.

Takayabu, Y. N., 1994a: Large-Scale Cloud Disturbances Associated with Equatorial Waves. Part I: Spectral Features of the Cloud Disturbances. *J. Meteorol. Soc. Japan*, **72**, 433–449, doi:10.2151/jmsj1965.72.3_433.

Takayabu, Y. N., 1994b: Large-Scale Cloud Disturbances Associated with Equatorial Waves. Part II: Westward-Propagating Inertio-Gravity Waves. *J. Meteor. Soc. Japan*, **72**, 451–465, doi:10.2151/jmsj1965.72.3_451.

Takayabu, Y. N., K.-M. Lau, and C.-H. Sui, 1996: Observation of a Quasi-2-Day Wave during TOGA COARE. *Mon. Weather Rev.*, **124**, 1892–1913, doi:10.1175/1520-0493(1996)124<1892:OOAQDW>2.0.CO;2.

Tang, Y., H. W. Lean, and J. Bornemann, 2013: The benefits of the Met Office variable resolution NWP model for forecasting convection. *Meteorol. Appl.*, **20**, 417–426, doi:10.1002/met.1300.

Taylor, G. I., 1915: Eddy motions in the atmosphere. *Philos. Trans. R. Soc. London*, **215**, 1–26.

Taylor, G. I., 1970: Some early ideas about turbulence. *J. Fluid. Mech.*, **41**, 3–11.

Thomson, W., 1880: On Gravitational Oscillation of Rotating Water. *Proc. R. Soc. Edinburgh*, **10**, 92–100, doi:10.1017/S0370164600043467.

Tsuda, T., Y. Murayama, H. Wiryosumarto, S. W. B. Harijono, and S. Kato, 1994a: Radiosonde observations of equatorial atmosphere dynamics over Indonesia: 2. Characteristics of gravity waves. *J. Geophys. Res. Atmos.*, **99**, 10507–10516, doi:10.1029/94JD00354.

Tsuda, T., Y. Murayama, H. Wiryosumarto, S. W. B. Harijono, and S. Kato, 1994b: Radiosonde observations of equatorial atmosphere dynamics over Indonesia: 1. Equatorial waves and diurnal tides. *J. Geophys. Res. Atmos.*, **99**, 10491–10505, doi:10.1029/94JD00355.

Tulich, S. N., and B. E. Mapes, 2008: Multiscale Convective Wave Disturbances in the Tropics: Insights from a Two-Dimensional Cloud-Resolving Model. *J. Atmos. Sci.*, **65**, 140–155, doi:10.1175/2007JAS2353.1.

Turner, J. S., 1979: Buoyancy Effects in Fluids. Cambridge Univ Press, Cambridge, 116–123.

Turner, J. S., and E. B. Kraus, 1967: A one-dimensional model of the seasonal thermocline I. A laboratory experiment and its interpretation. *Tellus*, **19**, 88–97, doi:10.1111/j.2153-3490.1967.tb01461.x.

Wallace, J. M., and V. E. Kousky, 1968: Observational Evidence of Kelvin Waves in the Tropical Stratosphere. *J. Atmos. Sci.*, **25**, 900–907, doi:10.1175/1520-0469(1968)025<0900:OEOKWI>2.0.CO;2.

Webster, P. J., and R. Lukas, 1992: TOGA COARE: The Coupled-Atmosphere Response Experiment. *Bull. Am. Meteorol. Soc.*, **73**, 1377–1416, doi:10.1175/1520-0477(1992)073⟨1377:tctcor⟩2.0.CO;2.

Weller, R. A., and S. P. Anderson, 1996: Surface Meteorology and Air-Sea Fluxes in the Western Equatorial Pacific Warm Pool during the TOGA Coupled Ocean-Atmosphere Response Experiment. *J. Clim.*, **9**, 1959–1990, doi:10.1175/1520-0442(1996)009<1959:SMAASF>2.0.CO;2.

Werne, J., and D. C. Fritts, 1999: Stratified shear turbulence: Evolution and statistics. *Geophys. Res. Lett.*, **26**, 439–442, doi:10.1029/1999GL900022.

Wheeler, M., and G. N. Kiladis, 1999: Convectively Coupled Equatorial Waves: Analysis of Clouds and Temperature in the Wavenumber–Frequency Domain. *J. Atmos. Sci.*, **56**, 374–399, doi:10.1175/1520-0469(1999)056<0374:CCEWAO>2.0.CO;2.

Wheeler, M., G. N. Kiladis, and P. J. Webster, 2000: Large-Scale Dynamic Fields Associated with Convectively Coupled Waves. *J. Atmos. Sci.*, **57**, 613–640, doi:10.1175/1520-0469(2000)0572.0.CO;2.

Wheeler, M. C., and H. H. Hendon, 2004: An All-Season Real-Time Multivariate MJO Index: Development of an Index for Monitoring and Prediction. *Mon. Weather Rev.*, **132**, 1917–1932, doi:10.1175/1520-0493(2004)132<1917:AARMMI>2.0.CO;2.

Wijesekera, H. W., and Coauthors, 2016: ASIRI: An Ocean-Atmosphere Initiative for Bay of Bengal. *Bull. Am. Meteorol. Soc.*, **97**, 1859–1884, doi:10.1175/BAMS-D-14-00197.1.

Williams, R. M., and C. A. Paulson, 1977: Microscale temperature and velocity spectra in the atmospheric boundary layer. *J. Fluid Mech.*, **83**, 547–567, doi:10.1017/S0022112077001335.

Wyngaard, J. C., and O. R. Coté, 1971: The Budgets of Turbulent Kinetic Energy and Temperature Variance in the Atmospheric Surface Layer. *J. Atmos. Sci.*, **28**, 190–201, doi:10.1175/1520-0469(1971)028<0190:TBOTKE>2.0.CO;2.

Yamamoto, M. K., M. Fujiwara, T. Horinouchi, H. Hashiguchi, and S. Fukao, 2003: Kelvin-Helmholtz instability around the tropical tropopause observed with the Equatorial Atmosphere Radar. *Geophys. Res. Lett.*, **30**, 1476, doi:10.1029/2002GL016685.

Yanai, M., and T. Maruyama, 1966: Stratospheric Wave Disturbances Propagating over the Equatorial Pacific. *J. Met. Soc. Japan*, **44**, 291–294, doi:10.2151/jmsj1965.44.5_291.

Yang, G.-Y., B. Hoskins, and J. Slingo, 2003: Convectively Coupled Equatorial Waves: A New Methodology for Identifying Wave Structures in Observational Data. *J. Atmos. Sci.*, **60**, 1637–1654, doi:10.1175/1520-0469(2003)060<1637:CCEWAN>2.0.CO;2.

Yang, G.-Y., B. Hoskins, and J. Slingo, 2007: Convectively Coupled Equatorial Waves. Part I: Horizontal and Vertical Structures. *J. Atmos. Sci.*, **64**, 3406–3423, doi:10.1175/JAS4017.1.

Yang, G.-Y., B. Hoskins, and L. Gray, 2012: The Influence of the QBO on the Propagation of Equatorial Waves into the Stratosphere. *J. Atmos. Sci.*, **69**, 2959–2982, doi:10.1175/JAS-D-11-0342.1.

Yoneyama, K., C. Zhang, and C. N. Long, 2013: Tracking Pulses of the Madden-Julian Oscillation. *Bull. Am. Meteorol. Soc.*, **94**, 1871–1891, doi:10.1175/BAMS-D-12-00157.1.

Žagar, N., J. Tribbia, J. L. Anderson, and K. Raeder, 2009: Uncertainties of Estimates of Inertia–Gravity Energy in the Atmosphere. Part II: Large-Scale Equatorial Waves. *Mon. Weather Rev.*, **137**, 3858–3873, doi:10.1175/2009MWR2816.1.

Zangvil, A., and M. Yanai, 1981: Upper Tropospheric Waves in the Tropics. Part II: Association with Clouds in the Wavenumber-Frequency Domain. *J. Atmos. Sci.*, **38**, 939–953, doi:10.1175/1520-0469(1981)038<0939:UTWITT>2.0.CO;2.

Zhang, C., 2013: Madden-Julian Oscillation: Bridging Weather and Climate. *Bull. Am. Meteorol. Soc.*, **94**, 1849–1870, doi:10.1175/BAMS-D-12-00026.1.

Zhou, X., and B. Wang, 2007: Transition from an eastern Pacific upper-level mixed Rossby-gravity wave to a western Pacific tropical cyclone. *Geophys. Res. Lett.*, **34**, L24801, doi:10.1029/2007GL031831.

Zuluaga, M. D., and R. A. Houze, 2013: Evolution of the Population of Precipitating Convective Systems over the Equatorial Indian Ocean in Active Phases of the Madden–Julian Oscillation. *J. Atmos. Sci.*, **70**, 2713–2725, doi:10.1175/JAS-D-12-0311.1.